

# Quasi-continuum reduction of field theories and energetics of defects in Aluminum

by

Mrinal Iyer

A dissertation submitted in partial fulfillment  
of the requirements for the degree of  
Doctor of Philosophy  
(Mechanical Engineering and Scientific Computing)  
in The University of Michigan  
2014

Doctoral Committee:

Associate Professor Vikram Gavini, Chair  
Professor John. E. Allison  
Professor Krishnakumar. R. Garikipati  
Jaroslaw Knap, U.S. Army Research Laboratory

© Mrinal Iyer 2014  

---

All Rights Reserved

For Amma and Appa

# TABLE OF CONTENTS

DEDICATION . . . . .	ii
LIST OF FIGURES . . . . .	v
LIST OF TABLES . . . . .	viii
LIST OF ABBREVIATIONS . . . . .	ix
ABSTRACT . . . . .	x
CHAPTER	
<b>I. Introduction . . . . .</b>	<b>1</b>
<b>II. Quasi Continuum method . . . . .</b>	<b>6</b>
2.1 Overview . . . . .	10
2.2 Error Analysis . . . . .	18
2.2.1 Node-based cluster rules for lattice sums . . . . .	20
2.2.2 Node-based cluster rules on energy . . . . .	26
2.2.3 Element-based cluster rules . . . . .	28
2.3 Local reformulation of interatomic potentials . . . . .	31
2.3.1 Exponential kernels . . . . .	32
2.3.2 Lennard-Jones kernels . . . . .	39
2.4 Quasi-continuum reduction . . . . .	44
2.5 Numerical Examples . . . . .	53
2.5.1 Field Formulation . . . . .	60
2.6 Summary . . . . .	64
<b>III. Real space formulation of Orbital Free DFT . . . . .</b>	<b>68</b>
3.1 Formulation . . . . .	69
3.1.1 Non Local Form . . . . .	70

3.1.2	Orbital Free DFT Kinetic Energy Model . . . . .	72
3.2	Local Reformulation of Orbital Free DFT . . . . .	73
3.2.1	Electrostatics . . . . .	74
3.2.2	Kinetic Energy . . . . .	77
3.3	Atomic Relaxation . . . . .	80
3.4	Summary . . . . .	84
<b>IV.</b>	<b>Real space finite-element implementation . . . . .</b>	<b>85</b>
4.1	Discrete Problem . . . . .	86
4.2	Atomic Relaxation . . . . .	87
4.2.1	Constraints on Atomic Positions . . . . .	88
4.2.2	Cell Relaxation . . . . .	89
4.3	<i>A priori</i> mesh adaption . . . . .	90
4.3.1	Estimate of Energy Error . . . . .	91
4.3.2	Optimal Coarse-Graining Rate . . . . .	97
4.4	Implementation and Results . . . . .	98
4.5	Transferability studies . . . . .	102
<b>V.</b>	<b>Quasi Continuum - Orbital Free DFT . . . . .</b>	<b>109</b>
5.1	Quasi-continuum Orbital Free DFT . . . . .	110
5.2	Benchmark Studies: Vacancy . . . . .	114
<b>VI.</b>	<b>Electronic structure study of an isolated edge dislocation . . . . .</b>	<b>116</b>
6.1	Electronic structure study of an isolated edge dislocation . . . . .	117
<b>VII.</b>	<b>Conclusions . . . . .</b>	<b>133</b>
<b>APPENDICES</b>	<b>. . . . .</b>	<b>139</b>
A.1	Estimate of Energy Error with Kernels . . . . .	140
A.2	Discrete formulation of electrostatic interactions . . . . .	146
<b>BIBLIOGRAPHY</b>	<b>. . . . .</b>	<b>149</b>

## LIST OF FIGURES

### Figure

2.1	Schematic of a 1D mono-atomic chain subjected to affine deformation. The circles in color are atomic-sites enclosed within clusters. . . . .	17
2.2	Schematic of a coarse-grained region in 1D mono-atomic chain: circles denote atoms; circles in red denote representative atoms. Interatomic spacings in the semi-infinite half-chains to the right and left of $A$ are $a_1$ and $a_2$ respectively. . . . .	19
2.3	Schematic of node-based cluster rules in 1D mono-atomic chain: circles in blue denote the atoms belonging to a cluster; shaded triangles represent the shape-functions of representative atoms restricted to the region BC. . . . .	20
2.4	Schematic demonstrating element-based cluster rules: circles in red denote representative atoms while circles in blue denote atoms lying within clusters; clusters are located at the center of elements. . . . .	31
2.5	A fit for kernel $\frac{1}{r^6}$ with an approximate kernel of the form $ae^{-\alpha r} + b\frac{e^{-(\beta r)}}{r} + c\frac{e^{-(\gamma r)}}{r} + d\frac{e^{-(\lambda r)}}{r}$ . . . . .	41
2.6	A fit for kernel $\frac{1}{r^{12}}$ with an approximate kernel of the form $ae^{-\alpha r} + b\frac{e^{-(\beta r)}}{r} + c\frac{e^{-(\gamma r)}}{r} + d\frac{e^{-(\lambda r)}}{r}$ . . . . .	42
2.7	Schematic sketch of meshes: (a) Shows the atomic-mesh, which has atomistic resolution in regions of interest and is coarse-grained elsewhere. The circles in red denote representative atoms. (b) Shows the potential-mesh, used to represent the corrections to the predictor of potential fields. The stars in black represent the nodes of this mesh. It is subatomic in regions of interest and coarse-grains to become superatomic. (c) Shows the fine-mesh which resolves the predictor for the potential fields. The nodes of this mesh are small circles in blue. Unlike $T_{h_1}$ and $T_{h_3}$ which are coarse-grained, $T_{h_2}$ is a uniform subatomic mesh everywhere. . . . .	47

2.8	Schematic showing reduction in computational complexity upon introduction of quadrature rules. (a) Atomic-mesh: circles denote atomic sites; circles in red denote representative atoms (rep-atoms). (b) Potential-mesh and fine-mesh: small circles in blue denote $T_{h_2}$ nodes; stars denote $T_{h_3}$ nodes. The disjoint clusters representing the $T_{h_2}$ mesh is enclosed in a light green box. . . . .	50
2.9	A triangulation showing a superatomic element and a subatomic element in the $T_{h_3}$ mesh. The quadrature rule is exact in such a region. . . . .	50
2.10	Displacement field obtained from an all-atom simulation of a chain of atoms loaded by an indenter. . . . .	54
2.11	Coarse grained mesh with 95 rep-atoms in a chain consisting of 4110 nominal number of atoms. . . . .	55
2.12	Approximation errors in displacement field and total energy for formulation proposed in <i>Knapp and Ortiz</i> (2001). . . . .	56
2.13	Approximation error created due to kinematic constraints (coarse-graining errors) and cluster rules (quadrature errors). . . . .	57
2.14	Approximation errors in displacement field and total energy for formulation proposed in <i>Eidel and Stukowski</i> (2009). . . . .	59
2.15	Convergence study of the self-consistent iteration for residual force correction. Here $\kappa(i)$ is the dead-load at the $i^{th}$ iteration of the self consistent loop and $\ \Delta\kappa(i)\ _2 = \ \kappa(i) - \kappa(i - 1)\ _2$ is the $\ell_2$ norm of change in dead-load against self-consistent iteration number. . . . .	61
2.16	Approximation errors in displacement and energy for the proposed field formulation of quasi-continuum method. $\mathbf{q}^h$ represents coarse-grained displacement field while $\phi^h$ represents coarse-grained potential field. . . . .	65
4.1	Convergence rates for the finite-element approximation of bulk Aluminum using orbital-free DFT with DD kernel energy. . . . .	101
4.2	Computational efficiency of various orders of finite-element approximations. Case study: Aluminum clusters. . . . .	103
6.1	Electron-density contours of a perfect edge dislocation in Aluminum. . . . .	121
6.2	Energy of a perfect edge dislocation as a function of simulation domain size. . . . .	124
6.3	Differential displacement plot of the edge component of Shockley partials. The dotted lines represent the location of the partials, and $d_{edge}$ denotes the partial separation distance. . . . .	125
6.4	Core-energy per unit length of dislocation line of relaxed Shockley partials as a function of macroscopic volumetric strain. . . . .	126
6.5	Core-energy per unit length of dislocation line of relaxed Shockley partials as a function of uniaxial $\epsilon_{11}$ strain. . . . .	126
6.6	Core-energy per unit length of dislocation line of relaxed Shockley partials as a function of macroscopic uniaxial $\epsilon_{22}$ strain. . . . .	126

6.7	Core-energy per unit length of dislocation line of relaxed Shockley partials as a function of macroscopic uniaxial $\epsilon_{33}$ strain. . . . .	127
6.8	Core-energy per unit length of dislocation line of relaxed Shockley partials as a function of macroscopic biaxial $\epsilon_{11} + \epsilon_{22}$ strain. . . . .	127
6.9	Core-energy per unit length of dislocation line of relaxed Shockley partials as a function of macroscopic biaxial $\epsilon_{11} + \epsilon_{33}$ strain. . . . .	127
6.10	Core-energy per unit length of dislocation line of relaxed Shockley partials as a function of macroscopic biaxial $\epsilon_{22} + \epsilon_{33}$ strain. . . . .	128
6.11	Schematics for the two scenarios considered. <i>Case (i)</i> : Edge dislocations aligned along the glide plane. <i>Case (ii)</i> : Dislocations at an angle of $45^\circ$ . . . . .	130



## LIST OF TABLES

### Table

2.1	Table of coefficients for an approximate fitting of $\frac{1}{r^6}$ and $\frac{1}{r^{12}}$ kernels with a kernel of the form $ae^{-\alpha r} + b\frac{e^{-(\beta r)}}{r} + c\frac{e^{-(\gamma r)}}{r} + d\frac{e^{-(\lambda r)}}{r}$ . . . . .	40
4.1	KS-DFT-LDA results for equilibrium total energies ( $E_{min}$ in eV per atom) calculated using TM-NLPS, and OFDFT results for the same using BLPS ( <i>Huang and Carter (2008)</i> ). The energy differences in eV between competing phases and the stable phase are shown. The TM-NLPS data should be viewed as the benchmark. The zero in the first column is to indicate that these numbers form the base against which energies of other phases are determined. . . . .	108
4.2	KS-DFT-LDA results for formation energies ( $E_{min}$ in eV per atom) calculated using TM-NLPS, and OFDFT results for the same using BLPS ( <i>Huang and Carter (2008)</i> ). The TM-NLPS data should be viewed as the benchmark . . . . .	108
5.1	Quasi-continuum Orbital Free DFT bench mark calculations on a perfect crystal with a single vacancy. The QC calculations are compared against explicit Orbital Free DFT calculations. All calculations are performed using the Bulk Local pseudo potential and with WGC kernels. . . . .	114
6.1	Computed elastic constants and intrinsic stacking fault energy ( $\gamma_{isf}$ ) with orbital-free DFT and Kohn-Sham DFT. Both sets of calculations are performed with the Goodwin-Needs-Heine pseudo potential. . .	119
6.2	Computed dislocation energy of perfect edge dislocation in Aluminum for varying domain-sizes, where $N$ denotes the number of atoms in the simulation domain. $\Delta E_d$ denotes the change in the dislocation energy from the previous domain-size, and $\Delta E_d^{elas}$ and $\Delta E_d^{elec}$ denote the elastic and electronic contributions to $\Delta E_d$ . . . . .	123
A.1	Convergence of $E_{electrostatic}^h$ for “HEX8” element . . . . .	147
A.2	Convergence of $E_{electrostatic}^h$ for “HEX125SPECTRAL” element . . .	148

## LIST OF ABBREVIATIONS

**Title** Quasi-continuum reduction of field theories and energetics of defects in Aluminum

**OFDFT** Orbital Free DFT

# ABSTRACT

Quasi-continuum reduction of field theories and energetics of defects in Aluminum

by

Mrinal Iyer

Chair: Vikram Gavini

Defects strongly govern the formation of microstructure in crystalline materials and thus their material properties. Accurate study of defect energetics requires numerical techniques capable of handling a wide range of length scales from the angstrom to the micro-scale by resolution of short-ranged complex atomic re-arrangements at the defect core and long-ranged elastic distortions of the lattice in bulk. We use a three pronged approach to attempt to solve this problem: (a) Orbital Free Density Functional Theory, a fast yet chemically accurate physical model valid for metals with a valence electron density close to a free electron gas (e.g Al, Mg). (b) A real space formulation and a finite element based implementation to naturally couple quantum mechanics with continuum mechanics (c) A coarse grained model that removes cell size restrictions on simulations, thus providing capability to handle millions of atoms. We use this technique to study the defect-core and energetics of an edge dislocation in Aluminum. Our results suggest that the core-size – region with significant contribution of electronic effects to defect energetics – is around ten times the magnitude of the Burgers vector, which is much larger than core-sizes used in continuum

studies. The computed core-structure, representing two Shockley partials, is consistent with other electronic structure and atomistic studies. Interestingly, our study indicates that the core-energy of an edge dislocation has a significant and a highly non-linear response to external macroscopic strains. From this core-energy dependence on macroscopic strains, we infer that interactions between dislocations involve an additional short-ranged force beyond the traditional Peach-Koehler force, and that this force is significant in regions of inhomogenous deformations.

# CHAPTER I

## Introduction

A perfect crystal is an idealization; A perfect crystal does not exist. In reality, materials have defects which make them rather interesting. Mechanical, chemical, electronic and optical properties of crystalline materials are strongly affected by defects in the structure and even the simplest defects create profound effects on the material (c.f. *Reed-Hill and Abbaschian (1973)*). These defects occur over multiple length scales ranging from the angstrom (vacancies) to the micro-scale (precipitates). The lattice distortion that a defect creates is characterized by a core region, with rapidly varying fields, and an elastic tail with slowly varying but long ranged fields. The core region of a defect features sharp changes in the atomic displacement field and in the electron density distribution. This necessitates calculations of quantum mechanical accuracy and correspondingly, knowledge of the electronic structure. The far-field perturbations induced by the core are long ranged, thus placing the demand for large simulations. The twin demands of highly accurate physical models and large scale simulations make this problem computationally challenging. Traditionally, continuum models based on elasticity have been very successful in predicting the asymptotic decay of displacement fields outside the defect core (*Eshelby (1957)*; *Bacon et al. (1980)*). More recently, large scale atomistic calculations (c.f. *Li et al. (2002a, 2004)*) have been used in an attempt to predict the complete displacement

field, including the core region. However these calculations use empirical potentials to describe atomic interactions, and their parameters, which are often fit to bulk properties and some simple defect properties, may not accurately describe the core of a more complex defect. Thus, neither approach can capture physics coming from changes to the electronic structure —sharp disturbances at the core and slow decay, created by the defect. The effect of electronic structure on defect energetics have been barely explored and the extent of this effect is largely unknown. Since the perturbations to the electronic structure are slowly decaying (c.f. *Gavini and Liu (2011)*), typically, volumes containing million of atoms need to be simulated, before the perturbations decay sufficiently. Explicit electronic structure simulations on such large samples are computationally intractable. On the other hand, the challenges presented by the problem can be addressed by multi-scale models that provide electronic structure resolution near the defect core and seamlessly coarsen to a continuum description away from the core, thus substantial computational savings in the process. A family of multi-scale models, based on quasi-continuum reduction, have been developed over the years with the intent of capturing such physics (c.f. *Tadmor et al. (1996a,b); Knap and Ortiz (2001)*). These numerical techniques were originally developed with the purpose of resolving the defect core with atomistic accuracy and coarsening to continuum description in the bulk. With large scale, purely atomistic calculations now becoming routine (and large scale, explicit electronic structure calculations still out of reach), quasi-continuum methods are especially useful in coarse-graining electronic structure calculations. Most early quasi-continuum formulations used different physical models to deal with different length scales and often introduced ad-hoc approaches to couple the physical models. This kind of coupling produced spurious effects and made them unreliable for predictive modeling. A newer class of quasi-continuum models did away with this coupling by introducing a seamless way to coarse-grain a single physical model. However, further approximations, called cluster

rules, introduced within the models to speed up force calculations, were inconsistent for non-local representation of atomic interactions, thus resulting in a lack of systematic reduction of errors with refinement. The first step of my research has been to demonstrate that cluster rules introduced on a non-local representation of energy result in a lack of consistency – approximation errors do not reduce with increasing refinement and then developing a *Field Theoretic* formulation for the quasi-continuum method that resolves the above issue, seamlessly couples multiple length scales using a single physical model and shows a systematic convergence of errors with increasing refinement. Furthermore, the field theoretic nature of the formulation makes it easily transferable to electronic structure models, which are also field based.

Among electronic structure theories, one of the most popular and widely accepted model is the Kohn-Sham approach to the Density Functional Theory (c.f. *Kohn and Sham* (1965)). While very accurate, it is also extremely expensive, with computational cost scaling cubically with the number of electrons in the system. For materials with an electronic structure close to a free electron gas, e.g. Aluminum and Magnesium, a far cheaper, yet accurate flavor called as Orbital Free DFT can be used (c.f. *Wang et al.* (1999)). This field has seen a large body of research over the years, that has produced some extremely fast techniques to perform explicit Density Functional Theory calculations. Many of these implementations achieve their exemplary performance through the use of a Fourier-space formulation and a plane wave basis set to efficiently perform computationally intensive operations through Fast Fourier Transforms. These, however, force the application of periodic boundary conditions, scale poorly on large parallel computing architectures and preclude any use of coarse grained approaches. Since most defect configurations are aperiodic, an increasingly popular approach for Density Functional Theory calculations has involved use of real-space formulations. Among real space techniques, finite-element methods display a number of features that make its application for electronic structure calculations very

attractive. Firstly, it is a general basis set allowing for arbitrary choice of boundary conditions and thus providing a clean solution for a wide variety of physical problems. Secondly, it allows for tailoring of mesh resolution to the physics of the problem, thus allowing development of quasi-continuum methods for coarse graining. Thirdly, complex geometries— a consequence of the elastic fields created by defects – are handled with ease. Lastly, finite-element methods scale very well on large computing platforms. While being attractive on the above counts, finite-element methods suffer from the drawback of requiring a large number of degrees of freedom per atom (often orders more than Fourier space methods). Thus the computational cost of this basis set has been far in excess of the advantage provided by an increase in versatility. So, the second component of my research has been to explore the use of higher-order adaptive finite elements to reduce the degrees of freedom and we find 100-1000 fold increase in computational savings over previous finite-element approaches. With the use of higher order adaptive finite elements, simulation cells containing up to 10,000 atoms can be routinely simulated. While this is a significant improvement over other finite element approaches, these sizes are still insufficient for complex defects. Hence, the final component of my research has been in using quasi-continuum methods to systematically coarse grain Orbital Free DFT. This permits the study of complicated defects in realistic concentrations and we apply this model to study the energetics of an isolated edge dislocation in Aluminum and its response to macroscopic strains. These simulations, with electronic structure accuracy, are the first of their kind and display a strongly non-linear coupling between the dislocation and the applied external macroscopic strains. The strong response of the dislocation to external loads can be attributed to the electronic effects in the core and beyond. From this core-energy dependence on macroscopic strains, we infer that interactions between dislocations involve an additional short-ranged force beyond the traditional Peach-Koehler force, and this force is significant in regions of inhomogenous deformations.



The remainder of this thesis is organized as follows: In chapter II we introduce a Field Theoretic formulation for the quasi-continuum method. In chapter III, we provide the real-space, field formulation for Orbital Free DFT and in chapter IV we discuss the finite-element implementation and computational efficiency gained with the use of a higher-order, adaptive finite-element method. We then build the quasi-continuum method on top of Orbital Free DFT in chapter V to get a systematically coarse-grained electronic structure model. In chapter VI, we apply the quad-continuum Orbital Free DFT model to study the energetics of an isolated edge dislocation in Aluminum. We conclude in chapter VII with directions for future research.

## CHAPTER II

### Quasi Continuum method

The main challenge in an accurate description of defect behavior is the wide range of interacting length-scales that determine the properties of defects. The core of a defect is determined by complex atomistic/quantum-mechanical interactions on an Angstrom length-scale, which in turn produces long-ranged elastic fields over many micrometers. The Quasi-continuum method is a numerical coarse-graining technique that attempts to bridge these various length-scales to accurately describe defect behavior in solids. We refer to the following articles and references therein for a comprehensive overview of the quasi-continuum method and its applications: *Tadmor et al.* (1996b,a); *Miller et al.* (1998a,b); *Phillips et al.* (1999); *Ortiz and Phillips* (1998); *Tadmor et al.* (1999); *Shenoy et al.* (2000); *Knap and Ortiz* (2001); *Miller and Tadmor* (2002); *Knap and Ortiz* (2003); *Curtin and Miller* (2003); *Gavini et al.* (2007a); *Eidel and Stukowski* (2009).

The quasi-continuum (QC) method was originally developed in the context of lattice statics at zero temperature using empirical interatomic potentials (*Tadmor et al.*, 1996b,a), where the key idea was the systematic and adaptive coarse-graining from a fully resolved atomistic description near a defect-core to a continuum description away from the core. This was achieved through kinematic constraints on the degrees of freedom—positions of atoms, thus reducing the variational problem of computing the

ground-state properties to a constrained variational problem with far fewer degrees of freedom. Although the imposed kinematic constraints significantly reduce the number of variables, the computational complexity of evaluating the generalized forces corresponding to the coarse-grained variables—positions of representative atoms—still scales with the total number of atoms in the system making computations on large systems intractable.

Various approximations have been suggested to further reduce the complexity of force computations and make it commensurate with the complexity of coarse-grained variables (*Tadmor et al.*, 1996b,a; *Shenoy et al.*, 1999; *Knap and Ortiz*, 2001; *Miller and Tadmor*, 2002; *Eidel and Stukowski*, 2009). These include the mixed atomistic and continuum formulations, or introduction of cluster summation rules on lattice sums. Valuable as these approximations are, they suffer from notable drawbacks. In some cases, the computed forces are non-conservative which may lead to energy conservation problems as studied in *Shimokawa et al.* (2004). In other cases, where the computed forces are conservative, spurious forces appear as a result of the approximations introduced and can undermine the accuracy of the solution. Many strategies have been suggested to correct the errors incurred in these approximations (cf. e.g. *Shimokawa et al.* (2004); *Weinan et al.* (2006)), but introduce undesirable seams in the process. Further, recent numerical analysis suggests that the approximations introduced may not be consistent and stable, and can result in uncontrolled errors for rapid coarse-graining (*Dobson and Luskin*, 2008; *Dobson et al.*, 2010; *Luskin and Ortner*, 2009).

In the present work we seek to construct a seamless quasi-continuum formulation which is solely based on a single theory, is variational, and provides systematic convergence of the approximations introduced. The notion of cluster summation rules introduced in *Knap and Ortiz* (2001); *Eidel and Stukowski* (2009) is attractive from the standpoint of being a seamless formulation based on a single theory. However, the

formulations based on this approximation are either not variational, or are not consistent as they fail the patch test and thus do not guarantee a systematic convergence of approximations. We demonstrate this through the error estimates we compute in section 2.2. We identify the primary cause of these shortcomings to be the use of the quadrature rules (cluster summation rules), which is a local notion of numerical approximation, on a non-local representation of energy describing the extended interatomic interactions. Further, this non-local representation of the energy is also a cause for the spurious forces observed in the formulation proposed in *Tadmor et al.* (1996b), and subsequent improvements in *Shenoy et al.* (1999); *Miller and Tadmor* (2002).

In this work, we first reformulate the non-local interatomic potentials into a local form by constructing the partial differential equation whose Green’s function corresponds to the kernel of the non-local interaction. Most interatomic potentials are based on either an exponential kernel of the form  $e^{-\alpha|\mathbf{r}-\mathbf{r}'|}$ , or kernels of the form  $\frac{1}{|\mathbf{r}-\mathbf{r}'|^m}$  where  $m$  is an integer. We note that  $e^{-\alpha|\mathbf{r}-\mathbf{r}'|}$  is the Green’s function of the biharmonic equation, and show that kernels of the form  $\frac{1}{|\mathbf{r}-\mathbf{r}'|^m}$  can be approximated with Green’s functions of Helmholtz equations without significant loss of accuracy. Thus, the extended interactions for a large class of interatomic potentials can now be described by a local variational problem involving potential fields, and this forms the basis for the field approach to the quasi-continuum method. In particular, as will be demonstrated in this article, the computation of energy as well as the physical forces on atoms reduce to local evaluations involving potential fields.

Following *Gavini et al.* (2007a), the quasi-continuum reduction is performed on the potential fields which are governed by a local variational problem. The potential fields are first decomposed into predictor fields and corrector fields. The predictor fields are constructed from local periodic calculations using the Cauchy-Born rule. The corrector fields, which are represented on a coarse-grained triangulation, are then

computed from the variational principle. In a related work (*Gavini and Liu, 2011*), we show that the corrector fields do not exhibit oscillations on the length-scale of the atomic lattice which justifies the computation of corrector fields on coarse-grained triangulations. Owing to the local nature of the formulation, we proceed to introduce quadrature rules that reduce all computations to have a complexity commensurate with coarse-grained variables. We show that the quadrature rules introduced on this local variational problem satisfy the consistency conditions for systematic convergence of approximations, which is one of the central results of this work.

To demonstrate the accuracy of the proposed field formulation of the QC method we have numerically implemented the formulation using Morse potential. We compare the numerical results from the proposed formulation with other seamless QC formulations employing node-based cluster rules (*Knap and Ortiz, 2001; Eidel and Stukowski, 2009*) using a nanoindentation test problem in one dimension. We find that errors arising from quadrature approximations are almost negligible in the field formulation, and the approximation error is predominantly the coarse-graining error associated with the kinematic constraints on positions of atoms which can not be surpassed in any QC formulation. These results are in sharp contrast to the approximation errors incurred when cluster summation rules are introduced on a non-local representation of the energy. In such a case, the quadrature errors are orders of magnitude larger than coarse-graining errors, and numerical results suggest a lack of systematic convergence with increasing number of representative atoms. These numerical results support our observations from error analysis, and highlight the strict control and systematic convergence afforded by the field approach to the QC method. We further note that the field approach makes mathematical analysis of QC more amenable, where established techniques from functional analysis can be employed.

## 2.1 Overview

We consider the reference configuration of a single crystallite, where the positions of the  $M$  atoms present in the crystallite are given by a subset of a simple Bravais lattice in a  $d$  dimensional space denoted  $\mathcal{L}$ . Let  $\mathbf{l} = \{l^1, \dots, l^d\} \in \mathbb{Z}^d$  denote the lattice coordinates representing an individual atom. The coordinates of atoms in the reference configuration are thus given by

$$\mathbf{X}_{\mathbf{l}} = \sum_{i=1}^d l^i \mathbf{a}_i, \quad \mathbf{l} \in \mathcal{L}, \quad (2.1)$$

where  $\mathbf{a}_i$  for  $i = 1, \dots, d$  denote the basis vectors of the Bravais lattice. We denote by  $\mathbf{q} = \{\mathbf{x}_{\mathbf{l}}, \mathbf{l} \in \mathcal{L}\}$  a vector that collects the positions of atoms in the deformed configuration. The energy of a material system in atomistic calculations is given by

$$\Pi(\mathbf{q}) = E(\mathbf{q}) + V(\mathbf{q}), \quad (2.2)$$

where  $\Pi$  denotes the total potential energy of the system,  $E$  denotes the internal energy of the system, and  $V$  denotes the potential energy due to body forces acting on the material system. The problem of computing ground-state properties, which include the ground-state energy and the deformed configuration, can now be expressed as the following variational problem:

$$\min_{\mathbf{q} \in X} \Pi(\mathbf{q}), \quad (2.3)$$

where  $X$  denotes the vector space of admissible trial functions corresponding to imposed boundary conditions. We note that the above minimization problem may not have a unique minimizer owing to the non-convex nature of the potential energy function. However, in most numerical simulations the crystallite is loaded incrementally in a quasi-static manner allowing the system to relax to a nearby stable configuration.

The internal energy of the system in atomistic calculations is often described by empirical interatomic potentials, the most common being the embedded atom method (cf. e. g. *Daw and Baskes (1984)*), and has a representation given by

$$E(\mathbf{q}) = \sum_{\mathbf{k} \in \mathcal{L}} \varepsilon_{\mathbf{k}}(\mathbf{q}), \quad (2.4a)$$

$$\varepsilon_{\mathbf{k}}(\mathbf{q}) = \frac{1}{2} \sum_{\mathbf{j} \in \mathcal{L}, \mathbf{j} \neq \mathbf{k}} \bar{K}(|\mathbf{x}_{\mathbf{k}} - \mathbf{x}_{\mathbf{j}}|) + f(\bar{\rho}(\mathbf{k})) \quad \text{with} \quad (2.4b)$$

$$\bar{\rho}(\mathbf{k}) = \sum_{\mathbf{j} \in \mathcal{L}, \mathbf{j} \neq \mathbf{k}} \rho(|\mathbf{x}_{\mathbf{k}} - \mathbf{x}_{\mathbf{j}}|). \quad (2.4c)$$

In the above expression,  $\varepsilon_{\mathbf{k}}(\mathbf{q})$  denotes the internal energy of atom  $\mathbf{k}$ ,  $\bar{K}$  denotes a pairwise potential governing the interatomic interactions,  $f$  denotes the embedding energy function and  $\bar{\rho}(\mathbf{k})$  denotes the electron density at atom  $\mathbf{k}$  in the environment of surrounding atoms. The ground-state properties are computed by equilibrating the forces on atoms given by

$$\mathbf{f}_{\mathbf{k}}(\mathbf{q}) = -\frac{\partial \Pi(\mathbf{q})}{\partial \mathbf{x}_{\mathbf{k}}} \quad \mathbf{k} \in \mathcal{L}. \quad (2.5)$$

Given the extended nature of interatomic interactions—every atom in the crystallite interacts with every other atom, at least within a cut-off radius—the complexity associated with the computation of forces and energy limits the size of accessible material systems. However, the nature of deformation fields in most systems of interest, especially those involving defects, is such that these fields are rapidly varying only near the core of a defect, and become smooth away from the core where the response is effectively elastic. This nature of deformation fields is the basis for the quasi-continuum method which is in spirit, an adaptive numerical coarse-graining technique retaining full resolution where necessary and coarse-graining elsewhere.

A key idea behind quasi-continuum method is to replace the minimization problem in equation (2.5) with a constrained minimization problem in a suitably chosen

sub-space. We consider a subset of *representative* atoms denoted by  $\mathcal{L}_h$  and construct a finite-element triangulation  $T_h$  of these representative atoms in the reference configuration, which in general is unstructured. Further, kinematic constraints are introduced on positions of atoms in the deformed state through shape-functions of the finite-element triangulation given by

$$\mathbf{x}_{\mathbf{k}}^h = \sum_{\mathbf{j} \in \mathcal{L}_h} \Phi^h(\mathbf{X}_{\mathbf{k}}|\mathbf{X}_{\mathbf{j}})\mathbf{x}_{\mathbf{j}}^h, \quad \mathbf{k} \in \mathcal{L} \quad (2.6)$$

where  $\Phi^h(\mathbf{X}_{\mathbf{k}}|\mathbf{X}_{\mathbf{j}})$  denotes the value of the shape-function associated with a representative atom  $\mathbf{j}$  evaluated at the position of atom  $\mathbf{k}$  in the reference configuration. Let  $\mathbf{q}^h = \{\mathbf{x}_{\mathbf{k}}^h, \mathbf{k} \in \mathcal{L}\}$  be a vector containing positions of atoms in the deformed configuration under the kinematic constraint imposed through equation (2.6). The energy of the system is now a function of positions of only the representative atoms, and the minimization problem in equation (2.3) reduces to a constrained minimization problem given by

$$\min_{\mathbf{q}^h \in X_h} \Pi(\mathbf{q}^h), \quad (2.7)$$

where  $X_h$  denotes the subspace of  $X$  spanned by the shape-functions of the finite-element triangulation. A judicious choice of the subspace  $X_h$  corresponds to providing full atomistic resolution in regions of rapidly varying deformation fields, for example at the defect-core, and using fewer representative nodes in regions of smooth deformations. Many numerical tests have shown that the ground-state properties of a system can be represented, without any significant loss of accuracy, by the constrained minimization problem in equation (2.7) which has far fewer degrees of freedom than equation (2.3).



The force on a representative atom at  $\mathbf{j} \in \mathcal{L}_h$  is given by

$$\begin{aligned} \mathbf{f}_j(\mathbf{q}^h) &= -\frac{\partial \Pi(\mathbf{q}^h)}{\partial \mathbf{x}_j^h} = -\sum_{\mathbf{k} \in \mathcal{L}} \frac{\partial \Pi(\mathbf{q}^h)}{\partial \mathbf{x}_k^h} \frac{\partial \mathbf{x}_k^h}{\partial \mathbf{x}_j^h} \\ &= \sum_{\mathbf{k} \in \mathcal{L}} \mathbf{f}_k(\mathbf{q}^h) \Phi^h(\mathbf{X}_k | \mathbf{X}_j), \end{aligned} \quad (2.8)$$

which is a weighted sum of forces of atoms that lie in the compact support of the shape-function associated with representative atom  $\mathbf{j}$ . Thus, although the kinematic constraints introduced in the quasi-continuum method significantly reduce the degrees of freedom, forces on all atoms in the system are required to compute forces on representative atoms. A full atomistic force calculation is prohibitively expensive on large systems and further approximations are necessary to reduce the computational complexity of these force calculations. We note that the kinematic constraints introduced through the selection of representative atoms is common to all versions of the quasi-continuum method developed so far (cf. e. g. *Tadmor et al. (1996b)*; *Shenoy et al. (1999)*; *Knap and Ortiz (2001)*; *Miller and Tadmor (2002)*; *Eidel and Stukowski (2009)*). The various versions of the method differ in the next approximation which is introduced to reduce the computational complexity of the force calculation. Here we briefly discuss and comment on the merits and demerits of commonly used formulations proposed in *Tadmor et al. (1996b)* and *Knap and Ortiz (2001)*, and a recent formulation proposed in *Eidel and Stukowski (2009)*.

In the first formulation of quasi-continuum method, proposed in *Tadmor et al. (1996b)*, the domain of analysis was divided into two regions—the non-local region where the energy is described by empirical interatomic potentials with extended interactions, and the local region where the energy is described by invoking the Cauchy-Born rule. The force computations are expensive only in the non-local region which is small compared to the local region, thus reducing the computational complexity of the calculation. However, the heterogeneous and disparate models used in different

regions of the domain result in spurious forces on the interface between the local and the non-local region, and are often referred to as *ghost forces* in the literature. *Shenoy et al.* (1999) proposed to remove the effect of these ghost forces by adding a dead load which is the negative of these ghost forces. But the drawback of this approach is that these dead loads are non-conservative and may lead to energy conservation problems (*Shimokawa et al.*, 2004) in molecular dynamics simulations. *Shimokawa et al.* (2004); *Weinan et al.* (2006) suggest a remedy to this problem by introducing a buffer region or using local reconstructions between the local and the non-local region, but in the process introduce undesirable seams in the formulation.

A seamless approach to reduce the computational complexity of the force calculations was proposed in *Knap and Ortiz* (2001). In the spirit of quadrature rules, the force computations are approximated by *cluster summation rules* that represent a weighted sampling of forces on atoms located in clusters centered at representative atoms. Although this formulation is free of ghost forces, the approximate forces are non-conservative (*Eidel and Stukowski*, 2009) which is not desirable as mentioned before. *Eidel and Stukowski* (2009) suggest introducing cluster summation rules only on the energy, and calculating the forces on representative atoms as tangents of this approximate energy. However, this leads to the appearance of non-zero residual forces for a perfect crystal even under affine deformations. These residual forces can become uncontrollably large for an arbitrary coarse-graining of representative nodes as will be demonstrated in section 2.2.2, and in turn will produce a spurious displacement field upon relaxation. It is suggested in *Eidel and Stukowski* (2009) that these residual forces can be eliminated by introducing dead loads on similar lines as proposed in *Shenoy et al.* (1999). The difference between ghost forces in *Tadmor et al.* (1996b) and the residual forces in *Eidel and Stukowski* (2009) is that the former are non-conservative while the latter are conservative. We note that calculation of dead loads requires evaluation of exact forces which is an expensive calculation. Since dead loads

change with the displacement field, they have to be updated periodically and solved for in a self-consistent manner. We demonstrate in this article through numerical examples that the self-consistent iterations do not always converge.

The introduction of cluster summation rules in *Knap and Ortiz* (2001) and *Eidel and Stukowski* (2009) in the spirit of quadrature rules is based on systematic numerical approximation, in contrast to the formulation proposed in *Tadmor et al.* (1996b) and its subsequent improvements (*Shimokawa et al.*, 2004) where different regions of the model are described by heterogeneous theories. However, numerical examples in a bench mark test conducted recently (*Miller and Tadmor*, 2009) show that errors in the node-based cluster formulations (*Knap and Ortiz*, 2001; *Eidel and Stukowski*, 2009) are considerably larger than other formulations. We provide a plausible explanation to these observations in section 2.2, where we demonstrate using error analysis that node-based cluster rules can have uncontrollably large errors for rapid coarse-graining and large element sizes. We further show that element-based cluster rules (*Gunzburger and Zhang*, 2010)—where the quadrature rules are introduced inside the element—exhibit better approximation properties for both forces and energy, and reduce to the Cauchy-Born rule for large elements in the leading order. A recent analysis based on nearest-neighbor interactions in one dimension (1D) (*Luskin and Ortner*, 2009) also draws similar conclusions.

The next observation we present is the primary cause of the above mentioned inconsistencies in various versions of quasi-continuum method. We note that it is desirable to introduce cluster (quadrature) rules on the energy and compute forces as tangents of this approximate energy—this guarantees conservative forces. Further, any cluster rule introduced should satisfy the following consistency conditions for systematic convergence (cf. e. g. *Strang and Fix* (1973); *Weinan et al.* (2006)):

- C1. The energy is summed exactly for affine deformations of perfect lattice.
- C2. The computed forces—tangents of the energy—are zero for affine deformations

of perfect lattice.

The consistency condition C2 is often referred to as *patch test* in numerical analysis of approximation theories. We remark that if the energy has a local representation, then C1 implies C2. However, if the energy has a non-local representation then the patch test is never passed by a cluster rule of any order. We consider the following example to illustrate this key point. As shown in the figure 2.1, consider a mono-atomic chain of atoms with uniform spacing between the atoms (affine deformation in 1D), and let  $\Omega$  denote the domain of analysis which consists of  $M$  atoms. First, we consider a *local representation* for the energy given by a lattice function  $\varepsilon(x_i)$ , which denotes the energy of an atom at position  $x_i$ . Using cluster summation rules the lattice sum describing the energy can be approximated as

$$E = \sum_{\substack{i \in \mathcal{L} \\ x_i \in \Omega}} \varepsilon(x_i) \approx \sum_{k=1}^m n_k \sum_{i \in C_k} \varepsilon(x_i) = \tilde{E} \quad (2.9)$$

where  $\tilde{E}$  denotes the approximate energy,  $C_k$  denotes the collection of atoms in the  $k^{\text{th}}$  cluster with a weight  $n_k$ , and  $m$  denotes the number of clusters. Similar to numerical approximation of integrals, the cluster weights and position of these clusters can be chosen such that the approximation is exact for polynomial lattice functions of order  $p$ —a  $p^{\text{th}}$  order accurate cluster rule. Now we consider the directional derivative of the energy for infinitesimal deformations  $\psi_\epsilon : \Omega \rightarrow \Omega$ , with  $\frac{d\psi_\epsilon}{d\epsilon}|_{\epsilon=0} = \Gamma$ . The generalized force is given by

$$f = \sum_{\substack{i \in \mathcal{L} \\ x_i \in \Omega}} \frac{d}{d\epsilon} \left\{ \varepsilon(x_i + \psi_\epsilon(x_i)) \right\} \Big|_{\epsilon=0} = \sum_{\substack{i \in \mathcal{L} \\ x_i \in \Omega}} \varepsilon'(x_i) \Gamma, \quad (2.10)$$

and the approximate generalized force, which is the directional derivative of  $\tilde{E}$ , is

given by

$$\tilde{f} = \sum_{k=1}^m n_k \sum_{i \in C_k} \frac{d}{d\epsilon} \left\{ \varepsilon(x_i + \psi_\epsilon(x_i)) \right\} \Big|_{\epsilon=0} = \sum_{k=1}^m n_k \sum_{i \in C_k} \varepsilon'(x_i) \Gamma. \quad (2.11)$$

From translational invariance of the mono-atomic chain, we note that  $\varepsilon(x_i) = C$ , a constant for  $i \in \mathcal{L}$ . Thus, a zeroth order cluster rule is sufficient to ensure that the energy is summed exactly (C1). Also, it follows that  $\varepsilon'(x_i) = 0$  and the cluster rule immediately passes the patch test (C2).

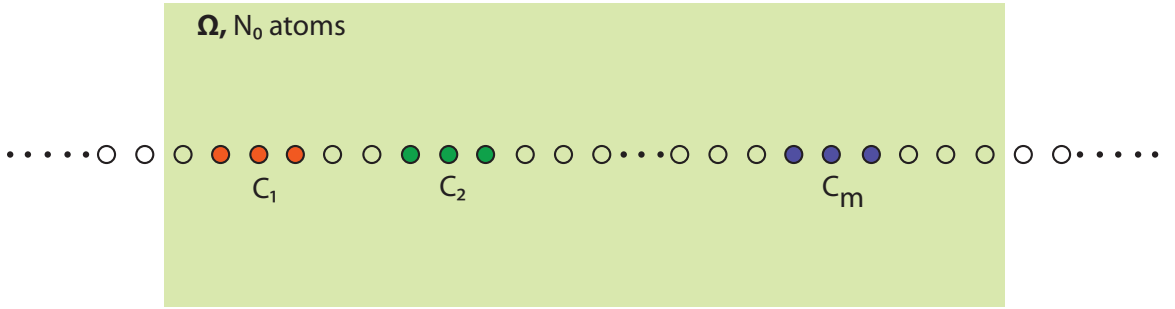


Figure 2.1: Schematic of a 1D mono-atomic chain subjected to affine deformation. The circles in color are atomic-sites enclosed within clusters.

Next, we will consider a *non-local* energy and demonstrate that a cluster rule of any order will not pass the patch test. Consider a non-local energy given by

$$E = \sum_{\substack{i \in \mathcal{L} \\ x_i \in \Omega}} \varepsilon(x_i), \quad \text{where} \quad (2.12a)$$

$$\varepsilon(x_i) = \sum_{\substack{j \in \mathcal{L} \\ j \neq i}} \bar{K}(|x_i - x_j|) \quad (2.12b)$$

and  $\bar{K}$  denotes the kernel representing extended interactions. The approximate energy is still given by equation (2.9), where a zeroth order quadrature rule is sufficient to ensure the consistency condition on energy (C1). The approximate force for this

non-local representation of energy is given by

$$\tilde{f} = \sum_{k=1}^m n_k \sum_{i \in C_k} \varepsilon'(x_i) \Gamma + \sum_{j \in \mathcal{L}} \Gamma \left\{ \sum_{k=1}^m n_k \sum_{\substack{i \in C_k \\ i \neq j}} \bar{K}'(|x_i - x_j|) \frac{x_j - x_i}{|x_j - x_i|} \right\}, \quad (2.13)$$

where  $\varepsilon'(x_i) = \sum_{\substack{j \in \mathcal{L} \\ j \neq i}} \bar{K}'(|x_i - x_j|) \frac{x_i - x_j}{|x_j - x_i|}$ . We note that the first term in the above expression vanishes as  $\varepsilon'(x_i) = 0$  from symmetry. However, for arbitrary  $\Gamma$ , the second term will not vanish for a cluster rule of any order, unless these clusters overlap to cover the complete domain. Error estimates derived in sections 2.2.2 and 2.2.3 to follow reinforce this key point. We note that this failure of patch test is not a deficiency of the cluster rules, but the result of an inconsistency in adopting a local concept of quadrature rules on a non-local representation of energy. We resolve this key issue by reformulating the extended interatomic interactions into a local variational form by solving for potential fields corresponding to these interactions (section 2.3) and subsequently introduce the quasi-continuum reduction of these fields (section 2.4).

## 2.2 Error Analysis

We begin by establishing error estimates for node-based cluster summation rules used in *Knap and Ortiz (2001)* and *Eidel and Stukowski (2009)*. Later in this section we demonstrate that element-based cluster summation rules (*Gunzburger and Zhang, 2010*)—clusters present in the interior of finite-elements—are more accurate in comparison to node-based cluster rules. More importantly, we show through these error estimates that neither approximations pass the patch test for an arbitrary coarse-graining of representative atoms, and thus a systematic convergence of these approximations can not be guaranteed.

We restrict our analysis to 1D where the estimates can be obtained in a form that will demonstrate the main attributes of these errors. To this end, we consider

an infinite mono-atomic chain of atoms with differing deformation gradients,  $F_1$  and  $F_2$ , in the two semi-infinite half-chains (figure 2.2). We consider three representative nodes as shown in figure 2.2 and we are interested in the force on representative atom denoted as  $A$ , and the energy of atoms lying between representative atoms denoted as  $B$  and  $C$ . The representative nodes are chosen such that there are  $N$  atoms in element  $BA$  and  $Ny$  atoms in element  $AC$ , where  $y > 1$  denotes the rate of coarse-graining. We assume without loss of generality that  $Ny$  is an integer. The present construction is a simplified representation of the coarse-grained region in a quasi-continuum formulation, as the deformations are in general different in elements lying to the left of  $B$  and right of  $C$ . To estimate the errors we further assume the following:

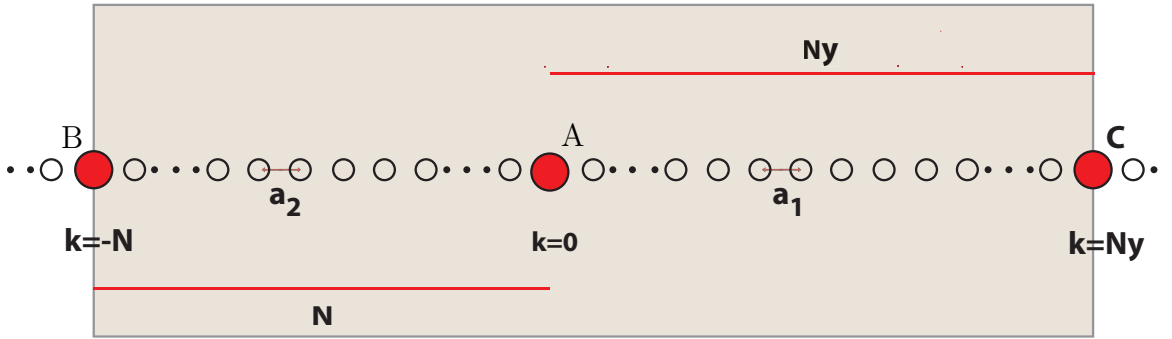


Figure 2.2: Schematic of a coarse-grained region in 1D mono-atomic chain: circles denote atoms; circles in red denote representative atoms. Interatomic spacings in the semi-infinite half-chains to the right and left of  $A$  are  $a_1$  and  $a_2$  respectively.

A1. The energy of the system is given  $E = \sum_{i \in \mathcal{L}} \sum_{\substack{j \in \mathcal{L} \\ j \neq i}} \bar{K}(|x_i - x_j|)$ , where the kernel  $\bar{K}(|x_i - x_j|)$  denotes a central potential representing extended interatomic interactions. Beyond a threshold distance  $r_{th}$ , measured in units of undeformed interatomic spacing  $a$ , the central potential has a decay given by  $\bar{K}(|x_i - x_j|) = \frac{1}{|x_i - x_j|^p}$ , where  $p$  is the decay exponent such that  $p > 2$ .

A2. The difference in deformation gradients in elements  $BA$  and  $AC$  is small— $F_1 \approx F_2$ . For convenience, we denote the interatomic spacing in  $AC$  as  $a_1 = F_1 a$ , and the interatomic spacing in  $BA$  as  $a_2 = F_2 a$ . Thus  $a_1 \approx a_2$ .

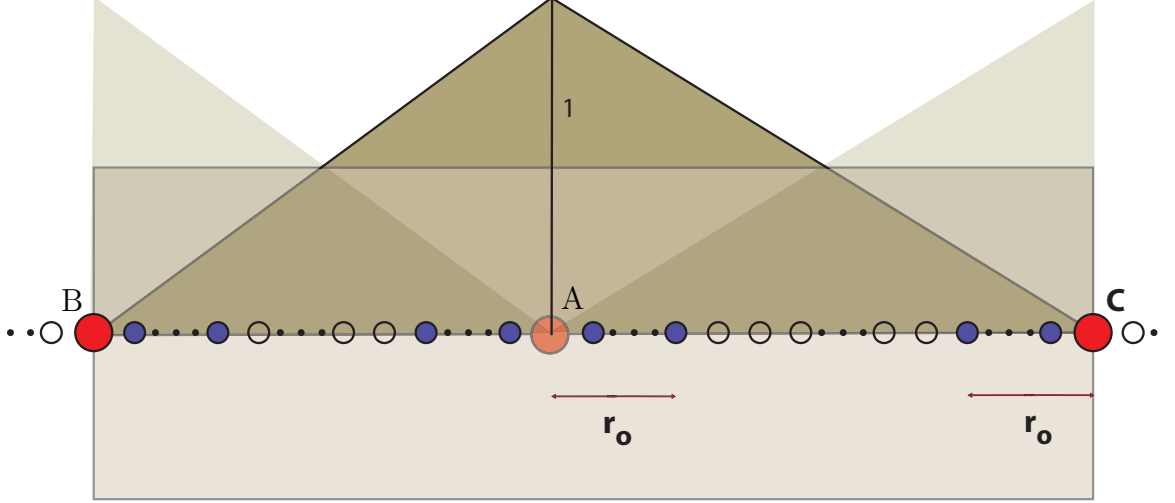


Figure 2.3: Schematic of node-based cluster rules in 1D mono-atomic chain: circles in blue denote the atoms belonging to a cluster; shaded triangles represent the shape-functions of representative atoms restricted to the region BC.

A3. We consider  $N \gg r_0$ , where  $r_0$ , measured in units of undeformed interatomic spacing, is the radius of all clusters introduced in cluster summation rules. Further, we will assume  $r_0 \gg 1$  unless specified otherwise.

### 2.2.1 Node-based cluster rules for lattice sums

We first compute the errors in node-based cluster summations proposed in *Knap and Ortiz* (2001) where cluster rules are employed on lattice sums of both forces and energy independently. In node-based cluster formulations, clusters are centered at the representative nodes as shown in figure 2.3. We begin by estimating approximation errors in force computations arising from the use of cluster summation rules, and subsequently estimate approximation errors in energy computation. The approximate force on any representative atom  $K \in \mathcal{L}_h$  is given by

$$\tilde{f}_K = -2 \sum_{J \in \mathcal{L}_h} n_J \sum_{k \in C_J} g(k) \Phi^h(X_k | X_K), \quad (2.14)$$



where  $\mathcal{L}_h \subset \mathcal{L}$  is a collection of representative atoms in the chain,  $C_J$  denotes the set of atoms located in the cluster centered at representative atom  $J$  with a cluster weight of  $n_J$ . Cluster weights are computed such that shape-functions of the finite-element triangulation of representative atoms are summed exactly (*Knap and Ortiz, 2001*). Further  $g(k) = \sum_{\substack{j \in \mathcal{L} \\ j \neq k}} \bar{K}'(|x_k - x_j|) \frac{x_k - x_j}{|x_k - x_j|}$ , and  $\bar{K}'(|x_k - x_j|)$  decays as  $\frac{1}{|x_k - x_j|^{p+1}}$  (up to a constant factor) from assumption A1.  $\Phi^h(X_k|X_K)$  denotes the value of the shape-function associated with representative atom  $K$  evaluated at atom  $k$ .

We first estimate  $g(k)$  before computing an estimate for the approximate force in equation (2.14). To this end we note the following bounds of the  $p$ -series which appear repeatedly in the estimates to follow:

$$S(k) = \sum_{t=k+1}^{\infty} \frac{1}{t^p} \geq \int_{k+1}^{\infty} \frac{dy}{y^p} = \frac{1}{(p-1)(k+1)^{p-1}} \quad k > 1 \quad (2.15a)$$

$$S(k) = \sum_{t=k+1}^{\infty} \frac{1}{t^p} \leq \int_k^{\infty} \frac{dy}{y^p} = \frac{1}{(p-1)k^{p-1}} \quad k > 1 \quad (2.15b)$$

The lower bound and the upper bound for  $p > 1$  will approach each other for large  $k$ . In the computation of error estimates below, for  $k > r_{th2}$  (a threshold distance) we will approximate the  $p$ -series with their upper bound

$$S(k) = \frac{1}{(p-1)k^{p-1}} + O\left(\frac{1}{k^p}\right). \quad (2.16)$$

We define  $r' = \max\{r_{th}, r_{th2}\}$  and assume  $r_0 \gg r'$  for simplicity. We now proceed to

estimate the force  $g(k)$  on atom  $k$ . For  $k \geq r'$ , using symmetry and assumption A1

$$\begin{aligned}
g(k) &= \sum_{t=k+1}^{\infty} \frac{1}{(ta_1)^{p+1}} - \frac{1}{(ka_1 + (t-k)a_2)^{p+1}} \\
&= \sum_{t=k+1}^{\infty} \frac{1}{t^{p+1}} \left\{ \frac{1}{a_1^{p+1}} - \frac{1}{((a_1 - a_2)\frac{k}{t} + a_2)^{p+1}} \right\} \\
&= \left( \sum_{t=k+1}^{\infty} \frac{1}{t^{p+1}} \right) \left( \frac{1}{a_1^{p+1}} - \frac{1}{a_2^{p+1}} \left\{ 1 + O\left(\frac{a_2 - a_1}{a_2}\right) \right\} \right) \frac{(a_2 - a_1)}{a_2} \ll 1 \quad \text{from A2} \\
&= \frac{1}{pk^p} \left( \frac{1}{a_1^{p+1}} - \frac{1}{a_2^{p+1}} \right) \tag{2.17}
\end{aligned}$$

Similarly we obtain for  $k \leq -r'$ ,

$$g(k) = \frac{1}{p(-k)^p} \left( \frac{1}{a_1^{p+1}} - \frac{1}{a_2^{p+1}} \right) \tag{2.18}$$

Now we estimate the approximate force on the representative atom  $K = 0$  using cluster summation rules. Using equations (2.14), (2.17)-(2.18) we get

$$\begin{aligned}
-\frac{\tilde{f}_0}{2} &= n_0 \sum_{k=0}^{r'} g(k) \left(1 - \frac{k}{Ny}\right) + n_0 \sum_{k=1}^{r'} g(-k) \left(1 - \frac{k}{N}\right) + \alpha n_0 \sum_{k=r'+1}^{r_0} \frac{1 - \frac{k}{Ny}}{k^p} \\
&\quad + \alpha n_0 \sum_{k=r'+1}^{r_0} \frac{1 - \frac{k}{N}}{k^p} + \alpha n_{-N} \sum_{k=N-r_0}^N \frac{1 - \frac{k}{N}}{k^p} + \alpha n_{Ny} \sum_{k=Ny-r_0}^{Ny} \frac{1 - \frac{k}{Ny}}{k^p} \\
&= n_0 \sum_{k=-r'}^{r'} g(k) + \frac{2\alpha n_0}{p-1} \left( \frac{1}{(r'+1)^{p-1}} - \frac{1}{r_0^{p-1}} \right) + O\left(\frac{1}{N}\right) \quad (\text{for } N \gg r_0 \gg 1 \text{ by A3}) \tag{2.19}
\end{aligned}$$

In the above expression  $\alpha = \frac{1}{p} \left( \frac{1}{a_1^{p+1}} - \frac{1}{a_2^{p+1}} \right)$ . Using the same approach, the exact force (without cluster summation rules) on the representative atom  $K = 0$  is computed to be

$$-\frac{f_0}{2} = \sum_{k=-r'}^{r'} g(k) + \frac{2\alpha}{(p-1)(r'+1)^{p-1}} + O\left(\frac{1}{N}\right) \tag{2.20}$$

Thus an estimate for the error in the force calculation using node-based cluster rules

is given by

$$f_0 - \tilde{f}_0 = 2(n_0 - 1) \left\{ \sum_{k=-r'}^{r'} g(k) + \frac{2\alpha}{(p-1)(r'+1)^{p-1}} \right\} - \frac{4\alpha n_0}{(p-1)r_0^{p-1}} \quad (2.21)$$

We now discuss some attributes of the error estimate in equation (2.21). Firstly we note that the error will vanish if  $F_1 = F_2$ , as in this case  $\alpha = 0$  and  $g(k) = 0 \forall k$ . But if  $F_1 \neq F_2$ , then the forces can become arbitrarily large for large elements. This follows from the fact that  $n_0$  scales as  $\frac{N(1+y)}{4r_0}$  for  $N \gg r_0 \gg 1$ . The reason for this uncontrolled error is that forces on atoms drop rapidly away from the element boundary. But the cluster weights are computed such that shape-functions are summed exactly, which is a suitable quadrature rule if the forces are distributed evenly, but results in highly inaccurate forces otherwise.

We now turn to the computation of error estimates when node-based cluster summation rules are employed on lattice sums appearing in the evaluation of the energy of a system. We first compute the exact energy of atoms in elements  $BA$  and  $AC$ . We denote by  $\varepsilon_1$  and  $\varepsilon_2$  the energy per atom in an infinite chain with interatomic spacings  $a_1$  and  $a_2$  respectively. The exact energy is then given by

$$\begin{aligned} E &= \sum_{k=0}^{Ny} \varepsilon(k) + \sum_{k=1}^N \varepsilon(-k) \\ &= \sum_{k=0}^{Ny} \Delta\varepsilon(k) + \sum_{k=1}^N \Delta\varepsilon(-k) + Ny\varepsilon_1 + N\varepsilon_2, \end{aligned} \quad (2.22)$$

where  $\varepsilon(k)$  is the energy of atom  $k$  in the environment of its neighbors, and  $\Delta\varepsilon(k) = \varepsilon(k) - \varepsilon_1, \Delta\varepsilon(-k) = \varepsilon(-k) - \varepsilon_2$ . We now compute  $\Delta\varepsilon(k)$  and  $\Delta\varepsilon(-k)$  for  $k > r'$ .

Following on similar lines as our estimate in equations (2.17)-(2.18),

$$\begin{aligned}
\Delta\varepsilon(k) &= \sum_{t=k+1}^{\infty} \frac{1}{(ka_1 + (t-k)a_2)^p} - \frac{1}{(ta_1)^p} \\
&= \sum_{t=k+1}^{\infty} \frac{1}{t^p} \left\{ \frac{1}{(a_2 + \frac{k}{t}(a_1 - a_2))^p} - \frac{1}{a_1^p} \right\} \\
&= \sum_{t=k+1}^{\infty} \frac{1}{t^p} \left( \frac{1}{a_2^p} - \frac{1}{a_1^p} \right) = \frac{1}{(p-1)k^{p-1}} \left( \frac{1}{a_2^p} - \frac{1}{a_1^p} \right) \quad (2.23)
\end{aligned}$$

$$\Delta\varepsilon(-k) = \frac{1}{(p-1)k^{p-1}} \left( \frac{1}{a_1^p} - \frac{1}{a_2^p} \right) = -\Delta\varepsilon(k) \quad (2.24)$$

The energy of atoms in elements  $BA$  and  $AC$  can now be estimated using equations (2.23)-(2.24) as

$$\begin{aligned}
E &= (Ny)\varepsilon_1 + N\varepsilon_2 + \sum_{k=-r'}^{r'} \Delta\varepsilon(k) + \sum_{k=r'+1}^N \Delta\varepsilon(-k) + \sum_{k=r'+1}^{Ny} \Delta\varepsilon(k) \\
&= (Ny)\varepsilon_1 + N\varepsilon_2 + \sum_{k=-r'}^{r'} \Delta\varepsilon(k) + \sum_{k=N}^{Ny} \Delta\varepsilon(k) \quad (\text{from equation (2.24)}) \\
&= (Ny)\varepsilon_1 + N\varepsilon_2 + \sum_{k=-r'}^{r'} \Delta\varepsilon(k) + \beta \left( \frac{1}{N^{p-2}} - \frac{1}{(Ny)^{p-2}} \right) \\
&\quad (\text{from equation (for } p > 2 \text{ and 2.16)}) \\
&= (Ny)\varepsilon_1 + N\varepsilon_2 + \sum_{k=-r'}^{r'} \Delta\varepsilon(k) + O\left(\frac{1}{N^{p-2}}\right) \quad (2.25)
\end{aligned}$$

where  $\beta = \frac{1}{(p-1)(p-2)} \left( \frac{1}{a_2^p} - \frac{1}{a_1^p} \right)$ . We now proceed to estimate the energy computed using node-based cluster summation rules. The expression for energy of the system upon using cluster summation rules for the lattice sums is given by

$$\tilde{E} = \sum_{J \in \mathcal{L}_h} n_J \sum_{k \in C_J} \varepsilon(k), \quad (2.26)$$

where  $\varepsilon(k) = \sum_{\substack{j \in \mathcal{L} \\ j \neq k}} K(|x_k - x_j|)$ . In the present analysis of 1D mono-atomic chain

with three representative atoms, this reduces to

$$\begin{aligned}
\tilde{E} &= (n_{-N} + n_0)\varepsilon_2 r_0 + (n_{Ny} + n_0)\varepsilon_1 r_0 + n_0 \sum_{k=-r_0}^{r_0} \Delta\varepsilon(k) \\
&\quad + n_{-N} \sum_{k=N-r_0}^N \Delta\varepsilon(-k) + n_{Ny} \sum_{k=Ny-r_0}^{Ny} \Delta\varepsilon(k) \\
&= (n_{-N} + n_0)\varepsilon_2 r_0 + (n_{Ny} + n_0)\varepsilon_1 r_0 + n_0 \left( \sum_{k=-r_0}^{-r'-1} \Delta\varepsilon(k) + \sum_{k=-r'}^{r'} \Delta\varepsilon(k) \right) \\
&\quad + \sum_{k=r'+1}^{r_0} \Delta\varepsilon(k) + O\left(\frac{1}{N^{p-2}}\right) \\
&= (n_{-N} + n_0)\varepsilon_2 r_0 + (n_{Ny} + n_0)\varepsilon_1 r_0 + n_0 \sum_{k=-r'}^{r'} \Delta\varepsilon(k) \\
&\quad \text{(as } \Delta\varepsilon(k) = -\Delta\varepsilon(-k) \text{ for } k > r').
\end{aligned} \tag{2.27}$$

We note that for  $N \gg r_0 \gg 1$ , the expressions for cluster weights, computed by enforcing that shape-functions are summed exactly, reduce to

$$n_{-N} = \frac{N}{2r_0}, \quad n_0 = \frac{N(1+y)}{4r_0}, \quad n_{Ny} = \frac{Ny}{2r_0}. \tag{2.28}$$

Using equations (2.25)-(2.28), we estimate the approximation error in the energy evaluation using node-based cluster rules to be

$$\tilde{E} - E = \frac{N(y-1)}{4}(\varepsilon_2 - \varepsilon_1) + (n_0 - 1) \sum_{k=-r'}^{r'} \Delta\varepsilon(k) \tag{2.29}$$

From the above estimate it is evident that the error in the energy evaluation upon using cluster summation rules vanishes when  $F_1 = F_2$ , as in this case  $\varepsilon_1 = \varepsilon_2$  and  $\Delta\varepsilon(k) = 0, k \in \mathcal{L}$ . However, if  $F_1 \neq F_2$  the error can grow arbitrarily large for large element sizes, which is not desirable. The nature of approximation error in energy computation is similar to the approximation error in force evaluation given by

equation (2.21). Further, as the cluster summation rules are used on lattice sums for forces and energy independently, the approximate forces are non-conservative.

## 2.2.2 Node-based cluster rules on energy

The non-conservative nature of approximate forces in the formulation proposed in *Knap and Ortiz* (2001) is a result of employing cluster summation rules directly on forces as opposed to computing the forces as tangents of an approximate energy. To resolve this deficiency in the formulation, *Eidel and Stukowski* (2009) have proposed to introduce cluster summation rules only on the energy of a system (equation (2.26)) and compute the forces as the tangents of this approximate energy. The approximation error in the energy has been computed in section 2.2.1 and is given by equation (2.29). We now estimate the approximation errors in forces for this formulation. Using the notation introduced in section 2.2.1, the approximate force on a representative atom  $K$  is given by

$$\tilde{f}_K = \sum_{J \in \mathcal{L}_h} n_J \sum_{k \in C_J} \left( \sum_{\substack{j \in \mathcal{L} \\ j \neq k}} f_{kj} \Phi^h(X_j | X_K) - \Phi^h(X_k | X_K) \sum_{\substack{j \in \mathcal{L} \\ j \neq k}} f_{kj} \right), \quad (2.30)$$

where  $f_{kj} = \bar{K}'(|x_k - x_j|) \frac{x_k - x_j}{|x_k - x_j|}$ . We will restrict our analysis to the special case of  $F_1 = F_2$ , which, as will be demonstrated, produces the leading order error for this formulation. We note that the second term in the above expression vanishes as  $\sum_{\substack{j \in \mathcal{L} \\ j \neq k}} f_{kj} = 0$  for affine deformations. Thus the non-zero contribution to the approximate force, which is also the approximation error as the exact force is zero, comes from the first term in the expression. We denote  $g(k) = \sum_{\substack{j \in \mathcal{L} \\ j \neq k}} f_{kj} \Phi^h(X_j | X_0)$  and estimate  $g(k)$  for  $\{-r_0, \dots, r_0\}$ . We remark that the value of  $g(k)$  for  $k \in \{-N, \dots, -N + r_0\} \cup \{Ny - r_0, \dots, Ny\}$  is small compared to the value of  $g(k)$  for  $k \in \{-r_0, \dots, r_0\}$ , and can be neglected as it will only result in a relative error of  $O(\frac{1}{N})$  as seen in section 2.2.1. For the central potential we are considering in this

analysis ( $\overline{\mathbb{K}}(|x_i - x_j|)$ ), the expression for  $g(k)$ ,  $k \in \{-r_0, \dots, r_0\}$ , is given by

$$\begin{aligned}
g(k) &= \sum_{j=k+1}^{Ny} \overline{\mathbb{K}}'(a_1|j-k|) \frac{Ny-j}{Ny} \\
&\quad - \left\{ \sum_{j=0}^{k-1} \overline{\mathbb{K}}'(a_1|j-k|) \frac{Ny-j}{Ny} + \sum_{j=1}^N \overline{\mathbb{K}}'(a_1|j+k|) \frac{N-j}{N} \right\} \quad k > 0 \\
g(-k) &= - \sum_{j=k+1}^N \overline{\mathbb{K}}'(a_1|j-k|) \frac{N-j}{N} + \left\{ \sum_{j=0}^{k-1} \overline{\mathbb{K}}'(a_1|j-k|) \frac{N-j}{N} \right. \\
&\quad \left. + \sum_{j=1}^{Ny} \overline{\mathbb{K}}'(a_1|j+k|) \frac{Ny-j}{Ny} \right\} \quad k > 0 \\
g(0) &= \sum_{j=1}^{Ny} \overline{\mathbb{K}}'(a_1j) \frac{Ny-j}{Ny} - \sum_{j=1}^N \overline{\mathbb{K}}'(a_1j) \frac{N-j}{N}
\end{aligned}$$

For brevity, we further define  $s(k) = g(k) + g(-k)$  for  $k = 0, 1, \dots, r_0$ . Upon rearranging, we obtain

$$\begin{aligned}
s(k) &= \sum_{j=N}^{Ny} (\overline{\mathbb{K}}'(a_1|j-k|) + \overline{\mathbb{K}}'(a_1|j+k|)) \left(1 - \frac{j}{Ny}\right) + \left(\frac{1}{N} - \frac{1}{Ny}\right) z(k) \quad \text{where} \\
z(k) &= \sum_{j=k+1}^N \overline{\mathbb{K}}'(a_1|j-k|)j - \sum_{j=0}^{k-1} \overline{\mathbb{K}}'(a_1|j-k|)j + \sum_{j=1}^N \overline{\mathbb{K}}'(a_1|j+k|)j \quad \text{for } k = 1 \dots r_0 \\
z(0) &= 2 \sum_{j=1}^N \overline{\mathbb{K}}'(a_1j)j.
\end{aligned} \tag{2.31}$$

Noting  $N \gg r_0$ , and using the decay for central potential in assumption A1 along with the properties of p-series (equation 2.16), the first term in  $s(k)$  is  $O(\frac{1}{N^p})$  which is higher order compared to the second term and we drop it for simplicity. Thus,  $s(k) = (\frac{1}{N} - \frac{1}{Ny})z(k)$ . Finally, the approximation error in the computation of force

on representative atom  $K = 0$  can now be expressed as

$$\begin{aligned} \tilde{f}_0 - f_0 = \tilde{f}_0 &= n_0 \left( \frac{1}{N} - \frac{1}{Ny} \right) \left\{ \frac{1}{2} z(0) + \sum_{k=1}^{r_0} z(k) \right\} \\ &= \frac{(1+y)}{4r_0} \left( 1 - \frac{1}{y} \right) \left\{ \frac{1}{2} z(0) + \sum_{k=1}^{r_0} z(k) \right\} \end{aligned} \quad (2.32)$$

We remark that  $z(k)$  is  $O(1)$  for  $k = 0, 1 \dots r_0$ , and from equation (2.32) it is evident that  $\tilde{f}_0 \neq 0$  for  $y \neq 1$ . Further, with increasing  $y$  the force increases and can become uncontrollably large for rapid rates of coarse grain. Thus, even in the case of an affine deformation in the chain, where the energy approximation using cluster rules is exact, the resulting forces computed as derivatives of the approximate energy are non-zero. This indicates the failure of patch test, and thus a systematic convergence of the scheme is not guaranteed which is also confirmed from numerical simulations in section 2.5.

### 2.2.3 Element-based cluster rules

As opposed to introducing clusters at nodes of the triangulation, we consider clusters that are introduced in the interior of elements, preferably at the Gauss points, following quadrature rules in numerical approximation schemes. Figure 2.4 illustrates this scenario where one cluster is introduced inside each element. We define  $k_1(i) = \frac{Ny}{2} - i$ , and  $k_2(i) = \frac{N}{2} - i$ , which for  $i = -r_0 \dots r_0$  denote the positions of the atoms in the clusters located in the two elements. We assume without loss of generality that  $\frac{N}{2}$  and  $\frac{Ny}{2}$  are integers. Using the notation introduced in section 2.2.1, the approximate



energy is given by

$$\begin{aligned}
\tilde{E} &= n_1 \sum_{i=-r_0}^{r_0} \varepsilon(k_1(i)) + n_2 \sum_{i=-r_0}^{r_0} \varepsilon(-k_2(i)) \\
&= n_1(2r_0 + 1)\varepsilon_1 + n_2(2r_0 + 1)\varepsilon_2 + n_1 \sum_{i=-r_0}^{r_0} \Delta\varepsilon(k_1(i)) \\
&\quad + n_2 \sum_{i=-r_0}^{r_0} \Delta\varepsilon(-k_2(i)). \tag{2.33}
\end{aligned}$$

In the above expression,  $n_1$  and  $n_2$  are weights of the clusters located inside elements  $AC$  and  $BA$  respectively, and are computed such that piecewise constant functions are summed exactly—a zeroth order quadrature rule. Thus, we obtain  $n_1 = \frac{Ny}{2r_0+1}$  and  $n_2 = \frac{N}{2r_0+1}$ . In fact, since the clusters are centered at mid-points of the elements, which are the Gauss quadrature points, the cluster rule is first order accurate. Using a similar analysis as adopted in section 2.2.1, we note that  $\sum_{i=-r_0}^{r_0} \Delta\varepsilon(k_1(i)) = O(\frac{1}{(Ny)^{p-1}})$  and  $\sum_{i=-r_0}^{r_0} \Delta\varepsilon(-k_2(i)) = O(\frac{1}{(N)^{p-1}})$ , which are higher order terms. Thus,  $\tilde{E} = N\varepsilon_2 + Ny\varepsilon_1$ . Using equation (2.25), the approximation error in energy using an element-based cluster rule is estimated as

$$\tilde{E} - E = - \sum_{k=-r'}^{r'} \Delta\varepsilon(k). \tag{2.34}$$

Comparing equation (2.34) with equation (2.29), it is evident that the approximation error in element-based cluster rules is not dependent on the size of the element as opposed to node-based cluster rules, and thus is a much more controlled error. We now compute the error in forces, which are computed as tangents of the approximate energy. Element-based cluster rules too fail the patch test as will be demonstrated from the estimate below. Considering the case  $F_1 = F_2$  and following on similar lines as in section 2.2.2, the approximation error in the force on representative atom  $K = 0$

is estimated as

$$\begin{aligned}
\tilde{f}_0 &= \sum_{i=-r_0}^{r_0} \frac{1}{2r_0+1} \left( z(k_1(i)) - z(k_2(i)) + N \sum_{j=1}^{Ny} \bar{K}'(a_1|j+k_2(i)|) \right. \\
&\quad \left. - Ny \sum_{j=1}^N \bar{K}'(a_1|j+k_1(i)|) \right) \\
z(k_1(i)) &= \sum_{j=0}^{k_1(i)-1} \bar{K}'(a_1|j-k_1(i)|)j - \sum_{j=k_1(i)+1}^{Ny} \bar{K}'(a_1|j-k_1(i)|)j \\
&\quad + y \sum_{j=1}^N \bar{K}'(a_1|j+k_1(i)|)j. \\
z(k_2(i)) &= \sum_{j=0}^{k_2(i)-1} \bar{K}'(a_1|j-k_2(i)|)j - \sum_{j=k_2(i)+1}^N \bar{K}'(a_1|j-k_2(i)|)j \\
&\quad + \frac{1}{y} \sum_{j=1}^{Ny} \bar{K}'(a_1|j+k_2(i)|)j
\end{aligned} \tag{2.35}$$

We remark that  $\tilde{f}_0 \neq 0$  for  $y \neq 1$ , and  $\tilde{f}_0 = O(\frac{y-1}{N^{p-1}})$ . We refer to the appendix for further details on this estimate. Thus, for any general coarse-graining, the element-based cluster rules also fail the patch test. However, we note that this error is smaller than the error in node-based cluster rules (equation (2.32)) as it scales inversely with the element size for large elements and hence reduces to the Cauchy Born rule in the leading order.

The primary cause for the failure of patch test, which is a necessary condition for the convergence of numerical approximations, is that cluster rules which are introduced in the spirit of numerical quadratures are not compatible with non-local representations of energies. This aspect has also been highlighted in section 2.1. The notion of numerical quadratures has been developed for local functions, and its use on non-local representations of energies appears incompatible—at least in the sense of satisfying the patch test. We rectify this problem by first reformulating the extended

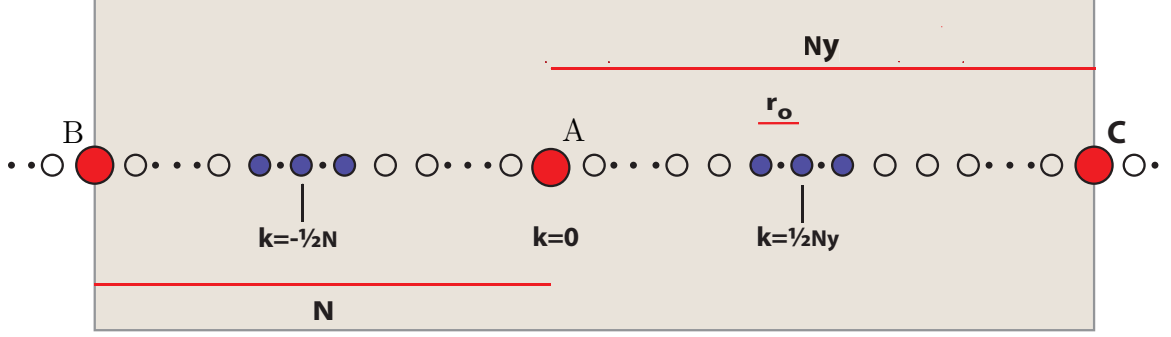


Figure 2.4: Schematic demonstrating element-based cluster rules: circles in red denote representative atoms while circles in blue denote atoms lying within clusters; clusters are located at the center of elements.

interactions in interatomic potentials into a local form, and subsequently introduce the quasi-continuum reduction.

### 2.3 Local reformulation of interatomic potentials

The energy of a single-component material system described by interatomic potentials, using the notation introduced in section 2.1, is given by

$$E(\mathbf{q}) = \sum_{\mathbf{i} \in \mathcal{L}} \varepsilon_{\mathbf{i}}(\mathbf{q}), \quad (2.36)$$

$$\varepsilon_{\mathbf{i}}(\mathbf{q}) = \sum_{\mathbf{j} \in \mathcal{L}, \mathbf{j} \neq \mathbf{i}} \bar{\mathbf{K}}|\mathbf{x}_{\mathbf{i}} - \mathbf{x}_{\mathbf{j}}|, \quad (2.37)$$

where  $\varepsilon_{\mathbf{i}}(\mathbf{q})$  denotes the energy of atom  $\mathbf{i}$  in the environment of its neighbors, and  $\bar{\mathbf{K}}$  denotes the kernel representing extended interatomic interactions. The widely used interatomic potentials include Lennard Jones potential, Morse potential, and embedded atom method (EAM) potentials (cf. e. g., *Lennard-Jones* (1925); *Morse* (1929); *Daw and Baskes* (1984); *Johnson* (1988); *Sutton and Chen* (1990)). The kernels used in these interatomic potentials are mostly either the *exponential kernel* ( $e^{-\alpha|\mathbf{x}_{\mathbf{i}} - \mathbf{x}_{\mathbf{j}}|}$ ), or kernels of the form  $\frac{1}{|\mathbf{x}_{\mathbf{i}} - \mathbf{x}_{\mathbf{j}}|^m}$ , where  $m$  is a positive integer, which we refer to in this article by *Lennard-Jones kernels*. We present the local reformulations

of these kernels, which convert the extended interactions often represented in a non-local form into a local variational problem. We first consider the case of exponential kernels, and then discuss our approach for Lennard-Jones kernels.

### 2.3.1 Exponential kernels

We consider the Morse potential which uses an exponential kernel to demonstrate our ideas. The energy of a single component material system in this case has the following form

$$\begin{aligned}
E^M(\mathbf{q}) &= \sum_{\mathbf{i} \in \mathcal{L}} \varepsilon_{\mathbf{i}}^M(\mathbf{q}), \\
\varepsilon_{\mathbf{i}}^M(\mathbf{q}) &= \frac{V_e}{2} \sum_{\mathbf{j} \in \mathcal{L}, \mathbf{j} \neq \mathbf{i}} \left\{ (1 - e^{-\alpha(|\mathbf{x}_{\mathbf{i}} - \mathbf{x}_{\mathbf{j}}| - x_e)})^2 - 1 \right\} \\
&= \frac{V_e}{2} \sum_{\mathbf{j} \in \mathcal{L}, \mathbf{j} \neq \mathbf{i}} \left\{ -2C e^{-\alpha|\mathbf{x}_{\mathbf{i}} - \mathbf{x}_{\mathbf{j}}|} + C^2 e^{-2\alpha|\mathbf{x}_{\mathbf{i}} - \mathbf{x}_{\mathbf{j}}|} \right\} \quad C = e^{\alpha x_e}, \quad (2.38)
\end{aligned}$$

where  $\alpha$ ,  $x_e$  and  $V_e$  are material constants. In order to construct a local reformulation of this non-local representation, we represent the atoms by regularized dirac distributions denoted by  $\delta(\mathbf{y} - \mathbf{x}_{\mathbf{i}})$  for  $\mathbf{i} \in \mathcal{L}$ . Further, we define  $b(\mathbf{y}; \mathbf{q}) = \sum_{\mathbf{i} \in \mathcal{L}} \delta(\mathbf{y} - \mathbf{x}_{\mathbf{i}})$ . The energy of the system can now be represented as

$$\begin{aligned}
E^M(\mathbf{q}) &= - V_e C \int_{\Omega_0} \int_{\Omega_0} b(\mathbf{y}; \mathbf{q}) e^{-\alpha|\mathbf{y} - \mathbf{y}'|} b(\mathbf{y}'; \mathbf{q}) d\mathbf{y} d\mathbf{y}' \\
&\quad + \frac{V_e C^2}{2} \int_{\Omega_0} \int_{\Omega_0} b(\mathbf{y}; \mathbf{q}) e^{-2\alpha|\mathbf{y} - \mathbf{y}'|} b(\mathbf{y}'; \mathbf{q}) d\mathbf{y} d\mathbf{y}'. \quad (2.39)
\end{aligned}$$

In the above expression  $\Omega_0 \subset \mathbb{R}^3$  is a simply connected bounded open set that contains the compact support of  $b$  (the region where  $b$  is non-zero). We note that the right-hand sides of equation (2.38) and equation (2.39) differ by the self-energy of the atoms which is an inconsequential constant that does not change the ground-state solution. We define  $\phi_1(\mathbf{y}; \mathbf{q}) = \int e^{-\alpha|\mathbf{y} - \mathbf{y}'|} b(\mathbf{y}'; \mathbf{q}) d\mathbf{y}'$  and take the Fourier transform

of this equation to get

$$\frac{(\alpha^2 + |\mathbf{k}|^2)^2}{8\pi\alpha} \hat{\phi}_1(\mathbf{k}) = \hat{b}(\mathbf{k}) \quad (2.40)$$

where  $\frac{8\pi\alpha}{(\alpha^2 + |\mathbf{k}|^2)^2}$  is the Fourier transform of  $e^{-\alpha|\mathbf{y}|}$ . Taking the inverse Fourier transform of equation (2.40) we arrive at

$$\frac{1}{8\pi\alpha} \{\nabla^4 - 2\alpha^2 \nabla^2 + \alpha^4\} \phi_1(\mathbf{y}; \mathbf{q}) = b(\mathbf{y}; \mathbf{q}). \quad (2.41)$$

In effect we have constructed the partial differential equation whose Green's function is the exponential kernel, which is the bi-harmonic equation. Rewriting equation (2.41) in a variational form we arrive at

$$\begin{aligned} I_1(\mathbf{q}) = & \inf_{\varphi_1 \in H_0^2(\Omega)} \frac{1}{8\pi\alpha} \left\{ \frac{1}{2} \int_{\Omega} (\nabla^2 \varphi_1)^2 d\mathbf{y} + \alpha^2 \int_{\Omega} |\nabla \varphi_1|^2 d\mathbf{y} \right. \\ & \left. + \frac{\alpha^4}{2} \int_{\Omega} \varphi_1^2 d\mathbf{y} - 8\pi\alpha \int_{\Omega} b(\mathbf{q}) \varphi_1 d\mathbf{y} \right\}, \end{aligned} \quad (2.42)$$

where  $\Omega \subset \mathbb{R}^3$  denotes the compact support of  $\varphi_1$  and other potentials we subsequently compute. We remark that the variation problem in equation (2.42) is well-posed and a minimizer exists which is unique. The solution of the partial differential in equation (2.41) is now given by  $\phi_1 = \arg \min I_1$ .

The variational problem in equation (2.42) requires the trial functions to be in  $H_0^2(\Omega)$ , and commonly used numerical schemes like  $C^0$  finite-elements are not dense in this function space. To this end, we consider the equivalent mixed variational

formulation given by

$$I_1(\mathbf{q}) = \inf_{\varphi_1 \in H_0^1(\Omega)} \sup_{\varrho_1 \in H_0^1(\Omega)} \frac{1}{8\pi\alpha} \left\{ \alpha^2 \int_{\Omega} |\nabla \varphi_1|^2 d\mathbf{y} + \frac{\alpha^4}{2} \int_{\Omega} \varphi_1^2 d\mathbf{y} - 8\pi\alpha \int_{\Omega} b(\mathbf{q}) \varphi_1 d\mathbf{y} - \int_{\Omega} \nabla \varphi_1 \cdot \nabla \varrho_1 d\mathbf{y} - \frac{1}{2} \int_{\Omega} \varrho_1^2 d\mathbf{y} \right\}. \quad (2.43)$$

The corresponding Euler-Lagrange equations are

$$\nabla^2 \rho_1(\mathbf{y}; \mathbf{q}) - 2\alpha^2 \nabla^2 \phi_1(\mathbf{y}; \mathbf{q}) + \alpha^4 \phi_1(\mathbf{y}; \mathbf{q}) - 8\pi\alpha b(\mathbf{y}; \mathbf{q}) = 0 \quad (2.44a)$$

$$\nabla^2 \phi_1(\mathbf{y}; \mathbf{q}) - \rho_1(\mathbf{y}; \mathbf{q}) = 0 \quad (2.44b)$$

which is a system of equations representing the bi-harmonic equation in equation (2.41). In the above equation  $\phi_1$  and  $\rho_1$  denote the minimizer and maximizer of the mixed variational formulation in equation (2.43) respectively.

Following along similar lines we define  $\phi_2(\mathbf{y}; \mathbf{q}) = \int e^{-2\alpha|\mathbf{y}-\mathbf{y}'|} b(\mathbf{y}'; \mathbf{q}) d\mathbf{y}'$ , and the corresponding mixed variational problem for  $\phi_2$  is given by

$$I_2(\mathbf{q}) = \inf_{\varphi_2 \in H_0^1(\Omega)} \sup_{\varrho_2 \in H_0^1(\Omega)} \frac{1}{16\pi\alpha} \left\{ 4\alpha^2 \int_{\Omega} |\nabla \varphi_2|^2 d\mathbf{y} + 8\alpha^4 \int_{\Omega} \varphi_2^2 d\mathbf{y} - 16\pi\alpha \int_{\Omega} b(\mathbf{q}) \varphi_2 d\mathbf{y} - \int_{\Omega} \nabla \varphi_2 \cdot \nabla \varrho_2 d\mathbf{y} - \frac{1}{2} \int_{\Omega} \varrho_2^2 d\mathbf{y} \right\}, \quad (2.45)$$

where  $\phi_2$  is the minimizer of the above mixed variational problem. Using the Euler-Lagrange equations corresponding to the mixed variational problems in equations (2.43) and (2.45), we note that

$$I_1(\mathbf{q}) = -\frac{1}{2} \int_{\Omega} b(\mathbf{y}; \mathbf{q}) \phi_1(\mathbf{y}; \mathbf{q}) d\mathbf{y}, \quad I_2(\mathbf{q}) = -\frac{1}{2} \int_{\Omega} b(\mathbf{y}; \mathbf{q}) \phi_2(\mathbf{y}; \mathbf{q}) d\mathbf{y}. \quad (2.46)$$

Using equations (2.39) and (2.46), we can rewrite the energy of the system as

$$E^M(\mathbf{q}) = 2CV_e I_1(\mathbf{q}) - C^2 V_e I_2(\mathbf{q}). \quad (2.47)$$

Using equations (2.42)-(2.47) we arrive at the saddle-point problem that describes the energy of the system:

$$E^M(\mathbf{q}) = \inf_{\substack{\varphi_1 \in H_0^1(\Omega) \\ \varrho_2 \in H_0^1(\Omega)}} \sup_{\substack{\varphi_2 \in H_0^1(\Omega) \\ \varrho_1 \in H_0^1(\Omega)}} \int_{\Omega} L(\varphi_1, \varrho_1, \varphi_2, \varrho_2; \mathbf{q}) d\mathbf{y}.$$

$$L(\varphi_1, \varrho_1, \varphi_2, \varrho_2; \mathbf{q}) = \frac{2CV_e}{8\pi\alpha} \left\{ \alpha^2 |\nabla \varphi_1|^2 + \frac{\alpha^4}{2} \varphi_1^2 - 8\pi\alpha b(\mathbf{q})\varphi_1 - \nabla \varphi_1 \cdot \nabla \varrho_1 - \frac{1}{2} \varrho_1^2 \right\}$$

$$- \frac{C^2 V_e}{16\pi\alpha} \left\{ 4\alpha^2 |\nabla \varphi_2|^2 + 8\alpha^4 \varphi_2^2 - 16\pi\alpha b(\mathbf{q})\varphi_2 - \nabla \varphi_2 \cdot \nabla \varrho_2 - \frac{1}{2} \varrho_2^2 \right\} \quad (2.48)$$

The saddle-point problem in equation (2.48) is a local reformulation of the extended interactions with exponential kernels. The problem of computing ground-state properties of a system is then given by the variation problem

$$E_0^M = \inf_{\mathbf{q} \in X} E^M(\mathbf{q}), \quad (2.49)$$

or equivalently the saddle-point problem on the Lagrangian  $L(\varphi_1, \varrho_1, \varphi_2, \varrho_2; \mathbf{q})$

$$E_0^M = \inf_{\mathbf{q} \in X} \inf_{\substack{\varphi_1 \in H_0^1(\Omega) \\ \varrho_2 \in H_0^1(\Omega)}} \sup_{\substack{\varphi_2 \in H_0^1(\Omega) \\ \varrho_1 \in H_0^1(\Omega)}} \int_{\Omega} L(\varphi_1, \varrho_1, \varphi_2, \varrho_2; \mathbf{q}) d\mathbf{y}. \quad (2.50)$$

The saddle-point problem in the above equation describes a crystallite in  $\mathbb{R}^3$  with finite number of atoms. Though we restrict our discussion of the formulation for a finite crystallite, the formulation itself and other remarks we made and will make subsequently are in general true for other systems like a periodic system, semi-infinite lattice, etc. For instance, the properties of a periodic system are obtained by appro-

privately changing the function space in the formulation to  $H_{per}^1(Q)$  where  $Q$  denotes the supercell, or  $H^1(Q)$  if the supercell is chosen such that  $\partial Q$  contains only planes of symmetry of the lattice.

We now consider the computation of forces on atoms. Consider the infinitesimal perturbation of atom positions given by a family of mappings  $\psi_\epsilon : \mathbb{R}^{3M} \rightarrow \mathbb{R}^{3M}$  with  $\epsilon \ll 1$  as the parameter. We denote by  $\psi_\epsilon^{\mathbf{i}} : \mathbb{R}^3 \rightarrow \mathbb{R}^3$  the infinitesimal perturbation of atom  $\mathbf{i}$  such that  $\psi_0^{\mathbf{i}} = id$  (identity mapping) and  $\frac{d}{d\epsilon}(\psi_\epsilon^{\mathbf{i}})_j|_{\epsilon=0} = \Gamma_j^{\mathbf{i}}$  for  $\mathbf{i} \in \mathcal{L}$ ,  $j = 1, 2, 3$ .  $\Gamma_j^{\mathbf{i}}$  is often referred to as the generator of the infinitesimal mappings, and the directional derivative corresponding to this generator is given by

$$\begin{aligned}
& \frac{d}{d\epsilon} E^M(\psi_\epsilon(\mathbf{q})) \Big|_{\epsilon=0} = \frac{d}{d\epsilon} \left( -2CV_e \int_{\Omega} b(\psi_\epsilon(\mathbf{q})) \phi_1 d\mathbf{y} + C^2 V_e \int_{\Omega} b(\psi_\epsilon(\mathbf{q})) \phi_2 d\mathbf{y} \right) \Big|_{\epsilon=0} \\
&= 2CV_e \sum_{\mathbf{k} \in \mathcal{L}} \int_{\Omega} \frac{\partial \delta(\mathbf{y} - \psi_\epsilon^{\mathbf{k}}(\mathbf{x}_{\mathbf{k}}))}{\partial y_j} \frac{d(\psi_\epsilon^{\mathbf{k}})_j}{d\epsilon} \phi_1(\mathbf{y}) d\mathbf{y} \Big|_{\epsilon=0} \\
&\quad - C^2 V_e \sum_{\mathbf{k} \in \mathcal{L}} \int_{\Omega} \frac{\partial \delta(\mathbf{y} - \psi_\epsilon^{\mathbf{k}}(\mathbf{x}_{\mathbf{k}}))}{\partial y_j} \frac{d(\psi_\epsilon^{\mathbf{k}})_j}{d\epsilon} \phi_2(\mathbf{y}) d\mathbf{y} \Big|_{\epsilon=0} \quad (\nabla_{\mathbf{r}} \delta(\mathbf{r} - \mathbf{r}') = -\nabla_{\mathbf{r}'} \delta(\mathbf{r} - \mathbf{r}')) \\
&= -2CV_e \sum_{\mathbf{k} \in \mathcal{L}} \int_{\Omega} \delta(\mathbf{y} - \mathbf{x}_{\mathbf{k}}) \Gamma_j^{\mathbf{k}} \frac{\partial \phi_1(\mathbf{y})}{\partial y_j} d\mathbf{x} + C^2 V_e \sum_{\mathbf{k} \in \mathcal{L}} \int_{\Omega} \delta(\mathbf{y} - \mathbf{x}_{\mathbf{k}}) \Gamma_j^{\mathbf{k}} \frac{\partial \phi_2(\mathbf{y})}{\partial y_j} d\mathbf{y} \\
&= - \sum_{\mathbf{k} \in \mathcal{L}} \left( 2CV_e \frac{\partial \phi_1}{\partial y_j}(\mathbf{x}_{\mathbf{k}}) - C^2 V_e \frac{\partial \phi_2}{\partial y_j}(\mathbf{x}_{\mathbf{k}}) \right) \Gamma_j^{\mathbf{k}}
\end{aligned} \tag{2.51}$$

The force on an atom  $\mathbf{k} \in \mathcal{L}$  is given by  $\mathbf{f}_{\mathbf{k}}(\mathbf{q}) = -\frac{\partial E^M(\mathbf{q})}{\partial \mathbf{x}_{\mathbf{k}}}$ , and using equation (2.51) we obtain

$$\mathbf{f}_{\mathbf{k}} = 2CV_e \nabla \phi_1(\mathbf{x}_{\mathbf{k}}) - C^2 V_e \nabla \phi_2(\mathbf{x}_{\mathbf{k}}). \tag{2.52}$$

We note that the expression for force on any atom given by equation (2.52) is *local*.

In arriving at equation (2.51) we computed the directional derivative by perturbing the positions of atoms. An equivalent approach, instead, is to hold the positions of atoms fixed and perturb the underlying space, which corresponds to taking inner variations of the energy functional in equation (2.48). Let  $\psi_\epsilon : \Omega \rightarrow \Omega'$  be infinitesimal



deformations corresponding to the generator  $\Gamma(\mathbf{y})$ , given by  $\Gamma = \frac{d\psi_\epsilon}{d\epsilon}\big|_{\epsilon=0}$ , such that  $\psi_0 = id$ . We constrain the generator such that  $div\Gamma = 0$  in the compact support of  $b$  in order to satisfy the integral condition  $\int_\Omega \delta(\mathbf{y} - \mathbf{x}_i) d\mathbf{y} = 1$ ,  $\mathbf{i} \in \mathcal{L}$ . Let  $\mathbf{y}$  denote a point in  $\Omega$  whose image in  $\Omega'$  is  $\mathbf{y}' = \psi_\epsilon(\mathbf{y})$ . We first consider the energy functional  $I_1$ , which under infinitesimal variations is given by

$$\begin{aligned}
I_1(\psi_\epsilon) = & \frac{1}{8\pi\alpha} \left\{ \alpha^2 \int_{\Omega'} |\nabla_{\mathbf{y}'} \phi_1(\mathbf{y}')|^2 d\mathbf{y}' + \frac{\alpha^4}{2} \int_{\Omega'} \phi_1^2(\mathbf{y}') d\mathbf{y}' \right. \\
& \left. - 8\pi\alpha \int_{\Omega'} b(\psi_\epsilon^{-1}(\mathbf{y}'); \mathbf{q}) \phi_1(\mathbf{y}') d\mathbf{y}' - \int_{\Omega'} \nabla_{\mathbf{y}'} \phi_1(\mathbf{y}') \cdot \nabla_{\mathbf{y}'} \rho_1(\mathbf{y}') d\mathbf{y}' - \int_{\Omega'} \frac{1}{2} \rho_1^2(\mathbf{y}') d\mathbf{y}' \right\}
\end{aligned} \tag{2.53}$$

Transforming the integrals back onto  $\Omega$ , we obtain

$$\begin{aligned}
I_1(\psi_\epsilon) = & \frac{1}{8\pi\alpha} \left\{ \alpha^2 \int_{\Omega} \frac{\partial y_j}{\partial y'_i} \frac{\partial \phi_1(\psi_\epsilon(\mathbf{y}))}{\partial y_j} \frac{\partial \phi_1(\psi_\epsilon(\mathbf{y}))}{\partial y_k} \frac{\partial y_k}{\partial y'_i} \det\left(\frac{\partial y'_l}{\partial y_m}\right) d\mathbf{y} \right. \\
& + \frac{\alpha^4}{2} \int_{\Omega} \phi_1^2(\psi_\epsilon(\mathbf{y})) \det\left(\frac{\partial y'_l}{\partial y_m}\right) d\mathbf{y} - 8\pi\alpha \int_{\Omega} b(\mathbf{y}; \mathbf{q}) \phi_1(\psi_\epsilon(\mathbf{y})) \det\left(\frac{\partial y'_l}{\partial y_m}\right) d\mathbf{y} \\
& - \int_{\Omega} \frac{\partial y_j}{\partial y'_i} \frac{\partial \phi_1(\psi_\epsilon(\mathbf{y}))}{\partial y_j} \frac{\partial \rho_1(\psi_\epsilon(\mathbf{y}))}{\partial y_k} \frac{\partial y_k}{\partial y'_i} \det\left(\frac{\partial y'_l}{\partial y_m}\right) d\mathbf{y} \\
& \left. - \frac{1}{2} \int_{\Omega} \rho_1^2(\psi_\epsilon(\mathbf{y})) \det\left(\frac{\partial y'_l}{\partial y_m}\right) d\mathbf{y} \right\}
\end{aligned} \tag{2.54}$$

We note that in taking the variation of  $I_1(\psi_\epsilon)$ , the terms arising from variations of  $\phi_1(\psi_\epsilon)$  and  $\rho_1(\psi_\epsilon)$  vanish as  $\phi_1$  and  $\rho_1$  satisfies the Euler-Lagrange equations of  $I_1$ . The non-trivial contributions to variation of  $I_1$  come from variations of  $\det\left(\frac{\partial y'_l}{\partial y_m}\right)$  and

$\frac{\partial y_k}{\partial y'_i}$ . We first note the following identities which will be used subsequently:

$$\begin{aligned} \frac{d}{d\epsilon} \left\{ \frac{\partial y_i}{\partial y'_j} \right\} \Big|_{\epsilon=0} &= - \frac{\partial y_i}{\partial y'_k} \left( \frac{d}{d\epsilon} \left\{ \frac{\partial \psi_{\epsilon k}}{\partial y_l} \right\} \right) \frac{\partial y_l}{\partial y'_j} \Big|_{\epsilon=0} \\ &= - \frac{\partial \Gamma_i}{\partial y_j} \quad \left( \text{Note: } \frac{\partial y_i}{\partial y'_j} \Big|_{\epsilon=0} = \delta_{ij} \right) \end{aligned} \quad (2.55)$$

$$\begin{aligned} \frac{d}{d\epsilon} \left\{ \det \left( \frac{\partial y'_l}{\partial y_m} \right) \right\} \Big|_{\epsilon=0} &= \det \left( \frac{\partial y'_l}{\partial y_m} \right) \frac{\partial y_j}{\partial y'_i} \left( \frac{d}{d\epsilon} \left\{ \frac{\partial \psi_{\epsilon i}}{\partial y_j} \right\} \right) \Big|_{\epsilon=0} \\ &= \frac{\partial \Gamma_j}{\partial y_j}. \end{aligned} \quad (2.56)$$

Using the above identities, the Gâteaux derivative of the energy functional  $I_1$  is given by

$$\begin{aligned} \frac{dI_1(\psi_\epsilon)}{d\epsilon} \Big|_{\epsilon=0} &= \int_{\Omega} W_1 \frac{\partial \Gamma_i}{\partial y_i} d\mathbf{y} - \frac{\alpha}{4\pi} \int_{\Omega} \frac{\partial \phi_1}{\partial y_i} \frac{\partial \phi_1}{\partial y_j} \frac{\partial \Gamma_i}{\partial y_j} d\mathbf{y} \\ &\quad + \frac{1}{8\pi\alpha} \int_{\Omega} \left( \frac{\partial \phi_1}{\partial y_i} \frac{\partial \rho_1}{\partial y_j} + \frac{\partial \rho_1}{\partial y_i} \frac{\partial \phi_1}{\partial y_j} \right) \frac{\partial \Gamma_i}{\partial y_j} d\mathbf{y} \quad \text{where} \quad (2.57) \\ W_1 &= \frac{1}{8\pi\alpha} \left\{ \alpha^2 |\nabla \phi_1|^2 + \frac{\alpha^4}{2} \phi_1^2 - 8\pi\alpha b(\mathbf{q})\phi_1 - \nabla \varphi_1 \cdot \nabla \rho_1 - \frac{1}{2} \rho_1^2 \right\}. \end{aligned}$$

On similar lines we compute the Gâteaux derivative of the energy functional  $I_2$  to be

$$\begin{aligned} \frac{dI_2(\psi_\epsilon)}{d\epsilon} \Big|_{\epsilon=0} &= \int_{\Omega} W_2 \frac{\partial \Gamma_i}{\partial y_i} d\mathbf{y} - \frac{\alpha}{2\pi} \int_{\Omega} \frac{\partial \phi_2}{\partial y_i} \frac{\partial \phi_2}{\partial y_j} \frac{\partial \Gamma_i}{\partial y_j} d\mathbf{y} \\ &\quad + \frac{1}{16\pi\alpha} \int_{\Omega} \left( \frac{\partial \phi_2}{\partial y_i} \frac{\partial \rho_2}{\partial y_j} + \frac{\partial \rho_2}{\partial y_i} \frac{\partial \phi_2}{\partial y_j} \right) \frac{\partial \Gamma_i}{\partial y_j} d\mathbf{y} \quad \text{where} \quad (2.58) \\ W_2 &= \frac{1}{16\pi\alpha} \left\{ 4\alpha^2 |\nabla \phi_2|^2 + 8\alpha^4 \phi_2^2 - 16\pi\alpha b(\mathbf{q})\phi_2 - \nabla \varphi_2 \cdot \nabla \rho_2 - \frac{1}{2} \rho_2^2 \right\}. \end{aligned}$$

From equations (2.57) and (2.58), the generalized force corresponding to  $E^M$  is given

by

$$\begin{aligned} \left. \frac{dE(\psi_\epsilon)}{d\epsilon} \right|_{\epsilon=0} &= \int_{\Omega} \mathbf{E}_{ij} \frac{\partial \Gamma_i}{\partial y_j} d\mathbf{y} \quad \text{where} \\ \mathbf{E}_{ij} &= L(\phi_1, \rho_1, \phi_2, \rho_2) \delta_{ij} - \frac{\alpha}{2\pi} \left( CV_e \frac{\partial \phi_1}{\partial y_i} \frac{\partial \phi_1}{\partial y_j} - C^2 V_e \frac{\partial \phi_2}{\partial y_i} \frac{\partial \phi_2}{\partial y_j} \right) \\ &\quad + \frac{1}{16\pi\alpha} \left\{ 4CV_e \left( \frac{\partial \phi_1}{\partial y_i} \frac{\partial \rho_1}{\partial y_j} + \frac{\partial \rho_1}{\partial y_i} \frac{\partial \phi_1}{\partial y_j} \right) - C^2 V_e \left( \frac{\partial \phi_2}{\partial y_i} \frac{\partial \rho_2}{\partial y_j} + \frac{\partial \rho_2}{\partial y_i} \frac{\partial \phi_2}{\partial y_j} \right) \right\} \end{aligned} \quad (2.59)$$

The above expression for generalized forces corresponding to the outer minimization problem in equation (2.50), which is *local*, is the Eshelby representation of configurational forces. In this thesis we refer to this form as the Eshelby form of the generalized forces. We note that equations (2.51) and (2.59) are equivalent when  $\psi_\epsilon : \Omega \rightarrow \Omega$ , which can be verified by integrating by parts the expression in equation (2.59), and using the Euler-Lagrange equations for (2.59) along with the constraint  $\text{div } \Gamma = 0$  in the compact support of  $b$ . However, when  $\psi_\epsilon : \Omega \rightarrow \Omega'$ , then the Eshelby form alone gives the correct generalized force which also accounts for the change in the domain. In the quasi-continuum reduction to follow in section 2.4 the elastic effects in coarse-grained regions of the triangulation arise from the change in the shape and size of unit cells representing the Cauchy-Born deformation. These elastic effects are naturally captured by the Eshelby form, and therein lies its need and usefulness.

### 2.3.2 Lennard-Jones kernels

We now proceed to the local reformulation of kernels of the form  $\frac{1}{|\mathbf{x}_i - \mathbf{x}_j|^m}$  where  $m$  is a positive integer. Lennard-Jones interatomic potential (*Lennard-Jones*, 1925) is an example of a widely used potential that uses kernels of this form, alongside some EAM potentials (cf. e. g. *Sutton and Chen* (1990)). We seek to construct the partial differential equation whose Green's function is the kernel  $\frac{1}{|\mathbf{y} - \mathbf{y}'|^m}$ . We note that the Green's function of Laplace operator in three-dimensions is  $\frac{1}{|\mathbf{y} - \mathbf{y}'|}$ . But

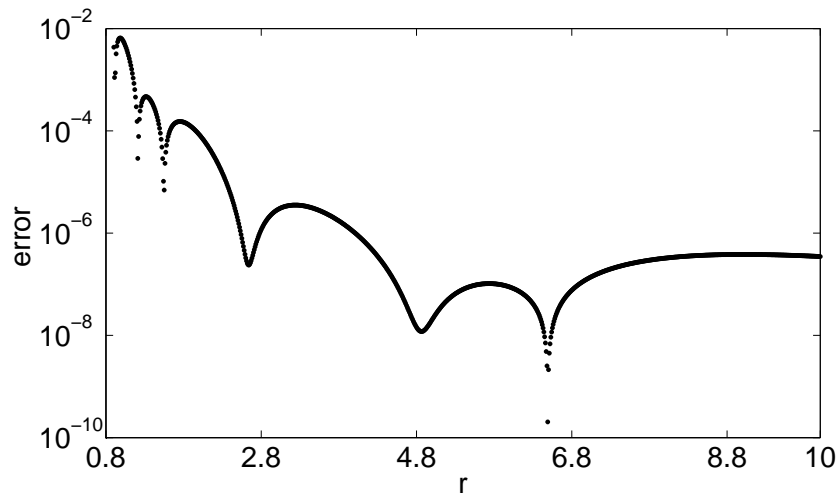
Table 2.1: Table of coefficients for an approximate fitting of  $\frac{1}{r^6}$  and  $\frac{1}{r^{12}}$  kernels with a kernel of the form  $ae^{-\alpha r} + b\frac{e^{-(\beta r)}}{r} + c\frac{e^{-(\gamma r)}}{r} + d\frac{e^{-(\lambda r)}}{r}$ .

coefficients of fit for kernel $\frac{1}{r^6}$				coefficients of fit for kernel $\frac{1}{r^{12}}$			
a	0.002484	$\alpha$	3.4262	a	$1.349 * 10^7$	$\alpha$	18.1135
b	14.11	$\beta$	0.02465	b	225.2	$\beta$	7.2092
c	547.5	$\gamma$	7.0597	c	$2.6 * 10^4$	$\gamma$	10.608
d	0.3833	$\lambda$	1.6154	d	0.4877	$\lambda$	3.8377

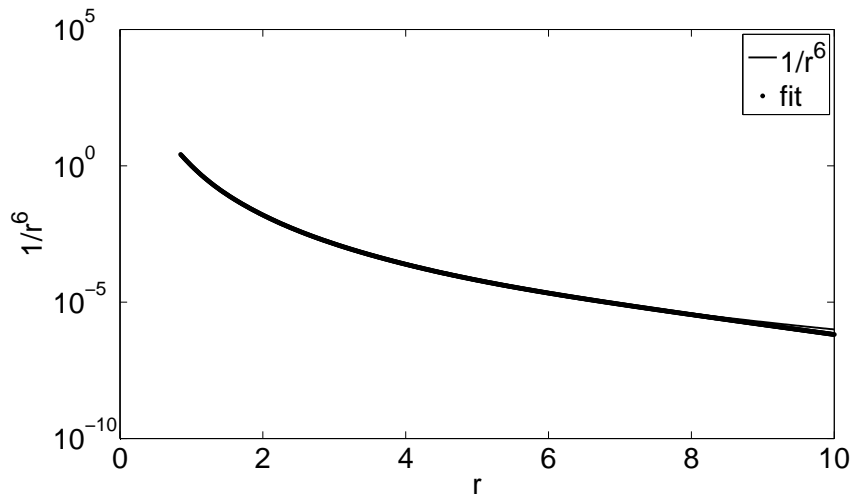
constructing a linear differential operator whose Green’s function is  $\frac{1}{|\mathbf{y}-\mathbf{y}'|^m}$  for any generic  $m$  is beyond reach, at least to the best of our knowledge. Thus we seek to find a good approximation for these kernels which can in turn be reformulated in a local form. We require this approximation to be accurate in the domain of influence of the potential—typically in the range  $0.85a < |\mathbf{y} - \mathbf{y}'| < Ca$ ,  $C \in \mathbb{Z}$ , where  $a$  is the nearest neighbor interatomic spacing of an undeformed lattice. The lower limit of this range guarantees that the energetics are accurate even up to 15% compressive strains and the value of the upper-limit  $C$  is chosen based on the decay of the potential. We consider an approximation of the form

$$\frac{1}{|\mathbf{y} - \mathbf{y}'|^m} \approx \sum_{j=1}^{M_0} A_j \frac{e^{-\alpha_j |\mathbf{y}-\mathbf{y}'|}}{4\pi |\mathbf{y} - \mathbf{y}'|} + \sum_{k=1}^{M_1} B_k e^{-\beta_k |\mathbf{y}-\mathbf{y}'|} \quad (2.60)$$

where  $A_j, \alpha_j$  for  $j = 1 \dots M_0$  and  $B_k, \beta_k$  for  $k = 1 \dots M_1$  are constants that are fit to best approximate the kernel. To test the accuracy of this approximation we consider two test cases with  $m = 6$  and  $m = 12$  that correspond to the Lennard-Jones interatomic potential. Figures 2.5, 2.6 demonstrate the accuracy of this approximation, where by just using four terms in the power series we obtain a good approximation to the desired kernels. Table 2.1 provides the coefficients corresponding to these approximations, where the relative  $\ell_2$  error of these approximations is less than 0.01 in both cases.

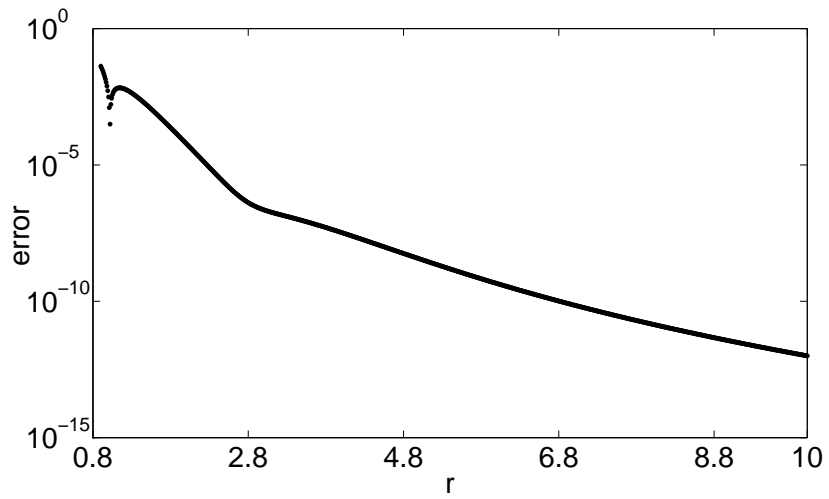


(a) linear scale

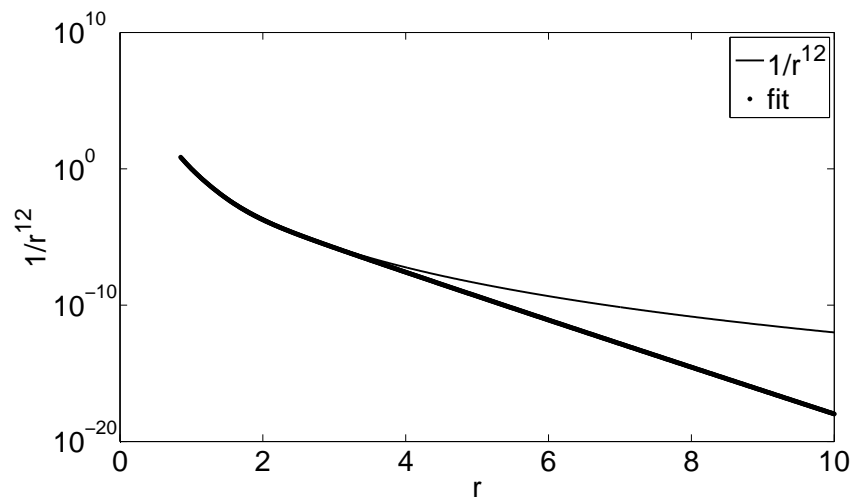


(b) semi-log scale

Figure 2.5: A fit for kernel  $\frac{1}{r^6}$  with an approximate kernel of the form  $ae^{-\alpha r} + b\frac{e^{-(\beta r)}}{r} + c\frac{e^{-(\gamma r)}}{r} + d\frac{e^{-(\lambda r)}}{r}$ .



(a) linear scale



(b) semi-log scale

Figure 2.6: A fit for kernel  $\frac{1}{r^{12}}$  with an approximate kernel of the form  $ae^{-\alpha r} + b\frac{e^{-(\beta r)}}{r} + c\frac{e^{-(\gamma r)}}{r} + d\frac{e^{-(\lambda r)}}{r}$ .

Following the ideas developed in section 2.3.1, we replace the atoms by regularized dirac distributions and the interatomic interaction energy corresponding to a  $\frac{1}{|\mathbf{x}_i - \mathbf{x}_j|^m}$  kernel is then given by

$$\begin{aligned}
E(\mathbf{q}) &= \int_{\Omega} \int_{\Omega} b(\mathbf{y}; \mathbf{q}) \frac{1}{|\mathbf{y} - \mathbf{y}'|^m} b(\mathbf{y}'; \mathbf{q}) d\mathbf{y} d\mathbf{y}' \\
&\approx \sum_{j=1}^{M_0} A_j \int_{\Omega} \int_{\Omega} b(\mathbf{y}; \mathbf{q}) \frac{e^{-\alpha_j |\mathbf{y} - \mathbf{y}'|}}{4\pi |\mathbf{y} - \mathbf{y}'|} b(\mathbf{y}'; \mathbf{q}) d\mathbf{y} d\mathbf{y}' \\
&\quad + \sum_{k=1}^{M_1} B_k \int_{\Omega} \int_{\Omega} b(\mathbf{y}; \mathbf{q}) e^{-\beta_k |\mathbf{y} - \mathbf{y}'|} b(\mathbf{y}'; \mathbf{q}) d\mathbf{y} d\mathbf{y}'
\end{aligned} \tag{2.61}$$

To keep the expressions simple, we will represent the second series of exponential kernels in equation (2.61) by  $E^{exp}(\mathbf{q})$  whose local reformulation is already established in section 2.3.1. We denote by  $\phi_j(\mathbf{y}; \mathbf{q})$  the convolution  $\int \frac{e^{-\alpha_j |\mathbf{y} - \mathbf{y}'|}}{4\pi |\mathbf{y} - \mathbf{y}'|} b(\mathbf{y}'; \mathbf{q}) d\mathbf{y}'$ ,  $j = 1, \dots, M_0$ . Taking the Fourier transform of the above expression we obtain

$$(|\mathbf{k}|^2 + \alpha_j^2) \hat{\phi}_j(\mathbf{k}) = \hat{b}(\mathbf{k}) \quad j = 1, \dots, M_0. \tag{2.62}$$

Taking the inverse Fourier transform we obtain the Helmholtz equation

$$(-\nabla^2 + \alpha_j^2) \phi_j(\mathbf{y}; \mathbf{q}) = b(\mathbf{y}; \mathbf{q}) \quad j = 1, \dots, M_0. \tag{2.63}$$

The energy in equation (2.61) can now be reformulated into a local form using the

variational form of equation (2.63), and is given by

$$E(\mathbf{q}) = \sum_{j=1}^{M_0} 2A_j I_j(\mathbf{q}) + E^{exp}(\mathbf{q}) \quad \text{where}$$

$$I_j(\mathbf{q}) = - \inf_{\varphi_j \in H_0^1(\Omega)} \left\{ \frac{1}{2} \int_{\Omega} |\nabla \varphi_j|^2 d\mathbf{y} + \frac{\alpha_j^2}{2} \int_{\Omega} \varphi_j^2 d\mathbf{y} - \int_{\Omega} b(\mathbf{q}) \varphi_j d\mathbf{y} \right\} \quad j = 1, \dots, M_0. \quad (2.64)$$

Further  $\phi_j = \arg \min I_j$ . Following on similar lines as in section 2.3.1 the Eshelby form of the generalized force for infinitesimal deformations corresponding to the generator  $\Gamma$  is given by

$$\frac{dE(\psi_\epsilon)}{d\epsilon} \Big|_{\epsilon=0} = \sum_{j=1}^{M_0} 2A_j \frac{dI_j(\psi_\epsilon)}{d\epsilon} \Big|_{\epsilon=0} + \frac{dE^{exp}(\psi_\epsilon)}{d\epsilon} \Big|_{\epsilon=0} \quad \text{where,}$$

$$\frac{dI_j(\psi_\epsilon)}{d\epsilon} \Big|_{\epsilon=0} = - \int_{\Omega} \left\{ \frac{1}{2} |\nabla \phi_j|^2 + \frac{\alpha_j^2 \phi_j^2}{2} - b(\mathbf{q}) \phi_j \right\} \frac{\partial \Gamma_i}{\partial y_i} d\mathbf{y}$$

$$+ \int_{\Omega} \frac{\partial \phi_j}{\partial y_i} \frac{\partial \phi_j}{\partial y_k} \frac{\partial \Gamma_i}{\partial y_k} d\mathbf{y} \quad j = 1, \dots, M_0 \quad (2.65)$$

Hence the energy as well as force expressions are now expressed in a local form which are amenable to quasi-continuum reduction, and is discussed in the next section.

## 2.4 Quasi-continuum reduction

The energetics of a material system, following the local reformulation of extended interactions discussed in section 2.3, is described by various fields, namely, the displacement field of atomic positions and potential fields that appear in the variational formulation (cf. equation (2.50)). The nature of the displacement field is such that it varies rapidly vary the core of a defect but becomes smooth away from the core



where the response is elastic. Potential fields on the other hand exhibit oscillations on the length-scale of the lattice parameter. This follows from oscillations in the forcing term,  $b(\mathbf{q})$ , on the lattice length-scale. In regions away from the defect-core, where the displacement field is smoothly varying, the fine-scale oscillations in potential fields exhibit a well characterized structure. In these regions potential fields are determined to leading order by a periodic calculation using the Cauchy-Born deformation. This follows from a formal result in *Blanc et al.* (2002), where this property has been shown for a class of non-linear functionals. We exploit this structure in potential fields to achieve the quasi-continuum reduction of the local field formulation proposed in section 2.3. The key ideas behind this quasi-continuum reduction have first been proposed in the context of orbital-free density functional theory in *Gavini et al.* (2007a). Here, we revisit these ideas in the context of empirical interatomic potentials with the focus on demonstrating the method being a systematic numerical coarse-graining scheme devoid of the inconsistencies in previous QC formulations.

The quasi-continuum reduction of field formulation is realized by coarse-graining the various fields that appear in the formulation using three unstructured finite-element triangulations with *linear* shape-functions:

- (i) a triangulation  $T_{h_1}$  of selected representative atoms forming  $\mathcal{L}_h$  in the usual manner of QC, which is labeled as *atomic mesh*;
- (ii) a triangulation  $T_{h_3}$ , subatomic close to lattice defects and increasingly coarser away from the defects, which is labeled as *potential-mesh*.
- (iii) an uniformly subatomic triangulation  $T_{h_2}$  to capture the fine-scale oscillations in potential fields, which is labeled as *fine-mesh*. A schematic of the hierarchy of meshes in one dimension is shown in figure 2.7. For convenience, these triangulations are restricted in such a way that  $T_{h_3}$  is a sub-grid of  $T_{h_1}$  and  $T_{h_2}$  is a sub-grid of  $T_{h_3}$ . The corresponding finite-element approximation spaces are denoted by  $X^{h_1}$ ,  $X^{h_2}$  and  $X^{h_3}$ . To demonstrate the main ideas behind quasi-continuum reduction, we consider

the energy of a system described by exponential kernels. We recall from section 2.3.1 that the local reformulation of such an energy is given by

$$E_0^M = \inf_{\mathbf{q} \in X} \inf_{\substack{\varphi_1 \in Y \\ \varrho_2 \in Y}} \sup_{\substack{\varphi_2 \in Y \\ \varrho_1 \in Y}} \int_{\Omega} L(\varphi_1, \varrho_1, \varphi_2, \varrho_2; \mathbf{q}) d\mathbf{y}. \quad (2.66)$$

where  $L$  denotes the Lagrangian given in equation (2.48). In the above expression  $Y$  denotes a suitable function space which is  $H_0^1(\Omega)$  for non-periodic problems on domain  $\Omega$ , or  $H_{per}^1(Q)$  for periodic problems on a supercell  $Q$ . We decompose the potentials as

$$\begin{aligned} \varphi_1 &= \varphi_{10} + \varphi_{1c}, & \varphi_2 &= \varphi_{20} + \varphi_{2c} \\ \varrho_1 &= \varrho_{10} + \varrho_{1c}, & \varrho_2 &= \varrho_{20} + \varrho_{2c} \end{aligned} \quad (2.67)$$

where  $(\varphi_{10}, \varphi_{20}, \varrho_{10}, \varrho_{20})$  denote the predictors for the potential fields while the corresponding correctors are denoted by  $(\varphi_{1c}, \varphi_{2c}, \varrho_{1c}, \varrho_{2c})$ . The predictors for the potential fields are computed by performing a periodic calculation on a unit cell in every element of  $T_{h_1}$  and mapped on to  $T_{h_2}$ . The resulting fields are in general not continuous across the boundaries of elements of  $T_{h_1}$  and we use a  $L^2 \rightarrow H^1$  map to obtain conforming fields. In regions away from the defect-core, where the deformation field is slowly varying, the nature of the corrector fields is such that they do not exhibit fine-scale oscillations on the length-scale of the lattice parameter. This is justified in (Gavini and Liu (2011)) using formal multi-scale analysis, where a more general case of non-linear functionals is treated. Thus, corrector fields can now be accurately represented on a coarse-grained triangulation, like  $T_{h_3}$ , which has subatomic resolution in regions of rapid variation of the deformation field and is coarse-grained elsewhere.

The unknowns in the formulation comprising of the coarse-grained displacement field and correctors for potential fields are computed from the constrained saddle-

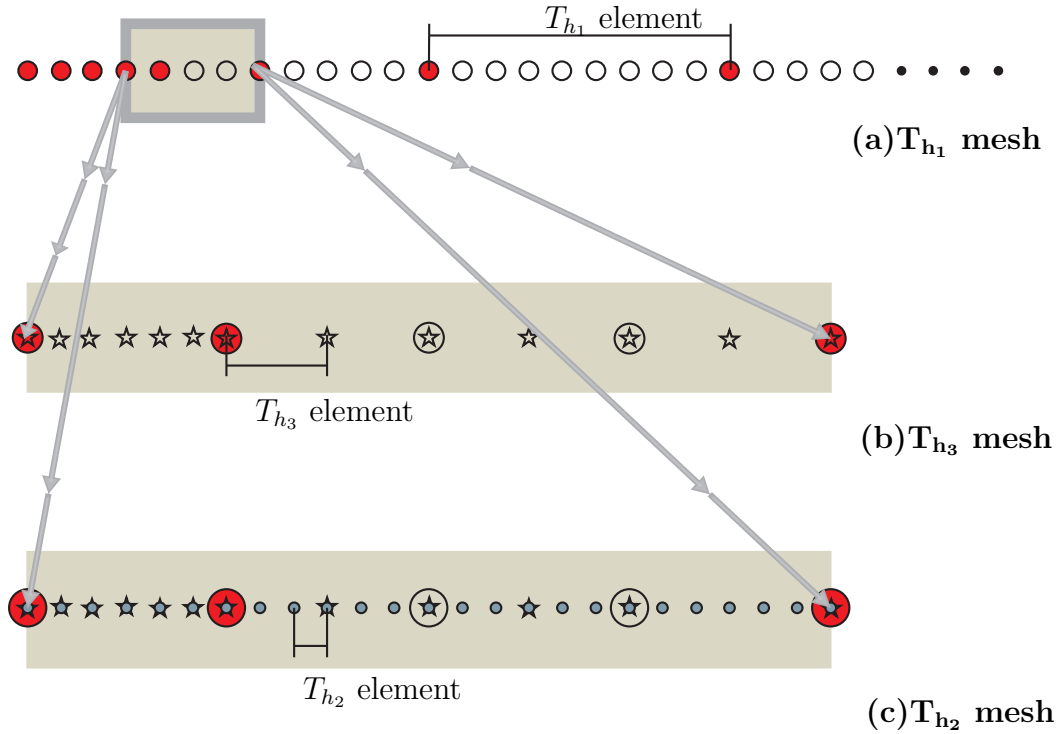


Figure 2.7: Schematic sketch of meshes: (a) Shows the atomic-mesh, which has atomistic resolution in regions of interest and is coarse-grained elsewhere. The circles in red denote representative atoms. (b) Shows the potential-mesh, used to represent the corrections to the predictor of potential fields. The stars in black represent the nodes of this mesh. It is subatomic in regions of interest and coarse-grains to become superatomic. (c) Shows the fine-mesh which resolves the predictor for the potential fields. The nodes of this mesh are small circles in blue. Unlike  $T_{h_1}$  and  $T_{h_3}$  which are coarse-grained,  $T_{h_2}$  is a uniform subatomic mesh everywhere.

point problem:

$$E_0^{hM} = \inf_{\mathbf{q}^h \in X_{h_1}} \inf_{\substack{\varphi_{1c}^h \in X_{h_3} \\ \varphi_{2c}^h \in X_{h_3}}} \sup_{\substack{\varphi_{10}^h \in X_{h_3} \\ \varphi_{20}^h \in X_{h_3}}} \int_{\Omega} L(\varphi_{10}^h + \varphi_{1c}^h, \varrho_{10}^h + \varrho_{1c}^h, \varphi_{20}^h + \varphi_{2c}^h, \varrho_{20}^h + \varrho_{2c}^h; \mathbf{q}^h) d\mathbf{y}. \quad (2.68)$$

Since the predictors for the potential fields are represented on a uniformly subatomic mesh  $T_{h_2}$ , the computation of the energy still has a complexity commensurate with the size of  $T_{h_2}$ . In regions of slowly varying deformations, which corresponds to coarse-grained regions of  $T_{h_1}$  and  $T_{h_3}$ , the predictor fields are accurate representations of potential fields and the corrector fields are very small compared to the predictors. We exploit this fact to introduce quadrature rules on integrals that reduce all the computations to the complexity of the coarse-grained mesh  $T_{h_3}$ . The precise form of the integration rule for an element  $e$  in the triangulation  $T_{h_3}$  is

$$\int_e f(\mathbf{y}) d\mathbf{y} \approx |e| \langle f \rangle_{D_e} \quad (2.69)$$

where  $|e|$  is the volume of element  $e$ ,  $D_e$  is the unit cell of an atom if such cell is contained in  $e$  or  $e$  otherwise, and  $\langle f \rangle_{D_e}$  is the average of  $f$  over  $D_e$ . Using (2.69), integration over the entire domain can be written as,

$$\int_{\Omega} f(\mathbf{y}) d\mathbf{y} = \sum_{e \in T_{h_3}} \int_e f(\mathbf{y}) d\mathbf{y} \approx \sum_{e \in T_{h_3}} |e| \langle f \rangle_{D_e}, \quad (2.70)$$

reducing all computations to have a complexity commensurate with the size of  $T_{h_3}$ . We note that this quadrature rule is exact for elements of  $T_{h_3}$  which are smaller than the unit cell, which we are labeled *subatomic* elements. The approximation is only introduced in elements that are larger than a unit cell, labeled as *superatomic* elements (c.f. figure 2.9). The nature of coarse-graining in triangulations is such that these superatomic elements lie in regions of smooth deformations where the corrector fields

are very small compared to the predictor fields. Thus, the integrand of equation (2.69) is a rapidly oscillating function with a small correction on the scale of the element. Hence, equation (2.69), for regions away from the core of a defect, denotes a zero order quadrature rule for rapidly oscillating functions.

Following the introduction of quadrature rules, predictor fields no longer need to be represented on a uniformly subatomic mesh everywhere in the domain, which is memory intensive. In the superatomic elements of  $T_{h_3}$ , where the quadrature approximation is used, it suffices to represent predictor fields on an auxiliary unit cell. This is demonstrated in figure 2.8, where  $T_{h_2}$  now represents a triangulation of disjoint simply connected domains formed from unit cells in each element of  $T_{h_3}$ . In the subatomic elements of  $T_{h_3}$ ,  $T_{h_2}$  represents a uniform triangulation of the underlying domain. In the superatomic elements of  $T_{h_3}$ ,  $T_{h_2}$  represents a uniform triangulation of the unit cell contained in the  $T_{h_3}$  element. The triangulations are constructed such that each simply connected domain will have boundaries that are planes of symmetry. This restriction ensures that the corrector fields vanish for a lattice undergoing affine deformations. In one-dimension it suffices to choose a triangulation such that the superatomic element have half-integer number of atoms as shown in figure 2.9. We further choose the triangulations and cell-complex in such a way that the integration rule is exact for all superatomic elements of  $T_{h_3}$  lying in the compact support of any shape-function in  $T_{h_1}$  that also contains one or more subatomic elements of  $T_{h_3}$ . We note that it is always possible to choose a triangulation and cell-complex that satisfies this requirement.

We now turn our attention to investigate if the quasi-continuum reduction of field formulations proposed here satisfies the consistency conditions laid out in section 2.1 (C1 and C2) for systematic convergence of numerical approximations. To this end, we consider a perfect crystal undergoing an affine deformation given by  $\mathbf{F} = \mathbf{A}\mathbf{X} + \mathbf{c}$ ,  $\mathbf{A}, \mathbf{c} \in \mathbb{R}^{3 \times 3}$ , and denote our domain of analysis by a super cell  $Q$

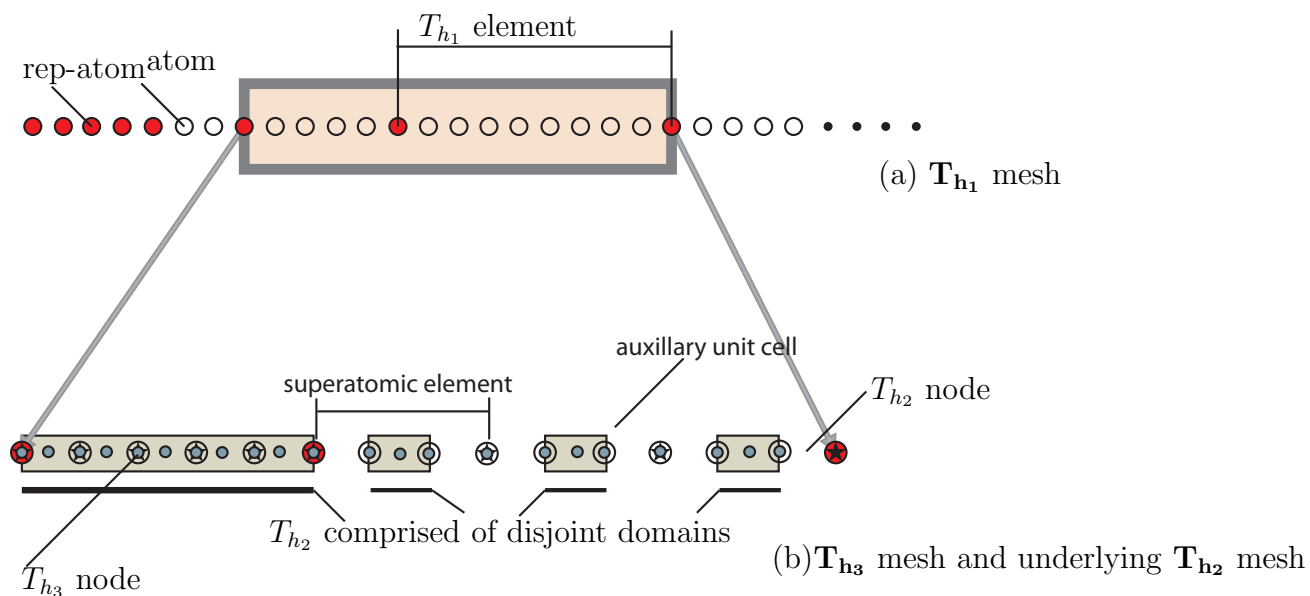


Figure 2.8: Schematic showing reduction in computational complexity upon introduction of quadrature rules. (a) Atomic-mesh: circles denote atomic sites; circles in red denote representative atoms (rep-atoms). (b) Potential-mesh and fine-mesh: small circles in blue denote  $T_{h_2}$  nodes; stars denote  $T_{h_3}$  nodes. The disjoint clusters representing the  $T_{h_2}$  mesh is enclosed in a light green box.

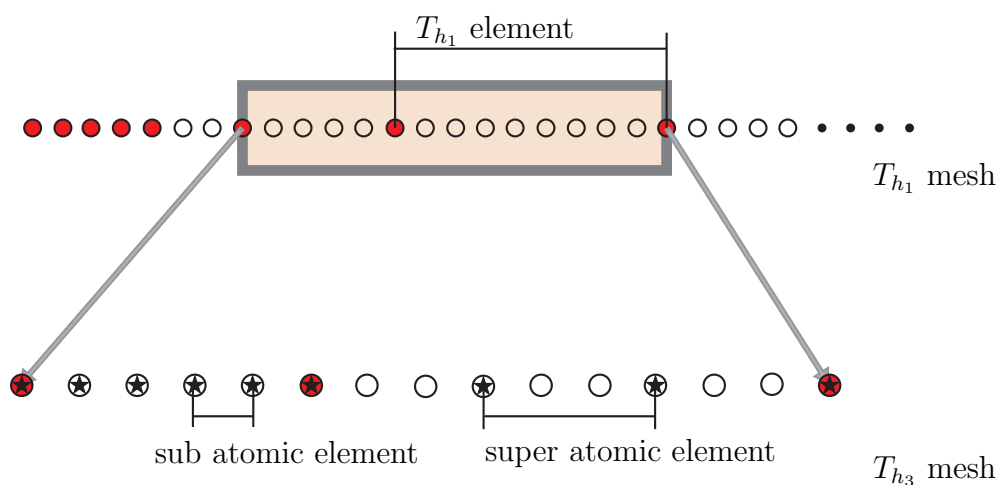


Figure 2.9: A triangulation showing a superatomic element and a subatomic element in the  $T_{h_3}$  mesh. The quadrature rule is exact in such a region.

containing  $N_0$  atoms. Further, we denote a unit cell in the lattice by  $U$ . The suitable function space for the corrector fields is  $H_{per}^1(Q)$ , which represents periodic boundary conditions on corrector fields. Further, we investigate the problem in the limit  $h_2 \rightarrow 0$ , where approximation errors in predictor fields are not considered, as we are interested in approximation errors corresponding to the coarse-grained fields. We note that the saddle-point problem given by equation (2.68) returns a trivial solution for the corrector fields. The energy is thus given by

$$\begin{aligned}
E_0^{hM} &= \inf_{\substack{\varphi_{1c}^h \in X_{h_3} \\ \varphi_{2c}^h \in X_{h_3}}} \sup_{\substack{\varphi_{1c}^h \in X_{h_3} \\ \varphi_{2c}^h \in X_{h_3}}} \int_Q L(\varphi_{10} + \varphi_{1c}^h, \varrho_{10} + \varrho_{1c}^h, \varphi_{20} + \varphi_{2c}^h, \varrho_{20} + \varrho_{2c}^h; \mathbf{F}) d\mathbf{y} \\
&= \int_Q L(\varphi_{10}, \varrho_{10}, \varphi_{20}, \varrho_{20}; \mathbf{F}) d\mathbf{y} = \sum_{e \in T_{h_3}} |e| \langle L \rangle_{D_e} \\
&= N_0 \int_U L(\varphi_{10}, \varrho_{10}, \varphi_{20}, \varrho_{20}; \mathbf{F}) d\mathbf{y}, \tag{2.71}
\end{aligned}$$

where the last equality follows from the restriction that each simply connected domain in  $T_{h_2}$  has boundaries that are planes of symmetry of lattice. Equation (2.71) demonstrates that the quadrature rule used satisfies the consistency condition C1.

We now investigate whether the proposed quasi-continuum reduction of field formulations passes the patch test. The force on any representative node is given by replacing the generator in equation (2.59) by the shape-function associated with the representative node:

$$(\mathbf{f}_{\mathbf{k}})_i = - \int_Q E_{ij} \frac{\partial \Phi_{\mathbf{k}}}{\partial y_j} d\mathbf{y} \quad i = 1, 2, 3, \quad \mathbf{k} \in \mathcal{L}_h, \tag{2.72}$$

where  $(\mathbf{f}_{\mathbf{k}})_i$  denotes the force in the  $i^{th}$  direction on a representative node  $\mathbf{k}$  in the triangulation  $T_{h_1}$ ;  $\Phi_{\mathbf{k}}$  denotes the shape-function associated with the representative node  $\mathbf{k}$ . We consider the following three cases to analyze the force expression: (i) the compact support of  $\Phi_{\mathbf{k}}$  contains only subatomic elements of  $T_{h_3}$ ; (ii) the compact

support of  $\Phi_{\mathbf{k}}$  contains only superatomic elements of  $T_{h_3}$ ; (iii) the compact support of  $\Phi_{\mathbf{k}}$  contains both subatomic and superatomic elements of  $T_{h_3}$ .

*Case (i):* The force is given by

$$\begin{aligned} (\mathbf{f}_{\mathbf{k}})_i &= - \int_Q \mathbf{E}_{ij} \frac{\partial \Phi_{\mathbf{k}}}{\partial y_j} dy = \sum_{e \in T_{h_3}} \int_e \mathbf{E}_{ij} \Phi_{\mathbf{k}} dy \\ &= \sum_{\mathbf{j} \in \mathcal{L}} (2CV_e \nabla \phi_1(\mathbf{x}_{\mathbf{j}}) - C^2 V_e \nabla \phi_2(\mathbf{x}_{\mathbf{j}}))_i \Phi_{\mathbf{k}}(\mathbf{x}_{\mathbf{j}}) = 0. \end{aligned} \quad (2.73)$$

The last equality follows from  $\nabla \phi_1(\mathbf{x}_{\mathbf{j}}) = 0$ ,  $\nabla \phi_2(\mathbf{x}_{\mathbf{j}}) = 0$ ,  $\mathbf{j} \in \mathcal{L}$ , for a lattice with affine deformation.

*Case (ii):* The force is given by

$$-(\mathbf{f}_{\mathbf{k}})_i = \sum_{e \in T_{h_3}} \int_e \mathbf{E}_{ij} \frac{\partial \Phi_{\mathbf{k}}}{\partial y_j} = \sum_{e \in T_{h_3}} |e| \langle \mathbf{E}_{ij} \frac{\partial \Phi_{\mathbf{k}}}{\partial y_j} \rangle_U \quad (2.74)$$

$$= \sum_{e \in T_{h_3}} |e| \langle \mathbf{E}_{ij} \rangle_U \langle \frac{\partial \Phi_{\mathbf{k}}}{\partial y_j} \rangle_U \quad (2.75)$$

$$= \langle \mathbf{E}_{ij} \rangle_U \sum_{e \in T_{h_3}} |e| \langle \frac{\partial \Phi_{\mathbf{k}}}{\partial y_j} \rangle_U = \langle \mathbf{E}_{ij} \rangle_U \int_Q \frac{\partial \Phi_{\mathbf{k}}}{\partial y_j} = 0 \quad (2.76)$$

We note that  $\langle \mathbf{E}_{ij} \frac{\partial \Phi_{\mathbf{k}}}{\partial y_j} \rangle_U = \langle \mathbf{E}_{ij} \rangle_U \langle \frac{\partial \Phi_{\mathbf{k}}}{\partial y_j} \rangle_U$  as  $\frac{\partial \Phi_{\mathbf{k}}}{\partial y_j}$  is a constant in every element  $e$  since  $\Phi_{\mathbf{k}}$  is a linear shape function, and  $\int_Q \frac{\partial \Phi_{\mathbf{k}}}{\partial y_j} = 0$  as  $\Phi_{\mathbf{k}}$  has a compact support in  $Q$ .

*Case (iii):* Noting that the quadrature rule is exact for the superatomic elements in this case, and using the results from Case (i) it follows that  $(\mathbf{f}_{\mathbf{k}})_i = 0$ .

Thus, the quasi-continuum reduction of field formulations proposed here satisfies the necessary consistency conditions for systematic convergence of approximations.



## 2.5 Numerical Examples

We consider *nanoindentation* on a semi-infinite chain of atoms in a 1D setting as a test case to present the numerical accuracy and salient features of the proposed field formulation, and compare with the node-based formulations proposed in *Knap and Ortiz* (2001) and *Eidel and Stukowski* (2009). Though the nanoindentation problem in 1D does not reveal the critical phenomenon of dislocation nucleation which is observed in higher dimensions, the displacement field obtained in 1D still has features similar to those obtained in 2D and 3D and hence serves as a good test case. To this end, we consider a chain consisting of 4110 atoms where one end of the chain is a free end, and the other end is fixed. The chain is extended beyond the fixed end to include atoms with fixed atomic positions that provide the environment of a semi-infinite chain. We use the Morse potential given by  $\bar{K}(|x_i - x_j|) = (1 - e^{-\alpha(|x_i - x_j| - x_e)})^2 - 1$  to describe the interatomic interactions. We choose the constants in the interatomic potential to be  $\alpha = 0.5$  and  $x_e = 2.8965$ , where units of all constants are in atomic units. The ground-state interatomic spacing of an infinite chain corresponding to these constants is  $a_0 = 1$ . We remark that our choice of constants is only a convenient choice for numerical implementation and does not represent any particular physical system. In order to simulate the nanoindentation of the semi-infinite chain, we load the free end using an indenter which applies an external force on the atoms. Following *Knap and Ortiz* (2001), we consider the external force from the indenter to be given by  $AH(R-r)(R-r)^3$ , where ‘R’ is the radius of the indenter, ‘r’ is the distance between the center of the indenter and the atomic site and  $H(r)$  is the heavy-side function. In our simulations we choose  $R = 5$  and  $A = 0.5$ . In order to compute the approximation errors, we first compute the ground-state energy and displacement in the the chain of atoms undergoing nanoindentation without introducing any approximations. The displacement field of an all-atom calculation is shown in figure 2.10, where  $X$  denotes the reference configuration and  $x$  denotes the deformed configuration. We note that

the deformation in the chain is rapidly varying close to the indenter and at the fixed end, but is uniform in most parts of the chain which is characteristic of an elastic response. We now proceed to introduce the approximations in the quasi-continuum method and compute the corresponding errors. We first consider the node-based formulation of *Knap and Ortiz* (2001), and subsequently consider the formulation in *Eidel and Stukowski* (2009).

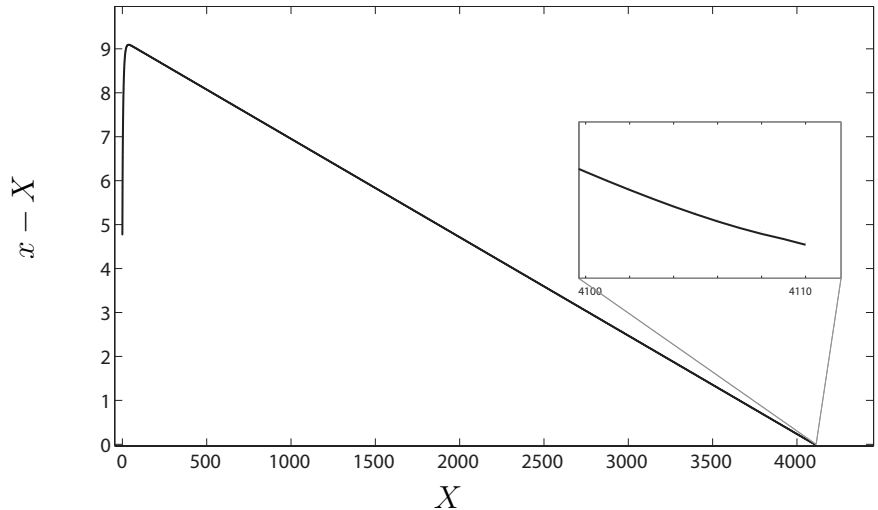


Figure 2.10: Displacement field obtained from an all-atom simulation of a chain of atoms loaded by an indenter.

In the formulation proposed in *Knap and Ortiz* (2001), node-based cluster rules are introduced independently on forces and energy. We consider a sequence of triangulations of representative atoms (rep-atoms) to study the approximation properties of this formulation. We denote the set of triangulations by  $\mathcal{T}^h$ , indexed by the number of rep-atoms, and are given by  $\mathcal{T}^h = \{35, 39, 47, 63, 95, 159, 251, 379, 463, 642, 1069, 3029, 3063\}$ . The sequence of triangulations are chosen such that finer triangulations form sub-grids of coarse triangulations, denoting a systematic refinement of the space of solutions. Figure 2.11 shows a triangulation with 95 rep-atoms. The triangulations are deliberately chosen to have rapid coarse-graining at the fixed end to study the robustness of the two QC formulations mentioned above. The convergence of quasi-continuum

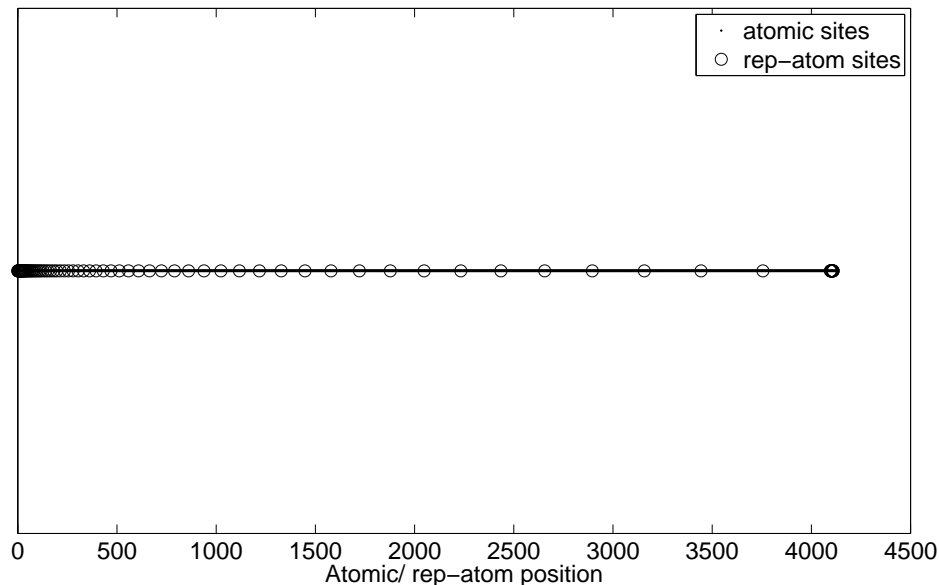
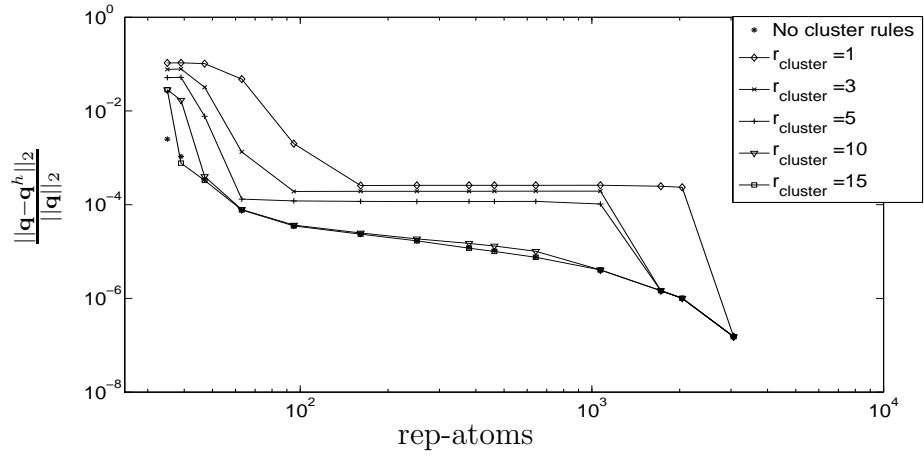


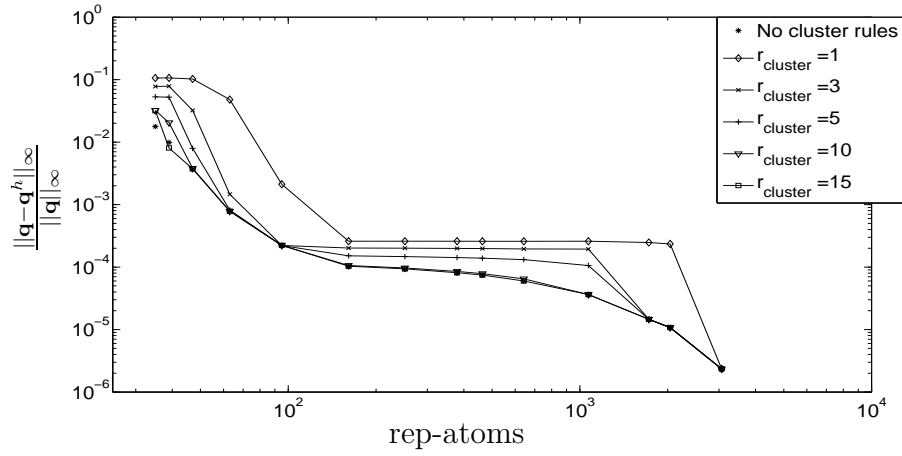
Figure 2.11: Coarse grained mesh with 95 rep-atoms in a chain consisting of 4110 nominal number of atoms.

formulations are measured using the approximation errors in computed positions of atoms (displacement field) given by  $\|\mathbf{q} - \mathbf{q}^h\|_2$ ,  $\|\mathbf{q} - \mathbf{q}^h\|_\infty$ , and the relative error in the energy given by  $\frac{|E - E^h|}{|E|}$ . Figure 2.12 shows the approximation errors for different number of rep-atoms and cluster radii. We note that these approximation errors can be decomposed into an error corresponding to coarse-graining (denoted by *coarse-graining error*), and another part corresponding to the approximations introduced through cluster summation rules (denoted by *quadrature error*). In the results shown in figure 2.12, the simulations performed without introducing cluster summation rules represent the coarse-graining error. Figure 2.13 demonstrates this decomposition and highlights the characteristics of the approximation errors. In our discussion, we will focus on the quadrature error as it is this error which determines the effectiveness of various formulations in the quasi-continuum method.

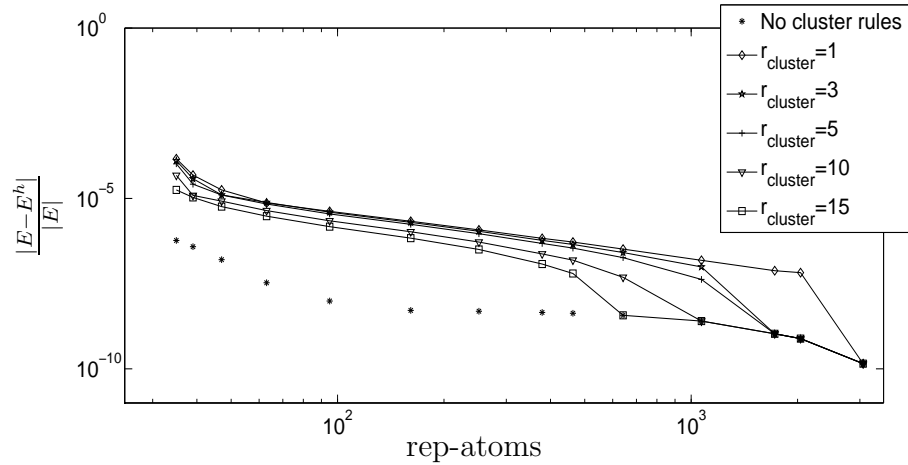
The nature of the approximation errors is such that three characteristic regions can be identified (cf. figure 2.13), at least for small cluster radii. In region I, corresponding to small number of rep-atoms, the approximation errors show an exponential drop



(a) Root mean squared error in displacement field.



(b) Supremum error in displacement field.



(c) Relative error in total energy evaluation.

Figure 2.12: Approximation errors in displacement field and total energy for formulation proposed in *Knap and Ortiz* (2001).

with increasing number of rep-atoms. However, these errors plateau very quickly, and in region II no significant reduction of the error is observed upon further increase in the number of representative atoms. This region corresponds to a constant quadrature error. When the number of representative atoms become large enough that the clusters start overlapping, the quadrature errors vanish, which is expected—this denoted by region III. The stagnation of approximation errors in region II suggest that the node-based cluster summation rules are not providing a systematic convergence of the approximation error.

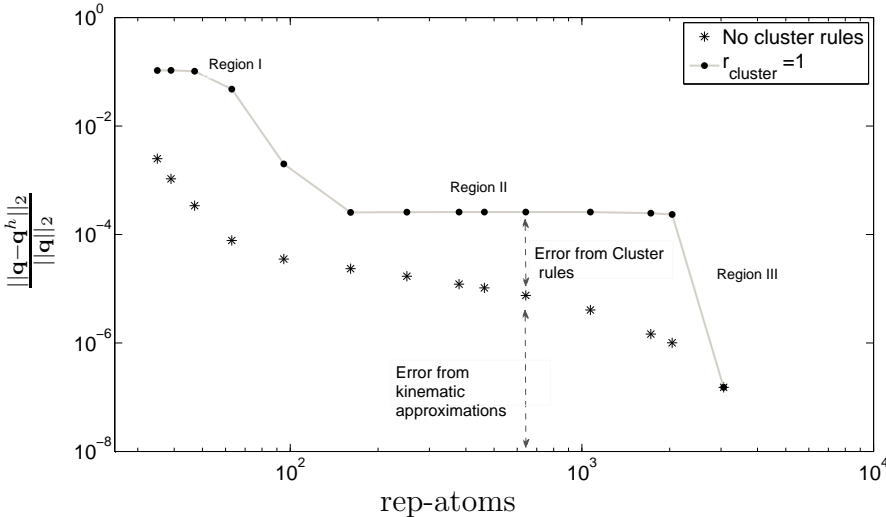


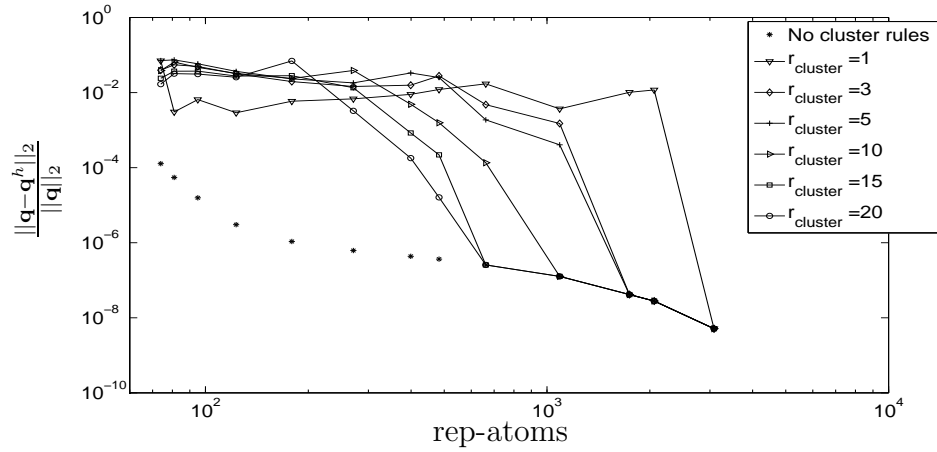
Figure 2.13: Approximation error created due to kinematic constraints (coarse-graining errors) and cluster rules (quadrature errors).

We now proceed to study the approximation errors in the node-based formulation suggested in *Eidel and Stukowski (2009)*, where node-based cluster summation rules are introduced on energy and the forces are computed as tangents of this approximate energy. As discussed in sections 2.1-2.2, this formulation does not pass the patch test and results in residual forces even for a periodic system. These residual forces can become arbitrarily large with increasing coarse-graining and size of elements, and require to be corrected. It is suggested in *Eidel and Stukowski (2009)* that the effect of residual forces can be nullified by computing these residual forces for an initial

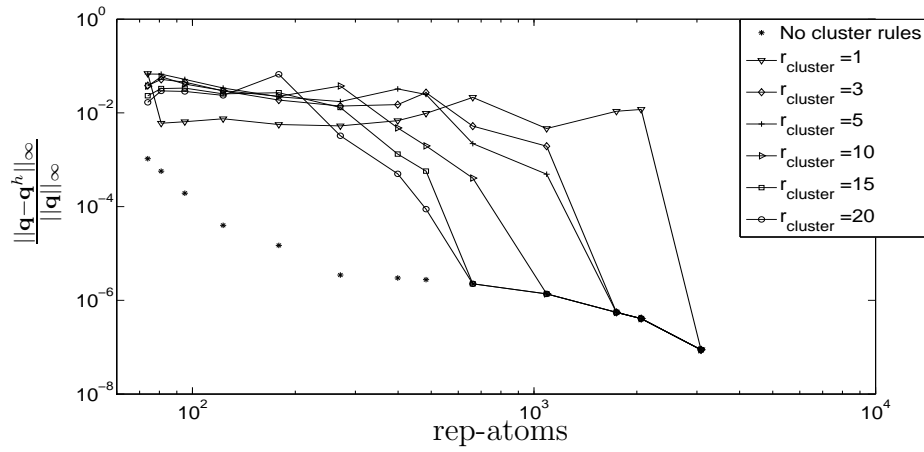
configuration and subtracting them out as a dead load.

In our simulations we find, for rapid coarse-graining rates, the force iterations do not converge even after subtracting the dead loads as these dead loads are orders of magnitude larger than the physical forces. Most of the triangulations that have been used to study the approximation errors in *Knap and Ortiz* (2001) have rapid coarse-graining at the fixed end, and the force iterations in *Eidel and Stukowski* (2009) formulation for these triangulations do not converge. Thus, we choose a different set of triangulations given by  $\mathcal{N}^h = \{74, 81, 95, 123, 179, 271, 399, 483, 662, 1089, 1743, 2059, 3083\}$ , where gradual coarse-graining is introduced on the fixed end. Figure 2.14 shows the approximation errors in displacement and relative energy for the node-based formulation in *Eidel and Stukowski* (2009). The nature of these errors is similar to the results obtained for the node-based formulation in *Knap and Ortiz* (2001), where the approximation errors are stagnant and do not improve with increasing number of rep-atoms until the clusters start to overlap. Further, the quadrature errors are significantly larger in this formulation in comparison to *Knap and Ortiz* (2001). These numerical results are in qualitative agreement with the error estimates in section 2.2 which suggest larger approximation errors in the force computations in *Eidel and Stukowski* (2009) in comparison to *Knap and Ortiz* (2001).

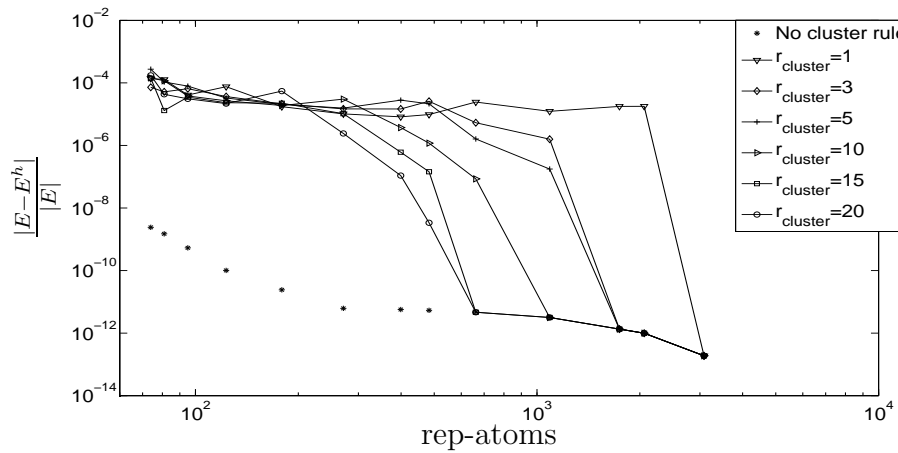
We further note that the spurious residual forces in *Eidel and Stukowski* (2009) change with deformation in the chain. Therefore, for a complete nullification of these residual forces, the dead loads have to be computed in a self-consistent manner and updated. We now investigate if the self-consistent iteration converges. We conduct two sets of numerical tests: (i) with the cluster radius fixed at 10 and consider different number of rep-atoms given by  $\{74, 271, 662\}$ ; (ii) with the number of rep-atoms fixed at 483 and consider different cluster radii  $r = \{5, 10, 15\}$ . Figure 2.15 shows the results of this study, where the  $\ell^2$  norm of the difference in the dead loads in iterations  $i$  and  $i - 1$  of the self-consistent loop is shown. The self-consistent iteration does not



(a) Root mean squared error in displacement field.



(b) Supremum error in displacement field.



(c) Relative error in total energy evaluation.

Figure 2.14: Approximation errors in displacement field and total energy for formulation proposed in *Eidel and Stukowski (2009)*.

necessarily converge, especially for small number of rep-atoms or small cluster radii. Numerical tests suggest that introducing linear mixing for the self-consistent iteration does not cure this deficiency.

To summarize, the numerical results suggest that the approximation errors do not systematically converge in the node-based QC formulations. The quadrature errors are found to be orders of magnitude larger than the coarse-graining errors even for moderately large number of rep-atoms. Moreover in the node-based QC formulation suggested in *Eidel and Stukowski (2009)* the self-consistent iteration which removes the effect of the residual forces may not always converge. We now proceed to study the approximation errors in the quasi-continuum reduction of the field formulation proposed in this thesis.

### 2.5.1 Field Formulation

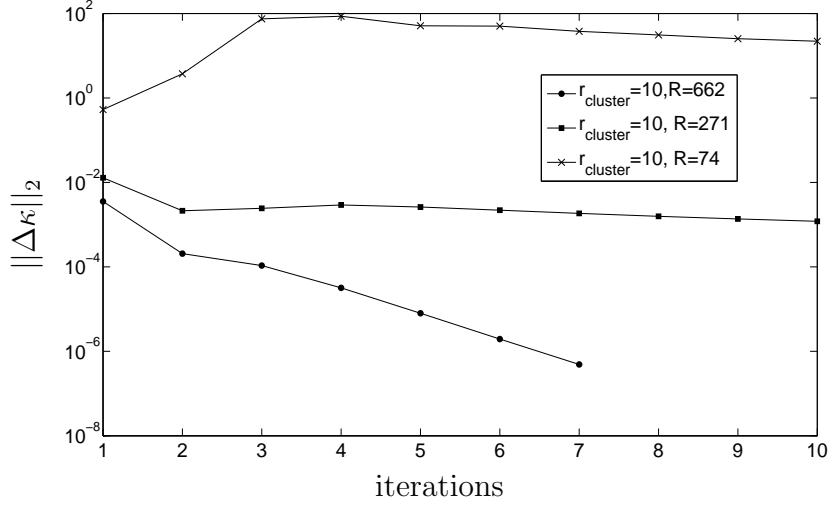
We numerically implement the variational formulation in equation (2.50) for the nanoindentation problem in 1D. Using the same notation as in section 2.3.1, the potential created by a given configuration of atoms  $b(y; \mathbf{q})$  is of the form

$$\phi(y; \mathbf{q}) = \int K(|y - y'|)b(y'; \mathbf{q})dy' \quad (2.77)$$

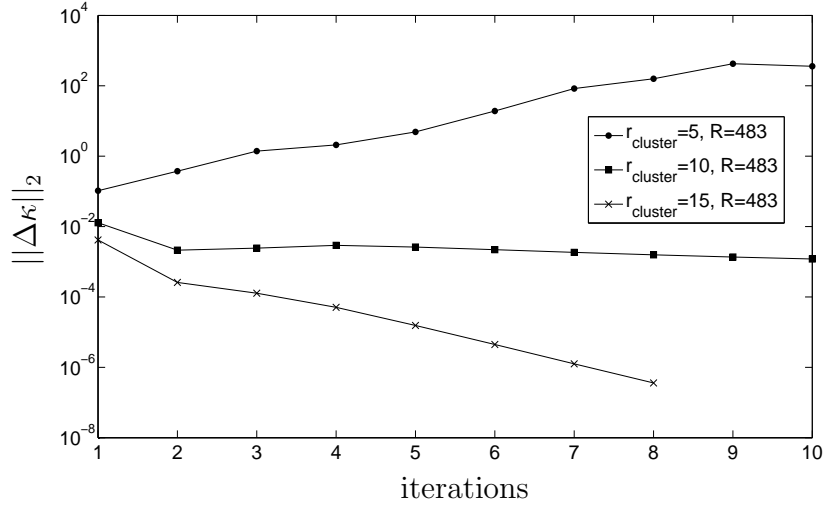
$$K(|y - y'|) = \left(1 - e^{-\alpha(|y - y'| - x_e)}\right)^2 - 1. \quad (2.78)$$

Let  $\phi_1(y; \mathbf{q}) = \int e^{-\alpha|y - y'|}b(y; \mathbf{q})dy'$ , and  $\phi_2(y; \mathbf{q}) = \int e^{-2\alpha|y - y'|}b(y; \mathbf{q})dy'$ . The desired potential can now be represented as  $\phi(y) = -2e^{\alpha x_e}\phi_1(y) + e^{2\alpha x_e}\phi_2(y)$ . Evaluation of the potentials  $\phi_1, \phi_2$  requires an evaluation of convolution integrals with non-local kernels. Following the ideas presented in section 2.3, and noting that the Fourier Transform of  $e^{-\alpha|y|}$  in one dimension is  $\frac{2\alpha}{y^2 + \alpha^2}$ , these potentials can be reformulated





(a) Self consistent iteration results for a fixed cluster radius and different number of rep-atoms.



(b) Self consistent iteration results for a fixed number of rep-atoms and different cluster radii.

Figure 2.15: Convergence study of the self-consistent iteration for residual force correction. Here  $\kappa(i)$  is the dead-load at the  $i^{\text{th}}$  iteration of the self consistent loop and  $\|\Delta\kappa(i)\|_2 = \|\kappa(i) - \kappa(i-1)\|_2$  is the  $\ell_2$  norm of change in dead-load against self-consistent iteration number.

into a local form using the following differential equations:

$$-\frac{d^2\phi_1(y; \mathbf{q})}{dy^2} + \alpha^2\phi_1(y; \mathbf{q}) = 2\alpha b(y; \mathbf{q}), \quad (2.79)$$

$$-\frac{d^2\phi_2(y; \mathbf{q})}{dy^2} + 4\alpha^2\phi_2(y; \mathbf{q}) = 4\alpha b(y; \mathbf{q}). \quad (2.80)$$

The problem of computing the ground-state solution can now be represented as the following saddle-point problem:

$$E_0 = \inf_{\mathbf{q} \in \mathbb{R}^M} \inf_{\varphi_1 \in \mathcal{X}} \sup_{\varphi_2 \in \mathcal{X}} L(\varphi_1, \varphi_2, \mathbf{q}), \quad (2.81)$$

where  $\mathcal{X}$  denotes the appropriate function space corresponding to the boundary conditions,  $M$  denotes the number of rep-atoms, and

$$\begin{aligned} L(\varphi_1, \varphi_2; \mathbf{q}) = & \frac{2e^{\alpha x_e}}{\alpha} \left( \frac{1}{2} \int |\nabla \varphi_1|^2 dy + \frac{\alpha^2}{2} \int \varphi_1^2 dy - 2\alpha \int \varphi_1(y) b(y; \mathbf{q}) dy \right) \\ & - \frac{e^{2\alpha x_e}}{2\alpha} \left( \frac{1}{2} \int |\nabla \varphi_2|^2 dy + 2\alpha^2 \int \varphi_2^2(y) dy - 4\alpha \int \varphi_2(y) b(y; \mathbf{q}) dy \right). \end{aligned} \quad (2.82)$$

We have numerically implemented the quasi-continuum reduction of the above saddle-point problem following the ideas developed in section 2.4. As in section 2.4, we denote the triangulation of the representative atoms as  $T_{h_1}$  (atomic-mesh), the triangulation resolving the corrector fields as  $T_{h_3}$  (potential-mesh), and the triangulation resolving the predictor fields as  $T_{h_2}$  (fine-mesh). We chose the triangulations such that discretization errors in the computation of physical forces are below  $10^{-10}$ . We used a nested iterative scheme for solving the saddle-point problem in equation (2.81), where for every displacement field given by  $\mathbf{q}^h$  the potential fields are computed by solving the inf – sup problem on  $(\phi_1^h, \phi_2^h)$ . We used a sparse-representation direct solve for solution of  $(\phi_1^h, \phi_2^h)$ , which is a linear problem, and a Levenberg-Marquardt iterative algorithm for solution of the non-linear problem corresponding to the minimization with respect to positions of atoms.

In order to determine the approximation errors in the proposed field formulation we have conducted three different studies. The first study considers coarse-graining of only the displacement field via selection of representative atoms. The potential fields are computed on the fine-mesh, i.e.  $T_{h_3} = T_{h_2}$ , and the coarse-graining of potential fields is suppressed. This study shows the approximation errors arising solely from coarse-graining of the displacement field. In the second study, along with coarse-graining of the displacement field, corrector fields are also represented using a coarse-grained triangulation. In other words, we consider  $T_{h_3}$  also to be a coarse-grained triangulation with subatomic resolution close to regions of interest and coarse-grained elsewhere. The approximation errors in this study arise from the coarse-graining of the displacement field as well as corrector fields. In the first two studies we do not introduce the quadrature rules proposed in equation (2.69). The third and final study introduces the quadrature rules as an additional approximation which then reduces all computations to the complexity commensurate with the coarse-grained triangulation  $T_{h_1}$ . The approximation errors in the third study include the coarse-graining errors from displacement and corrector fields, and the quadrature errors.

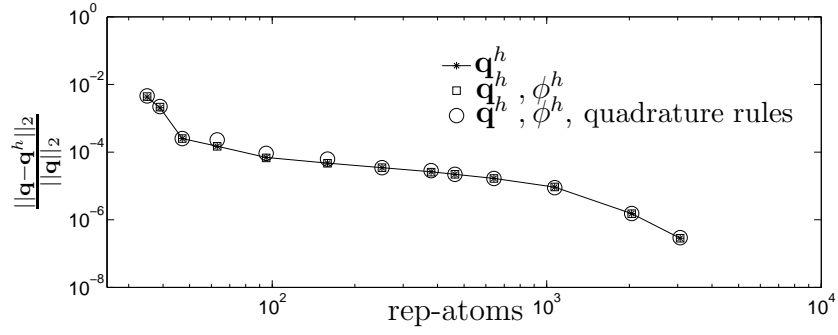
We have conducted the aforementioned three studies for the set of rep-atoms  $\mathcal{N}^h = \{35, 39, 47, 63, 95, 159, 251, 379, 463, 642, 1069, 3029, 3063\}$ —similar to the set used in the study of approximation errors in *Knap and Ortiz* (2001). Figure 2.16 shows the approximation errors in displacement fields and energy for the three studies with increasing number of rep-atoms. The data points from the first study, denoted by ‘\*’, show the displacement coarse-graining errors which are similar to the displacement coarse-graining errors for the node-based formulation in *Knap and Ortiz* (2001). The data points from the second study are denoted by ‘□’, and those from the third study are denoted by ‘○’. From figure 2.16 it is evident that the approximation errors corresponding to the coarse-graining of corrector fields and quadrature rules are negligible in comparison to the coarse-graining errors in the displacement

fields. These results are in sharp contrast to the node-based cluster rules where the quadrature errors are orders of magnitude larger than the coarse-graining errors. We argue that this remarkable improvement in the accuracy of the solution can be traced back to two key features of the quasi-continuum reduction of field theories. Firstly, the quadrature rules proposed in the quasi-continuum reduction of field formulations are element-based quadratures. As demonstrated in section 2.2, element-based cluster (quadrature) rules are more accurate in comparison to node-based cluster rules. Secondly, and more importantly, the notion of quadrature approximation is a local notion which is compatible with field formulations, and as demonstrated in section 2.4 satisfies the consistency conditions for systematic convergence of approximations.

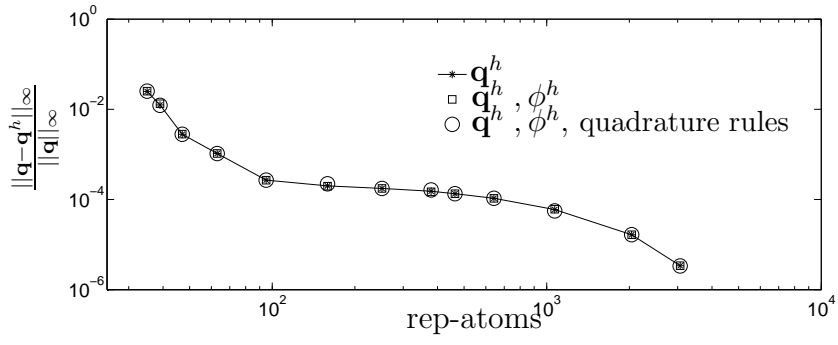
## 2.6 Summary

In summary, we have presented a solution to some of the long standing issues in the quasi-continuum method. The approximations involved in various versions of the QC method are known to result in undesirable features, which include a loss of variational structure leading to non-conservative forces, appearance of spurious forces on a perfect periodic lattice, possible lack of stability in the numerical approximations, etc. These in turn can undermine the numerical accuracy and systematic convergence of the QC method. In the present work, we identify the primary cause of these shortcomings to be the use of a non-local representation of energy to describe the extended interatomic interactions in materials. We demonstrate that cluster summation rules introduced on a non-local representation of energy result in a lack of consistency—approximation errors do not reduce with increasing refinement of the solution space. Cluster summation rules which are introduced in the spirit of numerical quadratures are derived from a local notion of numerical approximation, and result in inconsistent schemes when used on non-local representations of energy.

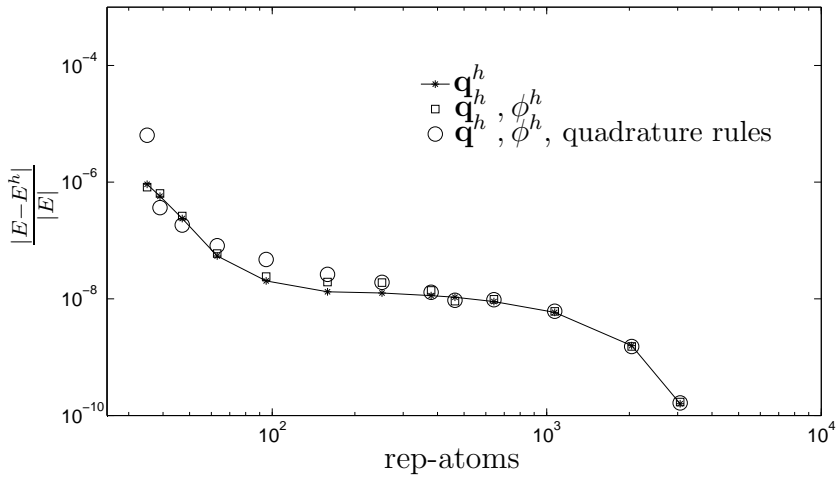
In the present work we resolve these outstanding issues by reformulating the ex-



(a) RMS error in displacement field



(b) supremum error in displacement field



(c) Relative error in total energy

Figure 2.16: Approximation errors in displacement and energy for the proposed field formulation of quasi-continuum method.  $\mathbf{q}^h$  represents coarse-grained displacement field while  $\phi^h$  represents coarse-grained potential field.

tended interatomic interactions into a local variational problem involving potential fields. We demonstrate this approach for commonly used interatomic potentials. We then introduce the quasi-continuum reduction of these potential fields following the ideas first suggested in *Gavini et al. (2007a)* in the context of electronic structure calculations. The key ideas behind the quasi-continuum reduction of field theories are: (i) decomposition of potential fields into predictor fields and corrector fields; (ii) an efficient representation of these fields using nested finite-element triangulations—predictor fields are resolved on an auxiliary unit cell, whereas corrector fields are represented on a coarse-grained triangulation; (iii) introduction of quadrature rules which reduce all computations to the complexity commensurate with the coarse-grained variables in the system. We demonstrate that the quasi-continuum reduction of field formulations satisfies the necessary conditions for a consistent numerical approximation, and hence may provide a systematic convergence of the approximation errors. Further, we show using numerical examples the remarkable improvement in the accuracy of the solution afforded by the suggested field approach to the QC method. Numerical results suggest that the approximation errors in a field approach are solely from the coarse-graining of displacement fields which can not be surpassed by any QC formulation. In comparison, other seamless QC formulations based on non-local representations of energy incur orders of magnitude larger numerical errors from quadrature approximations, and also suffer from a lack of systematic convergence.

The suggested field theoretic approach to the quasi-continuum method has the following properties. A single field theory is used to describe the physics in all regions of the model. The formulation is seamless and does not rely on any patching conditions. The formulation has a variational structure and thus the computed forces are conservative. The approximations introduced are consistent, and hence provide a systematic convergence to the exact solution. Moreover, the present work provides

a general framework for the quasi-continuum reduction of any field theory, where quasi-continuum reduction is solely a numerical coarse-graining technique.

It may appear that the computation of potential fields, which requires resolving these fields on a length-scale finer than interatomic distance, can significantly increase the computational cost. We note that the computation of these potential fields is mostly an overhead cost as it is the initial computation of these fields which is time consuming, and the subsequent evaluations are updates which require very few iterations. On the other hand, the field formulation provides a significant advantage as the computation of forces and energy is in turn a local computation involving the potential fields, unlike force and energy computations in conventional QC formulations. In our simulations, force evaluations in the field formulation were about four times more expensive than force evaluations in conventional node-based formulations. However, there is significant room for optimization in our preliminary implementation of the field formulation. For instance, the use of multi-grid approaches can significantly reduce the computational complexity of potential field calculations.

In the present work we have restricted our attention to a single component material system. Extending the present ideas to multi-component systems requires careful consideration as the PDE's describing potential fields can have different forms in different regions of the model, and presents itself as a direction for future investigations. Further, various numerical analysis aspects which include developing *a priori* error estimates, investigating the stability and accuracy of the formulation, developing effective preconditioned iterative solvers are potential directions for future investigations.

## CHAPTER III

### Real space formulation of Orbital Free DFT

Electronic structure calculations have been successful in accurately predicting a wide range of properties for a broad class of materials. They have been used to study materials in bulk, nanostructures, defects in crystals, isolated molecules and many more. The predictive capability of electronic structure calculations stems from the fact that they are derived from many-body quantum mechanics and incorporate much of the fundamental physics with little empiricism. One of the most widely used electronic structure theories is the Kohn Sham approach to the density functional theory (*Kohn and Sham* (1965)) in which the electron density distribution assumes the critical role, instead of the many-electron wave function. It is based on the Hohenberg-Kohn theorem (*Hohenberg and Kohn* (1964)) which states that there is a one-to-one correspondence between the many-electron wave-function of a quantum mechanical system and the ground-state electron-density. Based on the above result, the ground-state properties of any quantum-mechanical system can be described by an energy functional of the electron-density. While the existence of such an energy functional to describe the ground state properties is known, its functional representation is unknown to date. The Kohn-Sham approach addresses this challenge by proving the existence of an equivalent system consisting of non-interacting electrons moving in a mean field described by the electron density. This changes the computationally



intractable many-body problem to a computationally tractable system of many single body problems <sup>1</sup>. Kohn-Sham simulations are still very expensive, with computational cost scaling as cubic with the number of electrons in the system. The computational cost is dominated by the evaluation of the kinetic energy functional which requires computation of  $N$  single-electron wave functions in a system containing  $N$  electrons. In order to reduce the computational complexity of electronic structure calculations using DFT, approximate models for the kinetic energy have been proposed (*Parr and Yang (1989); Wang and Teter (1992); Smargiassi and Madden (1994); Wang et al. (1999, 2001)*). This approach is called as Orbital Free DFT (OFDFT) and various numerical studies have shown that this model is reasonable for systems with a valence electron density close to a uniform electron gas (*Wang et al. (2001, 1999); Huang and Carter (2008)*), e.g. for simple metals and Aluminum. Various efforts are underway to extend OFDFT to describe ionic and covalently bonded systems (*Huang and Carter (2010, 2012); Xia et al. (2012); Xia and Carter (2012)*).

### 3.1 Formulation

Let  $N$  and  $M$  denote the number of electrons and nuclei respectively, in a charge neutral system. The energy of the system (under the KS approximation) is given by

$$E(\rho, \mathbf{R}) = T_s(\rho) + E_{xc}(\rho) + E_H(\rho) + E_{ext}(\rho, \mathbf{R}) + E_{zz}(\mathbf{R}), \quad (3.1)$$

where  $\mathbf{R} = \{\mathbf{R}_1, \dots, \mathbf{R}_M\}$ ,  $\int \rho d\mathbf{x} = N$  is a list of nuclear coordinates in the system;  $T_s$  is the kinetic energy of non-interacting electrons;  $E_{xc}$  is the exchange correlation energy representing all many-body effects;  $E_H$  denotes the classical electrostatic interaction energy between electrons, also referred to as Hartree energy;  $E_{ext}$  represents the interaction energy of electrons with the external field  $V_{ext}$ , induced by

---

<sup>1</sup>While the non-interacting, independent particle description is in principle exact it is formulated in terms of an exchange-correlation functional for which only approximate models are available.

nuclear charges and  $E_{zz}$  is the repulsive energy between nuclei. Let  $u = \sqrt{\rho}$ , denote the square-root electron-density; In Orbital Free DFT,  $T_s$  is modeled as an explicit functional of electron-density and in our study we consider the Thomas-Fermi-von Weizsacker functional with kernel energies as proposed by *Wang et al.* (1999). The kernel functional is henceforth abbreviated as WGC (Wang-Govind-Carter) in this text.

### 3.1.1 Non Local Form

The kinetic energy of non-interacting electrons ( $T_s$ ), in OFDFT, has the form:

$$T_s(u) = \frac{3}{10}(3\pi^2)^{2/3} \int_{\Omega} u^{10/3}(\mathbf{x}) d\mathbf{x} + \frac{1}{2} \int_{\Omega} |\nabla u(\mathbf{x})|^2 d\mathbf{x} + \int_{\Omega} \int_{\mathbb{R}^3} u^{2\alpha}(\mathbf{x}) u^{2\beta}(\mathbf{x}') K(u(\mathbf{x}), u(\mathbf{x}'); |\mathbf{x} - \mathbf{x}'|) d\mathbf{x} d\mathbf{x}' \quad (3.2)$$

where  $\alpha, \beta = \frac{5}{3} \pm \frac{\sqrt{5}}{6}$  (c.f. *Wang et al.* (1999)). For  $E_{xc}$ , we use the local density approximation (LDA) which is given by

$$E_{xc}(u) = \int_{\Omega} \varepsilon_{xc}(u(\mathbf{x})) u^2(\mathbf{x}) d\mathbf{x} \quad (3.3)$$

where  $\varepsilon_{xc} = \varepsilon_x + \varepsilon_c$  is the exchange and correlation energy per electron of a *uniform* electron gas of density  $u^2$ . The exchange part is given by

$$\varepsilon_x = -\frac{3}{4} \left( \frac{3}{\pi} \right)^{1/3} u^{2/3} \quad (3.4)$$

while the correlation part has been estimated to high precision using Monte Carlo methods (c.f. *Ceperley and Alder* (1980); *Perdew and Zunger* (1981b)) and is given

by

$$\varepsilon_c(u) = \begin{cases} \frac{\gamma}{(1+\beta_1\sqrt{r_s}+\beta_2r_s)} & r_s \geq 1 \\ A \log r_s + B + C r_s \log r_s + D r_s & r_s < 1, \end{cases} \quad (3.5)$$

where  $r_s = \left(\frac{3}{4\pi u^2}\right)^2$ . The values of constants used in this study are those of an unpolarized medium, and are given by  $\gamma = -0.1471, \beta_1 = 1.1581, \beta_2 = 0.3446, A = 0.0311, B = -0.048, C = 0.0014, D = -0.0108$ .

The electrostatic interactions comprising of the Hartree, external and repulsive components take the form:

$$E_H(u) = \frac{1}{2} \int_{\Omega} \int_{\mathbb{R}^3} \frac{u^2(\mathbf{x})u^2(\mathbf{x}')}{|\mathbf{x} - \mathbf{x}'|} d\mathbf{x} d\mathbf{x}', \quad (3.6)$$

$$E_{ext}(u, \mathbf{R}) = \sum_J \int_{\Omega} u^2(\mathbf{x}) v_{ext}^J(|\mathbf{x} - \mathbf{R}_J|) d\mathbf{x}, \quad (3.7)$$

$$E_{ZZ}(\mathbf{R}) = \frac{1}{2} \sum_{I, J \neq I} \frac{Z_I Z_J}{|\mathbf{R}_I - \mathbf{R}_J|} \quad (3.8)$$

We note that, in a non-periodic setting like a finite atomic cluster, the domain volume  $\Omega$  in equations (3.2 - 3.6) is  $\mathbb{R}^3$  and the summations include all the atoms  $I$  and  $J$  in the system. In the case of an infinite periodic crystal,  $\Omega$  in equations (3.2 - 3.6) is the unit cell of the lattice. Similarly, the summation over  $I$  is on the atoms in the given cell, and summation over  $J$  extends over all lattice sites. We also note that even though the Hartree, external and repulsive energies individually diverge in an infinite crystal, their sum (the total electrostatic energy) is conditionally convergent.

The electrostatic terms and the kernel terms involve convolution integrals or double-sums over the lattice and their repeated evaluation is computationally, the most expensive part of the calculation. We now provide a brief description about the kinetic energy model in OFDFT.

### 3.1.2 Orbital Free DFT Kinetic Energy Model

Though the Kohn Sham kinetic energy functional is unknown in general, it can be evaluated for some asymptotic cases and these limits are enforced accurately by the Orbital Free DFT kinetic energy functional (c.f. *Wang et al. (1999)*). The limits are:

- Slowly varying electron density,

$$T_s \rightarrow T_{TF} + \frac{1}{9}T_{vW} \quad (3.9)$$

- Rapidly varying electron density,

$$T_s \rightarrow T_{TF} - \frac{3}{5}T_{vW} \quad (3.10)$$

- For small perturbations from a uniform electron gas

$$\hat{\mathbb{F}} \left[ \left( \frac{1}{4u(\mathbf{r})u(\mathbf{r}')} \frac{\delta^2 T_s}{\delta u(\mathbf{r})\delta u(\mathbf{r}')} \right) \Big|_{u_0} \right] = -\frac{1}{\chi_{Lind}} \quad (3.11)$$

where  $\delta/\delta u$  is the variational derivative,  $u_0$  is the average electron density,  $\hat{\mathbb{F}}$  denotes a Fourier transform and  $\chi_{Lind}$  is the Lindhard function (c.f. *Ashcroft and Mermin (2005)*).

In the above equations,  $T_{TF} = \frac{3}{10}(3\pi^2)^{2/3}u^{10/3}$ ,  $T_{vW} = \frac{1}{2}|\nabla u|^2$  are the Thomas-Fermi and Weizsacker kinetic energy functionals respectively. The kernel energy has a functional form

$$T_K(u) = \int \int u^{2\alpha}(\mathbf{x})u^{2\beta}(\mathbf{x}')K(u(\mathbf{x}), u(\mathbf{x}'); |\mathbf{x} - \mathbf{x}'|) d\mathbf{x} d\mathbf{x}' \quad (3.12)$$

It is evident that the kernel is dependent of the density and its re-evaluation for every new density will remove linear scaling of the problem. *Wang et al.* (1999) instead perform a Taylor expansion of the kernel about a reference uniform density to factor out density dependence in the kernel. The density dependent kernel in real space can be expanded to the the second order as

$$\begin{aligned}
K(u(\mathbf{x}), u(\mathbf{x}'); |\mathbf{x} - \mathbf{x}'|) &= K(u^*; |\mathbf{x} - \mathbf{x}'|) + \left. \frac{\partial K}{\partial u(\mathbf{x})} \right|_{u^*} \delta u(\mathbf{x}) \\
&+ \left. \frac{\partial K}{\partial u(\mathbf{x}')} \right|_{u^*} \delta u(\mathbf{x}') + \frac{1}{2} \left. \frac{\partial^2 K}{\partial^2 u(\mathbf{x})} \right|_{u^*} \delta^2 u(\mathbf{x}) \\
&+ \frac{1}{2} \left. \frac{\partial^2 K}{\partial^2 u(\mathbf{x}')} \right|_{u^*} \delta^2 u(\mathbf{x}') + \left. \frac{\partial^2 K}{\partial u(\mathbf{x}') \partial u(\mathbf{x})} \right|_{u^*} \delta u(\mathbf{x}') \delta u(\mathbf{x}) + \dots
\end{aligned} \tag{3.13}$$

where  $K = K(u(\mathbf{x}), u(\mathbf{x}'); |\mathbf{x} - \mathbf{x}'|)$ ,  $u^*$  is the reference uniform density and  $\delta u(\mathbf{x}) = u(\mathbf{x}) - u^*$ . Each of the partial derivatives in equation (3.13) are density-independent kernels. *Wang et al.* (1999) provide a functional form for each of these kernels in the Fourier space.

### 3.2 Local Reformulation of Orbital Free DFT

The computationally expensive part of the calculations are evaluation of convolution integrals in the electrostatic and kernel terms (equations 3.2, 3.6). Plane-wave basis sets have been the preferred choice in DFT (OF/KS) calculations, as they handle evaluation of non-local terms very efficiently through the use of Fast Fourier Transforms (c.f. *Kresse and Furthmüller* (1996); *Segall et al.* (2002); *Gonze et al.* (2002); *Hung et al.* (2010) ). However there are certain limitations: A plane-wave basis set restricts the geometry of simulation to dyadic domains which is incompatible with the displacement fields produced by most crystalline defects. Furthermore, a plane-wave basis can provide only a uniform grid resolution which is computationally

inefficient in the study of defects and non-periodic systems like molecules and clusters – a higher resolution is often desired to describe regions near the atoms, but a coarser resolution suffices elsewhere. Thus, plane-wave basis sets waste an enormous amount of computational effort to resolve empty space. Moreover, the non-locality of a plane-wave basis affects the scalability of computations on large parallel computing architectures. Finally, plane-wave basis sets, being in reciprocal space as they are, preclude the development of coarse grained approaches that are necessary to attempt electronic structure calculations of strong crystal defects. Thus, there is an increasing thrust towards using real-space techniques for electronic structure calculations (c.f. *Beck* (2000) and references therein for a comprehensive review). In order to develop a real space technique, an efficient technique must be obtained for evaluating the non-local interactions. We approach this by re-formulating the functionals involving extended interactions as local functionals through the introduction of auxiliary potential fields. We first present the approach for the electrostatic functional and follow it up with the local re-formulation for the kernel functional.

### 3.2.1 Electrostatics

The electrostatic interaction energy, comprising of Hartree, external and repulsive contributions is

$$\begin{aligned}
 E_{\text{electro}}(u, \mathbf{R}) &= \frac{1}{2} \int_{\Omega} \int_{\mathbb{R}^3} \frac{u^2(\mathbf{x})u^2(\mathbf{x}')}{|\mathbf{x} - \mathbf{x}'|} d\mathbf{x} d\mathbf{x}' + \sum_J \int_{\Omega} u^2(\mathbf{x})v_{ext}^J(|\mathbf{x} - \mathbf{R}_J|) d\mathbf{x} \\
 &+ \frac{1}{2} \sum_{I, J \neq I} \frac{Z_I Z_J}{|\mathbf{R}_I - \mathbf{R}_J|} \\
 &= E_H(u) + E_{ext}(u, \mathbf{R}) + E_{zz}(\mathbf{R})
 \end{aligned} \tag{3.14}$$

Following *Gavini et al.* (2007b), the electrostatic interaction energy can be reformulated as a local problem by observing that the kernel of the interaction,  $\frac{1}{|\mathbf{x} - \mathbf{x}'|}$ , is the

Green's function of the *Laplace* operator. To this end, we consider a nuclear charge  $Z_I$  located at  $\mathbf{R}_I$  as a bounded regularized charge distribution  $Z_I \tilde{\delta}_{\mathbf{R}_I}$  having a support in a small ball around  $\mathbf{R}_I$  and total charge  $Z_I$ . The nuclear repulsion energy can be subsequently represented as

$$\frac{1}{2} \int_{\Omega} \int_{\mathbb{R}^3} \frac{b(\mathbf{x})b(\mathbf{x}')}{|\mathbf{x} - \mathbf{x}'|} d\mathbf{x} d\mathbf{x}', \quad (3.15)$$

where  $b(\mathbf{x}) = \sum_{I=1}^M b_I(\mathbf{x}) = \sum_{I=1}^M Z_I \tilde{\delta}_{\mathbf{R}_I}(\mathbf{x})$ . However, equation (3.15) also includes the energy of a nuclear charge interacting with itself <sup>2</sup>. This is termed as self energy  $E_{\text{self}}$  and it must be computed and removed from equation (3.15). In other words,

$$E_{zz}(\mathbf{R}) = \frac{1}{2} \int_{\Omega} \int_{\mathbb{R}^3} \frac{b(\mathbf{x})b(\mathbf{x}')}{|\mathbf{x} - \mathbf{x}'|} d\mathbf{x} d\mathbf{x}' - E_{\text{self}}, \quad (3.16)$$

To calculate the self energy – interactions of charges with their own electrostatic field, we first consider the nucleus indexed  $I$ , with charge  $Z_I$  at location  $\mathbf{R}_I$  and electrostatic potential  $\tilde{\nu}_I(\mathbf{x})$ . The self energy of this nucleus is then  $\frac{1}{2} \int_{\mathbb{R}^3} b_I(\mathbf{x}) \tilde{\nu}_I(\mathbf{x}) d\mathbf{x}$ . The electrostatic field can be calculated by solving the Poisson equation

$$-\frac{1}{4\pi} \nabla^2 \tilde{\nu}_I(\mathbf{x}) = b_I(\mathbf{x}) \quad (3.17)$$

in a domain  $\Omega_I$  with boundary conditions  $\tilde{\nu}_I(\mathbf{x}) = \frac{Z_I}{|\mathbf{x} - \mathbf{R}_I|}$  on  $\partial\Omega_I$ . This can be expressed in a variational form as

$$\sup_{\nu_I \in \mathcal{V}_I} \left\{ -\frac{1}{8\pi} \int_{\Omega_I} |\nabla \nu_I(\mathbf{x})|^2 d\mathbf{x} + \int_{\Omega_I} b_I(\mathbf{x}) \nu_I(\mathbf{x}) d\mathbf{x} + \frac{1}{8\pi} \int_{\partial\Omega_I} \tilde{\nu}_I(\mathbf{x}) (\nabla \tilde{\nu}_I(\mathbf{x}) \cdot \mathbf{n}) \partial\Omega_I \right\}, \quad (3.18)$$

---

<sup>2</sup>On a continuous setting the self interactions are infinitely large due to the singular nature of the Coulomb potential. However, due to regularization of the nuclear charge, the singularities are softened and the interactions remain finite (though large).

where  $\mathcal{V}_I = H^1(\Omega_I)$  is the appropriate function space and  $\nu_I(\mathbf{x})$  denotes the trial function for the electrostatic potential created by nucleus  $I$ . From Eqs 3.17 and 3.18 the self interaction can be obtained by evaluating the extremal value of the functional :  $\frac{1}{2} \int_{\Omega_I} b_I(\mathbf{x}) \tilde{\nu}_I(\mathbf{x}) = \frac{1}{2} Z_I \tilde{\nu}_I(\mathbf{R}_I)$ . Extending to  $M$  atoms : For notational ease, let  $\nu = \{\nu_1, \dots, \nu_M\}$  be a vector collecting electrostatic fields created by the  $M$  nuclei and  $\mathcal{V} = \{\mathcal{V}_1, \dots, \mathcal{V}_M\}$  the same for the function spaces. The self energy is then given by:

$$E_{\text{self}} = E_{\text{self}}(\nu, \mathbf{R}) = \sup_{\nu \in \mathcal{V}} \left\{ \sum_{I=1}^M -\frac{1}{8\pi} \int_{\Omega_I} |\nabla \nu_I(\mathbf{x})|^2 d\mathbf{x} + \sum_{I=1}^M \int b_I(\mathbf{x}) \nu_I(\mathbf{x}) d\mathbf{x} + \sum_{I=1}^M \frac{1}{8\pi} \int_{\partial\Omega_I} \bar{\nu}_I(\mathbf{x}) (\nabla \bar{\nu}_I(\mathbf{x}) \cdot \mathbf{n}) d\mathbf{S}_I \right\}. \quad (3.19)$$

Subsequently, following a similar approach, the net electrostatic interaction energy in equation (3.14) can be re-formulated locally into:

$$E_{\text{electro}}(u, \phi, v_{\text{ext}}, \nu, \mathbf{R}) = E_{\phi}(u, \phi, \mathbf{R}) - E_{\text{self}}(\nu, \mathbf{R}) + \int_{\Omega} \sum_I u^2(\mathbf{x}) (v_{\text{ext}}^I(|\mathbf{x} - \mathbf{R}_I|) - \nu_I(\mathbf{x})) \quad (3.20)$$

$$E_{\phi}(u, \phi, \mathbf{R}) = \sup_{\phi \in \mathcal{Y}} \left\{ \frac{1}{8\pi} \int_{\Omega} |\nabla \phi(\mathbf{x})|^2 d\mathbf{x} - \int_{\Omega} (u^2(\mathbf{x}) + b(\mathbf{x})) \phi(\mathbf{x}) d\mathbf{x} \right\} \quad (3.21)$$

where  $\phi(\mathbf{x})$  denotes the trial function for the total electrostatic potential due to the electron density and the nuclear charge distribution. Since numerical computations are done on a finite-domain,  $\Omega$ , in non-periodic calculations, corresponds to a domain large enough to contain compact supports of  $u$  and  $\phi$  and  $\mathcal{Y} = H^1(\Omega)$ . For periodic calculations,  $\Omega$  spans the domain defining the unit cell and  $\mathcal{Y} = \{\phi : \phi \in$



$H_{per}^1(\Omega), \int_{\Omega} \varphi = 0$  <sup>3</sup>. We also note that the pseudopotential ( $v_{\text{ext}}(|\mathbf{x} - \mathbf{R}|)$ ) is necessarily local. Non-local pseudopotentials, common in KSDFE, cannot be used in OFDFT as there is no information about orbitals. Nevertheless, high quality local pseudopotentials are being developed for use in OFDFT (c.f. *Huang and Carter* (2008)).

### 3.2.2 Kinetic Energy

The kinetic energy functional has a non-local component with a generic form as given in equation (3.12). As discussed earlier in equation (3.13), the density dependent (DD) kernel is decomposed into a series of density independent (DI) kernels through a Taylor expansion of the kernel about a reference uniform density. The local reformulation of kernel energies has been addressed by *Radhakrishnan and Gavini* (2010) and is as follows: Defining the potentials  $V_{\alpha}(\mathbf{x})$  and  $V_{\beta}(\mathbf{x})$  as

$$V_{\alpha}(\mathbf{x}) = \int K(|\mathbf{x} - \mathbf{x}'|) u^{2\alpha}(\mathbf{x}') d\mathbf{x}' \quad (3.22a)$$

$$V_{\beta}(\mathbf{x}) = \int K(|\mathbf{x} - \mathbf{x}'|) u^{2\beta}(\mathbf{x}') d\mathbf{x}', \quad (3.22b)$$

we take the Fourier transform to obtain  $\hat{V}_{\alpha}(\mathbf{k}) = \hat{K}(\mathbf{k}) u^{2\alpha}(\mathbf{k})$  and  $\hat{V}_{\beta}(\mathbf{k}) = \hat{K}(\mathbf{k}) u^{2\beta}(\mathbf{k})$ . As shown by *Choly and Kaviras* (2002),  $\hat{K}$ , which is known in Fourier space, can be approximated to a reasonable accuracy using a sum of partial fractions of the following form:

$$\hat{K}(\mathbf{k}) \approx \sum_{J=1}^m \frac{A_J |\mathbf{k}|^2}{|\mathbf{k}|^2 + B_J}, \quad (3.23)$$

where  $A_J, B_J, J = 1 \dots m$  are complex constants determined using a best fit approximation. Using this approximation, the potentials defined in equation (3.22) take the

---

<sup>3</sup> $\int_{\Omega} \varphi = 0$  makes the problem well-posed and guarantees a unique solution

form

$$V_\alpha(\mathbf{x}) = \sum_{J=1}^m [\omega^{\alpha J}(\mathbf{x}) + A_J u^{2\alpha}(\mathbf{x})] , \quad (3.24a)$$

$$V_\beta(\mathbf{x}) = \sum_{J=1}^m [\omega^{\beta J}(\mathbf{x}) + A_J u^{2\beta}(\mathbf{x})] , \quad (3.24b)$$

where  $\omega^{\alpha J}(\mathbf{x})$  and  $\omega^{\beta J}(\mathbf{x})$  are referred to as kernel potentials and are solutions to the following Helmholtz equations for  $J = 1 \dots m$ :

$$-\nabla^2 \omega^{\alpha J} + B_J \omega^{\alpha J} + A_J B_J u^{2\alpha} = 0 , \quad (3.25a)$$

$$-\nabla^2 \omega^{\beta J} + B_J \omega^{\beta J} + A_J B_J u^{2\beta} = 0 . \quad (3.25b)$$

In the interest of clarity, we note that  $\alpha_J$  in  $\omega^{\alpha J}$  is only a superscript, and should not be interpreted as the power of  $\omega$  (and likewise for  $\omega^{\beta J}$ ). For convenience of notation, we define  $\tilde{\omega}^\alpha = \{\omega^{\alpha 1}, \omega^{\alpha 2}, \dots, \omega^{\alpha m}\}$  and  $\tilde{\omega}^\beta = \{\omega^{\beta 1}, \omega^{\beta 2}, \dots, \omega^{\beta m}\}$ , which denote the vectors containing the corresponding kernel potentials. The Helmholtz equations in equation (3.25) can be expressed in a variational form which allows us to reformulate the non-local energies as the following local saddle-point problem:

$$T_k(u) = \inf_{\tilde{\omega}^\alpha \in \mathcal{Z}} \sup_{\tilde{\omega}^\beta \in \mathcal{Z}} \bar{L}(u, \tilde{\omega}^\alpha, \tilde{\omega}^\beta) , \quad (3.26)$$

where

$$\begin{aligned} \bar{L}(u, \tilde{\omega}^\alpha, \tilde{\omega}^\beta) = \sum_{J=1}^m \left\{ \int_{\Omega} \left[ \frac{1}{A_J B_J} \nabla \omega^{\alpha J} \cdot \nabla \omega^{\beta J} + \frac{1}{A_J} \omega^{\alpha J} \omega^{\beta J} \right. \right. \\ \left. \left. + \omega^{\beta J} u^{2\alpha} + \omega^{\alpha J} u^{2\beta} + A_J u^{2(\alpha+\beta)} \right] d\mathbf{x} \right\} . \end{aligned} \quad (3.27)$$

In the saddle-point problem in equation (3.26), the function space is chosen to be  $\mathcal{Z} = (H_{per}^1)^m$  for periodic problems where  $\Omega$  denotes the unit-cell in the periodic

calculation, and in non-periodic problems it is  $\mathcal{Z} = (H^1)^m$ . In systems involving vacuum, the WGC Kernel diverges at very low electron densities and all kernels are suppressed in such regions (c.f. *Shin et al.* (2009b)). Using the local reformulation of the electrostatic interactions from equations (3.19, 3.20) and kernel energies from equation (3.26), the problem of computing the ground-state properties in orbital-free DFT, for a fixed position of atoms and on bounded domains, can now be expressed as the following local saddle-point problem:

$$\inf_{u \in \mathcal{X}} \sup_{\phi \in \mathcal{Y}} \inf_{\tilde{\omega}^\alpha \in \mathcal{Z}} \sup_{\tilde{\omega}^\beta \in \mathcal{Z}} \inf_{\nu \in \mathcal{V}} \tilde{L}(u, \phi, v_{\text{ext}}, \nu, \tilde{\omega}^\alpha, \tilde{\omega}^\beta, \mathbf{R}) \quad \text{subject to: } \int_{\Omega} u^2 d\mathbf{x} = N, \quad (3.28)$$

where

$$\tilde{L}(u, \phi, v_{\text{ext}}, \nu, \tilde{\omega}^\alpha, \tilde{\omega}^\beta, \mathbf{R}) = L(u, \phi, \nu, \mathbf{R}) + \bar{L}(u, \tilde{\omega}^\alpha, \tilde{\omega}^\beta), \quad (3.29)$$

and

$$\begin{aligned} L(u, \phi, v_{\text{ext}}, \nu, \mathbf{R}) &= C_F \int_{\Omega} u^{10/3}(\mathbf{x}) d\mathbf{x} + \frac{1}{2} \int_{\Omega} |\nabla u(\mathbf{x})|^2 d\mathbf{x} + \int_{\Omega} \varepsilon_{xc}(u^2(\mathbf{x}))u^2(\mathbf{x}) d\mathbf{x} \\ &\quad - \frac{1}{8\pi} \int_{\Omega} |\nabla \phi(\mathbf{x})|^2 d\mathbf{x} + \int_{\Omega} (u^2(\mathbf{x}) + b(\mathbf{x}))\phi(\mathbf{x}) d\mathbf{x} \\ &\quad + \sum_{I=1}^M \frac{1}{8\pi} \int_{\Omega_I} |\nabla \nu_I(\mathbf{x})|^2 d\mathbf{x} - \sum_{I=1}^M \int_{\Omega_I} b_I(\mathbf{x})\nu_I(\mathbf{x}) d\mathbf{x} \\ &\quad - \sum_{I=1}^M \frac{1}{8\pi} \int_{\partial\Omega_I} \bar{\nu}_I(\mathbf{x})(\nabla \bar{\nu}_I(\mathbf{x}) \cdot \mathbf{n}) \partial\Omega_I \\ &\quad + \int_{\Omega} \sum_I u^2(\mathbf{x}) (v_{\text{ext}}^I(|\mathbf{x} - \mathbf{R}_I|) - \nu_I(\mathbf{x})) , \end{aligned} \quad (3.30)$$

where  $\mathcal{X} = \mathcal{Y}$  and  $\bar{L}$  is given in equation (3.27).

### 3.3 Atomic Relaxation

We have so far considered the problem of computing ground-state electron density for a fixed set of atom positions and now consider computation of forces on atoms. When the system is at ground state with respect to electron density, the Hellmann-Feynman theorem (c.f *Hellmann* (1939)) applies, and force on a nucleus indexed  $I$  is simply  $f_I = -\frac{\partial \tilde{L}}{\partial \mathbf{R}_I}$ , which is

$$\begin{aligned} \mathbf{f}_I = & -\frac{\partial}{\partial \mathbf{R}_I} \sum_{K=1}^M \int_{\Omega} Z_K \tilde{\delta}(\mathbf{x} - \mathbf{R}_K) \phi(\mathbf{x}) + \frac{\partial}{\partial \mathbf{R}_I} \sum_{K=1}^M \int_{\Omega_K} Z_K \tilde{\delta}(\mathbf{x} - \mathbf{R}_K) \nu_K(\mathbf{x}) d\mathbf{x} \\ & - \frac{\partial}{\partial \mathbf{R}_I} \sum_K \int_{\Omega} u^2(\mathbf{x}) (v_{\text{ext}}^K(|\mathbf{x} - \mathbf{R}_K|) - \nu_K(|\mathbf{x} - \mathbf{R}_K|)) \end{aligned} \quad (3.31)$$

The first 2 terms can be simplified as:

$$\begin{aligned} & \int_{\Omega} Z_I \frac{\partial}{\partial \mathbf{x}} \tilde{\delta}(\mathbf{x} - \mathbf{R}_I) \phi(\mathbf{x}) d\mathbf{x} - \int_{\Omega_I} Z_I \frac{\partial}{\partial \mathbf{x}} \tilde{\delta}(\mathbf{x} - \mathbf{R}_I) \nu_I(\mathbf{x}) d\mathbf{x} \quad \because \frac{\partial \tilde{\delta}(\mathbf{x} - \mathbf{R}_I)}{\partial \mathbf{R}_I} = -\frac{\partial \tilde{\delta}(\mathbf{x} - \mathbf{R}_I)}{\partial \mathbf{x}} \\ = & - \int_{\Omega} Z_I \tilde{\delta}(\mathbf{x} - \mathbf{R}_I) \frac{\partial}{\partial \mathbf{x}} \phi(\mathbf{x}) d\mathbf{x} + \int_{\Omega_I} Z_I \tilde{\delta}(\mathbf{x} - \mathbf{R}_I) \frac{\partial}{\partial \mathbf{x}} \nu_I(\mathbf{x}) d\mathbf{x} \\ = & -Z_I \nabla \phi(\mathbf{R}_I) + Z_I \nabla \nu_I(\mathbf{R}_I) \end{aligned} \quad (3.32)$$

The force on a nucleus, as coming from the Hellman-Feynman theorem is thus:

$$\mathbf{f}_I = -Z_I \nabla \phi(\mathbf{R}_I) + Z_I \nabla \nu_I(\mathbf{R}_I) + \int_{\Omega} u^2(\mathbf{x}) \nabla (v_{\text{ext}}^I(|\mathbf{x} - \mathbf{R}_I|) - \nu_I(|\mathbf{x} - \mathbf{R}_I|)) \quad (3.33)$$

However, computing atomic forces this way has a significant drawback: Equation (3.33) does not capture the stress in the cell as it produces the same force for any affine deformation on the system, and fails to capture effects of elastic deformation on the crystal. Hence we turn to calculation of configurational force on the system and obtain the *Eshelby* form for forces. This gives a single expression that captures both,

forces on atoms and elastic stresses on the crystal. We define a bijective mapping  $\psi_\epsilon(\mathbf{x})$  for every point in space with the following properties:

$$\begin{aligned} \psi_\epsilon(\mathbf{x}) &: \Omega \rightarrow \Omega', \quad \psi_0 = \mathbb{I} \\ \mathbf{x}' &= \psi_\epsilon(\mathbf{x}) = \mathbf{x} + \epsilon\mathbf{\Gamma}(\mathbf{x}) \\ \left. \frac{d}{d\epsilon}\psi_\epsilon(\mathbf{x}) \right|_{\epsilon=0} &= \mathbf{\Gamma}(\mathbf{x}) \end{aligned} \quad (3.34)$$

The map  $\psi_\epsilon(\mathbf{x})$  can be physically interpreted as perturbing every point  $\mathbf{x}$  in space along some direction  $\mathbf{\Gamma}(\mathbf{x})$  to a new point  $\mathbf{x}' = \mathbf{x} + \epsilon\mathbf{\Gamma}(\mathbf{x})$ . In this mapping we also require the nuclear charge distribution be unchanged. To this end we constrain the mapping so that it does not compress, dilate or shear in the region where  $b(\mathbf{x}, \mathbf{R}) \neq 0$ . This restricts the mapping to rigid body motions on the compact support of the nucleus, i.e.  $\psi_\epsilon(\mathbf{x}) = Q_\epsilon^I \mathbf{x} + T_\epsilon^I, I = 1 : M$  in the compact support of  $b_I(\mathbf{x}, \mathbf{R})$ . Here,  $Q^I$  is unitary and  $Q^I, T^I$  are independent of  $\mathbf{x}$ . We show the derivation for  $E_\phi$  in equation (3.20) and it follows along similar lines for the rest of the Lagrangian. Due to the infinitesimal variations introduced by the mapping,  $E_\phi$  is now given by

$$E_\phi = E_\phi(\psi_\epsilon(\mathbf{x})) \quad (3.35)$$

$$E_\phi = -\frac{1}{8\pi} \int_{\Omega'} |\nabla_{\mathbf{x}'} \phi(\mathbf{x}')|^2 d\mathbf{x}' + \int_{\Omega'} (u^2(\mathbf{x}') + b(\mathbf{x}', \mathbf{R}')) \phi(\mathbf{x}') d\mathbf{x}' \quad (3.36)$$

Since  $b(\mathbf{x}, \mathbf{R}) = b(|\mathbf{x} - \mathbf{R}|)$  and  $\psi_\epsilon(\mathbf{x}) = Q_\epsilon^I \mathbf{x} + T_\epsilon^I$  in the compact support of  $b$ ,

$$\begin{aligned} b(|\mathbf{x}' - \mathbf{R}'|) &= \sum_{I=1}^M Z_I \tilde{\delta}(|\mathbf{x}' - \mathbf{R}'_I|) = \sum_{I=1}^M Z_I \tilde{\delta}(|Q_\epsilon^I \mathbf{x} - Q_\epsilon^I \mathbf{R}_I|) \\ &= \sum_{I=1}^M Z_I \tilde{\delta}(|\mathbf{x} - \mathbf{R}_I|) = b(|\mathbf{x} - \mathbf{R}|) \end{aligned} \quad (3.37)$$

Using Equation 3.37, Equation 3.36 now becomes

$$E_\phi(\psi_\epsilon) = -\frac{1}{8\pi} \int_{\Omega'} |\nabla_{\mathbf{x}'} \phi(\mathbf{x}')|^2 d\mathbf{x}' + \int_{\Omega'} (u^2(\mathbf{x}') + b(\mathbf{x}, \mathbf{R})) \phi(\mathbf{x}') d\mathbf{x}' \quad (3.38)$$

Transforming the integrals back onto  $\Omega$ , we obtain in indicial notation,

$$\begin{aligned} E_\phi(\psi_\epsilon) &= -\frac{1}{8\pi} \int_{\Omega} \frac{\partial \phi(\psi_\epsilon(\mathbf{x}))}{\partial x_j} \frac{\partial x_j}{\partial x'_i} \frac{\partial \phi(\psi_\epsilon(\mathbf{x}))}{\partial x_k} \frac{\partial x_k}{\partial x'_i} \det\left(\frac{\partial x'_l}{\partial x_m}\right) d\mathbf{x} \\ &\quad + \int_{\Omega} (u^2(\psi_\epsilon(\mathbf{x})) + b(\mathbf{x}, \mathbf{R})) \phi(\psi_\epsilon(\mathbf{x})) \det\left(\frac{\partial x'_l}{\partial x_m}\right) d\mathbf{x} \end{aligned} \quad (3.39)$$

We first note that in taking the variation of  $E_\phi(\psi_\epsilon)$  (to follow) :

1.  $b(\mathbf{x}, \mathbf{R})$  is independent of  $\epsilon$  and does not contribute to the variations.
2. The terms arising from the variations of  $u(\psi_\epsilon), \phi(\psi_\epsilon)$  vanish as  $u, \phi$  satisfy the Euler-Lagrange equations in 3.30.
3. The non-vanishing contributions to  $\frac{dE_\phi(\psi_\epsilon)}{d\epsilon}$  come from variations of  $\det\left(\frac{\partial \mathbf{x}'}{\partial \mathbf{x}}\right)$  and  $\frac{\partial \mathbf{x}}{\partial \mathbf{x}'}$ .

We also note the following identities :

$$\begin{aligned} \frac{d}{d\epsilon} \left\{ \frac{\partial x'_i}{\partial x_j} \right\} \Big|_{\epsilon=0} &= \frac{\partial \Gamma_i(\mathbf{x})}{\partial x_j} \\ \frac{d}{d\epsilon} \left\{ \frac{\partial x_i}{\partial x'_j} \right\} \Big|_{\epsilon=0} &= -\frac{\partial x_i}{\partial x'_k} \left( \frac{d}{d\epsilon} \frac{\partial x'_k}{\partial x_l} \right) \frac{\partial x_l}{\partial x'_j} \Big|_{\epsilon=0} \\ &= -\frac{\partial \Gamma_i(\mathbf{x})}{\partial x_j}; \quad \because \left( \frac{\partial x_i}{\partial x'_j} \Big|_{\epsilon=0} = \delta_{ij} \right) \end{aligned} \quad (3.40)$$

$$\begin{aligned} \frac{d}{d\epsilon} \left\{ \det\left(\frac{\partial x'_i}{\partial x_j}\right) \right\} \Big|_{\epsilon=0} &= \det\left(\frac{\partial x'_i}{\partial x_j}\right) \frac{\partial x_j}{\partial x'_i} \left( \frac{d}{d\epsilon} \frac{\partial x'_i}{\partial x_j} \right) \Big|_{\epsilon=0} \\ &= \frac{\partial \Gamma_j(\mathbf{x})}{\partial x_j} \end{aligned} \quad (3.41)$$

Using the above identities and noting that  $\psi_0 = \mathbb{I}$ , the Gâteaux derivative (generalized directional derivative) of the energy functional in Equation 3.39 is given by

$$\begin{aligned} \left. \frac{dE_\phi(\psi_\epsilon(\mathbf{x}))}{d\epsilon} \right|_{\epsilon=0} &= \int_{\Omega} \left( -\frac{1}{8\pi} |\nabla\phi|^2 + (u^2 + b(\mathbf{R}))\phi \right) \frac{\partial\Gamma_j(\mathbf{x})}{\partial x_j} d\mathbf{x} + \frac{1}{4\pi} \int_{\Omega} \frac{\partial\phi}{\partial x_i} \frac{\partial\phi}{\partial x_j} \frac{\partial\Gamma_i(\mathbf{x})}{\partial x_j} d\mathbf{x} \\ &= \int_{\Omega} \left( -\frac{1}{8\pi} |\nabla\phi|^2 + u^2\phi \right) \frac{\partial\Gamma_j(\mathbf{x})}{\partial x_j} d\mathbf{x} + \frac{1}{4\pi} \int_{\Omega} \frac{\partial\phi}{\partial x_i} \frac{\partial\phi}{\partial x_j} \frac{\partial\Gamma_i(\mathbf{x})}{\partial x_j} d\mathbf{x} \end{aligned} \quad (3.42)$$

where the above equation follows because  $\nabla \cdot \mathbf{\Gamma} = 0$ , if  $b \neq 0$ . The gradient at any atom  $I$ , along direction  $i$  can be obtained by setting  $\Gamma_i(\mathbf{x}) = 1$  in the support of atom  $I$  and  $\Gamma(\mathbf{x}) = 0$  outside it. It can be shown that, when  $\Gamma(\partial\Omega) = 0$  – no external deformation – the Gâteaux derivative in equation (3.42) is equivalent to the Hellman-Feynman force. To compute the Gâteaux derivative of  $E_{\text{self}}$ , we make an additional assumption that the simulation domain is large enough to make the surface contributions to  $E_{\text{self}}$  lower order. Using the same procedure, we can obtain the complete configurational force as

$$\begin{aligned} \left. \frac{d\tilde{L}(\psi_\epsilon(\mathbf{x}))}{d\epsilon} \right|_{\epsilon=0} &= \int_{\Omega} \tilde{L} \frac{\partial\Gamma_j(\mathbf{x})}{\partial x_j} d\mathbf{x} - \int_{\Omega} \left\{ \left( \frac{\partial\tilde{L}}{\partial\nabla u} \right)_j \frac{\partial u}{\partial x_i} + \left( \frac{\partial\tilde{L}}{\partial\nabla\phi} \right)_j \frac{\partial\phi}{\partial x_i} \right. \\ &\quad + \sum_{I=1}^M \left( \frac{\partial\tilde{L}}{\partial\nabla\nu_I} \right)_j \frac{\partial\nu_I}{\partial x_i} + \sum_{J=1}^m \left( \frac{\partial\tilde{L}}{\partial\nabla\omega^{\alpha_J}} \right)_j \frac{\partial\omega^{\alpha_J}}{\partial x_i} \\ &\quad + \left. \sum_{J=1}^m \left( \frac{\partial\tilde{L}}{\partial\nabla\omega^{\beta_J}} \right)_j \frac{\partial\omega^{\beta_J}}{\partial x_i} \right\} \frac{\partial\Gamma_i(\mathbf{x})}{\partial x_j} d\mathbf{x} \\ &\quad + \sum_I \left[ \int u^2(\mathbf{x}) \frac{\partial v_{\text{net}}^I(\mathbf{x}, \mathbf{R})}{\partial x_j} \Gamma_j(\mathbf{x}) d\mathbf{x} + \int u^2(\mathbf{x}) \frac{\partial v_{\text{net}}^I(\mathbf{x}, \mathbf{R})}{\partial x_j} \Gamma_j(\mathbf{r}^I) d\mathbf{x} \right] \end{aligned} \quad (3.43)$$

where  $\tilde{L}$  is from equation (3.30) modified by the relation  $\nabla \cdot \mathbf{\Gamma} = 0$ , if  $b \neq 0$  and  $v_{\text{net}}^I = v_{\text{ext}}^I - \nu_I$ . The main advantages in using the Eshelby form of forces is that this

unified expression accounts for change in volume of the crystal and can hence capture the state of stress in a crystal. It will be zero only when the crystal is in equilibrium and under no externally applied stress.

### 3.4 Summary

In summary, we have developed a local formulation for Orbital Free DFT functional. We convert the non-local electrostatic and kinetic energy functionals into a local form through the introduction of auxiliary potential fields. In deriving a local formulation for the electrostatic interactions, we use the fact that the kernel of the electrostatic interactions  $\frac{1}{|\mathbf{r}-\mathbf{r}'|}$ , is the Green's function of the Laplace operator. The kernel for the WGC component of the kinetic energy has a very complicated form and is known only in Fourier space. The local form for the non-local functional is obtained by fitting the kernel using rational polynomials, which are Green's functions of the Helmholtz operator. The problem of obtaining ground state electron density for a fixed position of atoms is then posed as a min-max problem of a local functional. We then proceed to consider the case of driving the system to equilibrium by deriving the expressions for Born-Oppenheimer forces experienced by the atoms. We first derive the Hellman-Feynman expression for the force and establish that the situations in which it is applicable are restricted in number. We resolve this by deriving an Eshelbian form for these forces by taking outer variations of the energy functional. The resulting expression is very general in terms of its applicability to different systems.



## CHAPTER IV

### Real space finite-element implementation

An increasingly popular approach for Density Functional Theory calculations has involved use of real-space formulations. Among real space techniques, finite-element methods display a number of features that make its application for electronic structure calculations very attractive. Firstly, it is a general basis set allowing for arbitrary choice of boundary conditions and thus providing a clean solution for a wide variety of physical problems. Secondly, it allows for tailoring of mesh resolution to the physics of the problem, thus allowing development of quasi-continuum methods for coarse graining. Thirdly, complex geometries – a consequence of the elastic fields created by defects – are handled with ease. Lastly, finite-element methods scale very well in large computing platforms. While being attractive on the above counts, finite-element methods suffer from the drawback of requiring a large number of degrees of freedom per atom (often orders more than Fourier space methods). Thus the computational cost of this basis set has been far in excess of the advantage provided by an increase in versatility. In this chapter, we first provide the discrete form for the equations derived in chapter III. We use known far-field solutions of Orbital Free DFT to derive optimal coarse graining rates and then explore the use of higher-order finite-elements. Having established the computational efficiency afforded by higher-order adaptive finite-elements, we proceed to compute bulk properties of a

number of Aluminum-Magnesium alloys and compare them against Kohn-Sham DFT calculations. The close match between these calculations confirms validity of using Orbital Free DFT for electronic structure calculations in Aluminum and Magnesium systems.

## 4.1 Discrete Problem

The discrete problem corresponding to equation (3.28) is given by the following constrained saddle-point problem:

$$\begin{aligned} & \inf_{u_h \in X_h^u} \sup_{\phi_h \in X_h^\phi} \inf_{\nu_h \in X_h^\nu} \inf_{\tilde{\omega}_h^\alpha \in X_h^\omega} \sup_{\tilde{\omega}_h^\beta \in X_h^\omega} \tilde{L}_h(u_h, \phi_h, \tilde{\omega}_h^\alpha, \tilde{\omega}_h^\beta, \mathbf{R}) \\ & \text{subject to: } \int_{\Omega} u_h^2 d\mathbf{x} = N. \end{aligned} \tag{4.1}$$

where  $X_h^u$ ,  $X_h^\phi$ ,  $X_h^\omega$ ,  $X_h^\nu$  denote the finite-dimensional subspaces of  $\mathcal{X}$ ,  $\mathcal{Y}$ ,  $\mathcal{Z}$  and  $\mathcal{V}$  respectively (c.f. eq (3.28)). Here, the nuclear charges are treated as point charges located on the nodes of the finite-element triangulation, and the discretization provides a regularization for the electrostatic potential. We note that the self-energy of the nucle is mesh-dependent and diverges with mesh refinement. The self energy is also computed on the same mesh that is used to compute the total electrostatic potential, which ensures that the divergent components of the variational problem on the right hand side of equation (3.20) and the self energy exactly cancel owing to the linearity of the Poisson equation (c.f. Appendix A.2).

With the discrete problem for a fixed set of atomic positions in hand, we turn to atomic relaxations and obtain the Eshelbian gradient on a finite setting by discretizing equation (3.43): Let the space be discretized with  $m$  nodes and let  $M$  of these nodes

contain nuclei. The discretized form of  $\Gamma_j(\mathbf{x})$  is

$$\Gamma_j(\mathbf{x}) = \Gamma_j^k N^k(\mathbf{x}), \quad (4.2)$$

where  $N^k(\mathbf{x})$  is the real space shape function of node  $k$  and  $\Gamma_j^k$  is the perturbation of node  $k$  in the  $j^{\text{th}}$  direction. We obtain the configurational force at node  $i$  of the discretization by setting  $\Gamma_j^i = 1$  and 0 otherwise in equation (3.43). We use the Lagrangian from equation (3.30) and note that the physical force is the negative of the Eshelbian gradient to obtain

$$\begin{aligned} -f_j^i = & \int_{\Omega} \left( \sum_{J=1}^m \left[ \frac{1}{A_J B_J} \nabla \omega^{\alpha_J} \cdot \nabla \omega^{\beta_J} + \frac{1}{A_J} \omega^{\alpha_J} \omega^{\beta_J} + \omega^{\beta_J} u^{2\alpha} + \omega^{\alpha_J} u^{2\beta} + A_J u^{2(\alpha+\beta)} \right] \right. \\ & + C_F u_h^{10/3}(\mathbf{x}) + \frac{1}{2} |\nabla u_h(\mathbf{x})|^2 + e_{xc}(u_h(\mathbf{x})) u_h(\mathbf{x})^2 + u_h(\mathbf{x})^2 \phi(\mathbf{x}) \\ & - \frac{1}{8\pi} |\nabla \phi_h(\mathbf{x})|^2 + \sum_I \frac{1}{8\pi(\mathbf{x})} |\nabla v_h^I(\mathbf{x})|^2 + \sum_I u_h^2(\mathbf{x}) v_{net}^I(\mathbf{x}) + \mu u_h^2(\mathbf{x}) \left. \right) \delta_{jk} \frac{\partial N^i(\mathbf{x})}{\partial x_k} d\mathbf{x} \\ & \int_{\Omega} - \left( \frac{\partial u_h(\mathbf{x})}{\partial x_j} \frac{\partial u_h(\mathbf{x})}{\partial x_k} + \frac{1}{4\pi} \frac{\partial \phi_h(\mathbf{x})}{\partial x_j} \frac{\partial \phi_h(\mathbf{x})}{\partial x_k} - \sum_I \frac{1}{4\pi} \frac{\partial v_h^I(\mathbf{x})}{\partial x_j} \frac{\partial v_h^I(\mathbf{x})}{\partial x_k} \right. \\ & + \sum_{J=1}^m \left( \frac{\partial \omega_h^{\alpha_J}(\mathbf{x})}{\partial x_j} \frac{\partial \omega_h^{\beta_J}(\mathbf{x})}{\partial x_k} + \frac{\partial \omega_h^{\beta_J}(\mathbf{x})}{\partial x_j} \frac{\partial \omega_h^{\alpha_J}(\mathbf{x})}{\partial x_k} \right) \left. \right) \frac{\partial N^i(\mathbf{x})}{\partial x_k} d\mathbf{x} \\ & + \int_{\Omega} \left( \sum_I u_h^2(\mathbf{x}) \frac{\partial v_{net}^I(\mathbf{x})}{\partial x_j} N^i + u_h^2(\mathbf{x}) \frac{\partial v_{net}^K(\mathbf{x})}{\partial x_j} \delta_{iK} \right) d\mathbf{x}, \quad (4.3) \end{aligned}$$

where  $\mu$  is the Lagrange multiplier enforcing the constraint. We also note that the last term is non-trivial only when the node contains a nucleus.

## 4.2 Atomic Relaxation

Since nuclei are located on the nodes of the triangulation, such nodes are made to advect along with the nuclei during atomic relaxation. We advect a ball of nodes around every nucleus to make the mesh advection robust. The displacements of these

nodes are kinematically constrained to the nucleus through mesh-less shape functions. Let the displacements of the  $m$  (in general) nodes be described by  $M$  control points and interpolation functions of the form  $\Phi(|\mathbf{X}^i - \mathbf{X}^r|)$ ,  $i \in m, r \in M$ . The displacement of any node  $k$  under this kinematic constraint is given by

$$\sum_{i=1}^R \mathbf{c}^i \Phi(|\mathbf{X}_k - \mathbf{X}_i|) \quad k = 1 : M, \quad (4.4)$$

where  $\mathbf{c}^i$  are constants to be determined. Here  $\mathbf{X}$ ,  $\mathbf{x}$  denote reference and current coordinates respectively. With these kinematic constraint the energy depends on the variables  $\mathbf{c}^i$  as

$$\tilde{L}_h = \tilde{L}_h(\mathbf{c}^1, \dots, \mathbf{c}^R). \quad (4.5)$$

The generalized forces with respect to these undetermined constants  $\frac{\partial \tilde{L}_h}{\partial \mathbf{c}^k}$ ,  $k \in R$  are given by

$$\begin{aligned} \frac{\partial \tilde{L}_h}{\partial \mathbf{c}^k} &= \sum_{i=1}^M \frac{\partial \tilde{L}_h}{\partial \mathbf{x}^i} \frac{\partial \mathbf{x}^i}{\partial \mathbf{c}^k} \quad k \in R \\ &= \sum_{i=1}^M \frac{\partial \tilde{L}_h}{\partial \mathbf{x}^i} \Phi(|\mathbf{X}^i - \mathbf{X}^k|), \end{aligned} \quad (4.6)$$

where  $\frac{\partial \tilde{L}_h}{\partial \mathbf{x}^i}$  comes from equation (4.3). We refer to the force in equation (4.6) is called as the *generalized configurational force* and drive them to zero to obtain the equilibrium configuration. In equation (4.6), we assign to  $\Phi$  a Gaussian ( $e^{-r^2}$ ) form.

### 4.2.1 Constraints on Atomic Positions

Constraints on atomic positions during relaxation are enforced with Lagrange multipliers<sup>1</sup>. With constraints, the Lagrangian in equation (4.5), is modified by the introduction of a Lagrange multiplier  $\lambda_k^i$ ,  $i = 1 : R, k = 1 : 3$  for each degree of

---

<sup>1</sup>Since mesh-less shape functions overlap with each other, constraints are enforced in a general manner

freedom, to get

$$\tilde{L}_h = \tilde{L}_h(\mathbf{c}^1, \dots, \mathbf{c}^R) + \sum_{i=1}^R \sum_{k=1}^3 \lambda_k^i u_k^i. \quad (4.7)$$

We note that  $\lambda_k^i$  is 0 for any unconstrained degree of freedom ( $c_k^i$ ). The final force expression is then given by

$$\frac{\partial \tilde{L}_h}{\partial c_k^i} = \sum_{j=1}^M \frac{\partial \tilde{L}_h}{\partial \mathbf{x}_k^j} \Phi(|\mathbf{X}_i - \mathbf{X}_j|) + \sum_{m=1}^R \lambda_k^m \Phi(|\mathbf{X}_i - \mathbf{X}_m|) \quad (4.8)$$

and the equilibrium atomic configuration is obtained by solving for

$$\frac{\partial \tilde{L}_h}{\partial c_k^i} = 0 \quad i = 1 : R, k = 1 : 3, \quad (4.9)$$

$$\frac{\partial \tilde{L}_h}{\partial \lambda_k^i} = u_k^i \quad i = 1 : R, k = 1 : 3. \quad (4.10)$$

#### 4.2.2 Cell Relaxation

For periodic problems on a bulk crystal, relaxation of the cell shape is performed by application of deformations that change volume of the cell while preserving the periodicity of its faces. To satisfy this, the applied deformation must be affine <sup>2</sup>.

$$\begin{aligned} \frac{\partial \Gamma_i}{\partial x_j} &= c_{ij} = \text{const} \\ \therefore \Gamma_i &= \frac{\partial \Gamma_i}{\partial x_j} x_j \end{aligned} \quad (4.11)$$

in equation (3.43) to get

$$\left. \frac{d\tilde{L}_h}{d\epsilon} \right|_{\epsilon=0} = \frac{\partial \Gamma_i}{\partial x_j} \int_{\Omega} \tilde{L}_{ij}(\mathbf{x}) d\mathbf{x} \quad (4.12)$$

---

<sup>2</sup>An affine deformation is the only general deformation that preserves the periodicity of faces the cell.  $\therefore$  deformation gradient must be a constant over the volume of the cell.

We draw an analogy with the principle of virtual work and relate  $\left. \frac{d\tilde{L}_h}{d\epsilon} \right|_{\epsilon=0}$  to work or change in energy,  $\int_{\Omega} \tilde{L}_{ij}(\mathbf{x}) d\mathbf{x}$  to stress and  $\frac{\partial \Gamma_i}{\partial x_j}$  as its conjugate. The crystal is then at equilibrium when the force in each atom is zero and  $\int_{\Omega} L_{ij}(\mathbf{x}) d\mathbf{x} = 0$ . To drive this stress to a desired value, we use a simple gradient-flow algorithm, i.e we drive the strain in a direction opposite to the stress until the stress reaches the desired value.

**Algorithm:**

1. evaluate stress tensor  $\sigma_{ij} = \int_{\Omega} L_{ij}(\mathbf{x}) d\mathbf{x}$
2. break if  $\sigma_{ij}\sigma_{ij} < \text{tol}$
3. Evolution : deformationGradient =  $F_{ij} = F_{ij} - \epsilon * \sigma_{ij}$  (Note:  $F_{ij} = \delta_{ij} + \frac{\partial \Gamma_i}{\partial x_j}$ ,  $\epsilon = \text{const}$ ,  $\epsilon \ll 1$ )
4. Update cell volume : newLatticeVector = oldLatticeVector\*deformationGradient

In Orbital Free DFT problems involving vacuum, it is computationally advantageous to coarsen the mesh in the vacuum, away from the atoms. Since the choice of ad-hoc rates of coarse-graining can adversely affect the accuracy of the solution, we derive the optimal coarse-graining rates for the finite-element meshes using the asymptotic nature of the solution fields in the Orbital Free DFT problem.

### 4.3 *A priori* mesh adaption

Based on the ideas presented in *Radovitzky and Ortiz (1999)*; *Levine and Wilkins (1989)*, we propose an *a priori* mesh adaption scheme by minimizing the error in the finite-element approximation of the orbital-free DFT problem for a fixed number of elements in the mesh. To this end, we first seek a bound on the energy error  $|L - L_h|$  as a function of the characteristic mesh-size,  $h$ , and the distribution of electronic fields. We remark that error estimates have been rigorously derived in recent studies for the orbital-free DFT problem ( *Langwallner et al. (2010)*; *Chen et al. (2010)*; *Cancès*

*et al.* (2010)). However, the form of these estimates is not useful for developing mesh adaption schemes as these studies primarily focused on proving the convergence of the finite-element approximation and determining the convergence rates. In what follows, we present the derivation of error bound in terms of the root-electron-density and the electrostatic potential for the Orbital Free DFT problem without kernel energies. Similar error estimates for Orbital Free DFT models with kernel energies are discussed in appendix A.1.

### 4.3.1 Estimate of Energy Error

Let  $(\bar{u}_h, \bar{\phi}_h, \bar{\mu}_h)$  and  $(\bar{u}, \bar{\phi}, \bar{\mu})$  be the solutions of the discrete finite-element problem and the continuous problem respectively for a given set of nuclear positions, where the nuclear charges are represented by a bounded regularized charge distribution  $b(\mathbf{x})$ . The ground state energy in the discrete and the continuous formulations can be expressed as

$$L_h(\bar{u}_h, \bar{\phi}_h) = \frac{1}{2} \int_{\Omega} |\nabla \bar{u}_h|^2 d\mathbf{x} + \int_{\Omega} F(\bar{u}_h) d\mathbf{x} - \frac{1}{8\pi} \int_{\Omega} |\nabla \bar{\phi}_h|^2 d\mathbf{x} + \int_{\Omega} (\bar{u}_h^2 + b) \bar{\phi}_h d\mathbf{x},$$

$$L(\bar{u}, \bar{\phi}) = \frac{1}{2} \int_{\Omega} |\nabla \bar{u}|^2 d\mathbf{x} + \int_{\Omega} F(\bar{u}) d\mathbf{x} - \frac{1}{8\pi} \int_{\Omega} |\nabla \bar{\phi}|^2 d\mathbf{x} + \int_{\Omega} (\bar{u}^2 + b) \bar{\phi} d\mathbf{x},$$

where

$$F(u) = C_F u^{10/3} + \varepsilon_{xc}(u^2)u^2 + \sum_I u^2 v_{net}^I.$$

**Proposition IV.1.** *In the neighborhood of  $(\bar{u}, \bar{\phi}, \bar{\mu})$ , the finite-element approximation error in the ground state energy can be bounded as:*

$$\begin{aligned}
|L_h - L| \leq & \frac{1}{2} \left| \int_{\Omega} |\nabla \delta u|^2 d\mathbf{x} \right| + \bar{\mu} \left| \int_{\Omega} (\delta u)^2 d\mathbf{x} \right| + \frac{1}{2} \left| \int_{\Omega} F''(\bar{u})(\delta u)^2 d\mathbf{x} \right| \\
& + \frac{1}{8\pi} \left| \int_{\Omega} |\nabla \delta \phi|^2 d\mathbf{x} \right| + \left| \int_{\Omega} (\delta u)^2 \bar{\phi} d\mathbf{x} \right| + 2 \left| \int_{\Omega} \bar{u} \delta u \delta \phi d\mathbf{x} \right|.
\end{aligned} \tag{4.13}$$

*Proof.* We begin by expanding  $L_h(\bar{u}_h, \bar{\phi}_h)$  about the solution of the continuous problem, i.e  $\bar{u}_h = \bar{u} + \delta u$  and  $\bar{\phi}_h = \bar{\phi} + \delta \phi$ . Using Taylor series expansion, we get

$$\begin{aligned}
L_h(\bar{u} + \delta u, \bar{\phi} + \delta \phi) = & \frac{1}{2} \int_{\Omega} |\nabla(\bar{u} + \delta u)|^2 d\mathbf{x} + \int_{\Omega} F(\bar{u} + \delta u) d\mathbf{x} \\
& - \frac{1}{8\pi} \int_{\Omega} |\nabla(\bar{\phi} + \delta \phi)|^2 d\mathbf{x} + \int_{\Omega} ((\bar{u} + \delta u)^2 + b) (\bar{\phi} + \delta \phi) d\mathbf{x},
\end{aligned} \tag{4.14}$$

which can be simplified to

$$\begin{aligned}
L_h(\bar{u}_h, \bar{\phi}_h) = & \frac{1}{2} \int_{\Omega} (|\nabla \bar{u}|^2 + |\nabla \delta u|^2 + 2\nabla \bar{u} \cdot \nabla \delta u) d\mathbf{x} + \int_{\Omega} F(\bar{u}) d\mathbf{x} + \int_{\Omega} F'(\bar{u})\delta u d\mathbf{x} \\
& + \frac{1}{2} \int_{\Omega} F''(\bar{u})(\delta u)^2 d\mathbf{x} - \frac{1}{8\pi} \int_{\Omega} (|\nabla \bar{\phi}|^2 + |\nabla \delta \phi|^2 + 2\nabla \bar{\phi} \cdot \nabla \delta \phi) d\mathbf{x} + \int_{\Omega} (\bar{u}^2 + b)\bar{\phi} d\mathbf{x} \\
& + 2 \int_{\Omega} \bar{u} \delta u \bar{\phi} d\mathbf{x} + \int_{\Omega} (\bar{u}^2 + b)\delta \phi d\mathbf{x} + \int_{\Omega} (\delta u)^2 \bar{\phi} d\mathbf{x} + 2 \int_{\Omega} \bar{u} \delta u \delta \phi d\mathbf{x} \\
& + O(\delta u^3, \delta \phi^3, \delta u^2 \delta \phi, \delta u \delta \phi^2).
\end{aligned} \tag{4.15}$$



Since  $(\bar{u}, \bar{\phi}, \bar{\mu})$  satisfy the Euler-Lagrange equations, we have

$$\int_{\Omega} \nabla \bar{u} \cdot \nabla \delta u \, d\mathbf{x} + \int_{\Omega} F'(\bar{u}) \delta u \, d\mathbf{x} + 2 \int_{\Omega} \bar{u} \delta u \bar{\phi} \, d\mathbf{x} = -2 \int_{\Omega} \bar{\mu} \bar{u} \delta u \, d\mathbf{x}, \quad (4.16a)$$

$$-\frac{1}{4\pi} \int_{\Omega} \nabla \bar{\phi} \cdot \nabla \delta \phi + \int_{\Omega} (\bar{u}^2 + b) \delta \phi = 0. \quad (4.16b)$$

Using equation (4.15) and the above Euler-Lagrange equations, we get

$$\begin{aligned} L_h - L &= \frac{1}{2} \int_{\Omega} |\nabla \delta u|^2 \, d\mathbf{x} - 2\bar{\mu} \int_{\Omega} \bar{u} \delta u \, d\mathbf{x} + \frac{1}{2} \int_{\Omega} F''(\bar{u}) (\delta u)^2 \, d\mathbf{x} \\ &\quad - \frac{1}{8\pi} \int_{\Omega} |\nabla \delta \phi|^2 \, d\mathbf{x} + \int_{\Omega} (\delta u)^2 \bar{\phi} \, d\mathbf{x} + 2 \int_{\Omega} \bar{u} \delta u \delta \phi \, d\mathbf{x} \\ &\quad + O(\delta u^3, \delta \phi^3, \delta u^2 \delta \phi, \delta u \delta \phi^2). \end{aligned} \quad (4.17)$$

Note that the constraint functional in the discrete form,

$$c(u_h) = \int_{\Omega} u_h^2 \, d\mathbf{x} - N, \quad (4.18)$$

is also expanded about the solution  $\bar{u}$ , to give

$$c(u_h) = \int_{\Omega} (\bar{u} + \delta u)^2 \, d\mathbf{x} - N = \int_{\Omega} (\bar{u}^2 + (\delta u)^2 + 2\bar{u} \delta u) \, d\mathbf{x} - N. \quad (4.19)$$

Using

$$\int_{\Omega} \bar{u}^2 \, d\mathbf{x} = N, \quad (4.20)$$

and  $c(\bar{u}_h) = 0$  we get

$$\int_{\Omega} (\delta u)^2 = -2 \int_{\Omega} \bar{u} \delta u \, d\mathbf{x}. \quad (4.21)$$

Using equations (4.17) and (4.21) we arrive at the following error bound in energy,

upon neglecting third-order terms and beyond

$$\begin{aligned}
|L_h - L| \leq & \frac{1}{2} \left| \int_{\Omega} |\nabla \delta u|^2 d\mathbf{x} \right| + \bar{\mu} \left| \int_{\Omega} (\delta u)^2 d\mathbf{x} \right| + \frac{1}{2} \left| \int_{\Omega} F''(\bar{u})(\delta u)^2 d\mathbf{x} \right| \\
& + \frac{1}{8\pi} \left| \int_{\Omega} |\nabla \delta \phi|^2 d\mathbf{x} \right| + \left| \int_{\Omega} (\delta u)^2 \bar{\phi} d\mathbf{x} \right| + 2 \left| \int_{\Omega} \bar{u} \delta u \delta \phi d\mathbf{x} \right|.
\end{aligned} \tag{4.22}$$

□

**Proposition IV.2.** *The finite-element approximation error in proposition IV.1 expressed in terms of the approximation errors in root-electron-density and electrostatic potential is given by*

$$|L_h - L| \leq C \left( \|\bar{u} - \bar{u}_h\|_{1,\Omega}^2 + \|\bar{\phi} - \bar{\phi}_h\|_{1,\Omega}^2 + \|\bar{u} - \bar{u}_h\|_{0,\Omega} \|\bar{\phi} - \bar{\phi}_h\|_{1,\Omega} \right) \tag{4.23}$$

*Proof.* We make use of the following norms:  $|\cdot|_{1,\Omega}$  represents the semi-norm in  $H^1$  space,  $\|\cdot\|_{1,\Omega}$  denotes the  $H^1$  norm,  $\|\cdot\|_{0,\Omega}$  and  $\|\cdot\|_{0,p,\Omega}$  denote the standard  $L^2$  and  $L^p$  norms respectively. All the constants to appear in the following estimates are positive and bounded. Firstly, we note that

$$\frac{1}{2} \left| \int_{\Omega} |\nabla \delta u|^2 d\mathbf{x} \right| = \frac{1}{2} \int_{\Omega} |\nabla \delta u|^2 d\mathbf{x} \leq C_1 \|\bar{u} - \bar{u}_h\|_{1,\Omega}^2, \tag{4.24}$$

$$\bar{\mu} \left| \int_{\Omega} (\delta u)^2 d\mathbf{x} \right| = \bar{\mu} \int_{\Omega} (\bar{u}_h - \bar{u})^2 d\mathbf{x} \leq C_2 \|\bar{u} - \bar{u}_h\|_{0,\Omega}^2. \tag{4.25}$$

Using Cauchy-Schwartz and Sobolev inequalities, we arrive at the following estimate

$$\begin{aligned}
\frac{1}{2} \left| \int_{\Omega} F''(\bar{u})(\delta u)^2 d\mathbf{x} \right| &\leq \frac{1}{2} \int_{\Omega} |F''(\bar{u})(\bar{u}_h - \bar{u})^2| d\mathbf{x} \\
&\leq C_3 \| F''(\bar{u}) \|_{0,\Omega} \| (\bar{u} - \bar{u}_h)^2 \|_{0,\Omega} \\
&= C_3 \| F''(\bar{u}) \|_{0,\Omega} \| \bar{u} - \bar{u}_h \|_{0,4,\Omega}^2 \\
&\leq \bar{C}_3 \| \bar{u} - \bar{u}_h \|_{1,\Omega}^2 .
\end{aligned} \tag{4.26}$$

Further, we note

$$\frac{1}{8\pi} \left| \int_{\Omega} |\nabla(\bar{\phi}_h - \bar{\phi})|^2 d\mathbf{x} \right| \leq C_4 |\bar{\phi} - \bar{\phi}_h|_{1,\Omega}^2 . \tag{4.27}$$

Using Cauchy-Schwartz and Sobolev inequalities we arrive at

$$\begin{aligned}
\left| \int_{\Omega} (\delta u)^2 \bar{\phi} d\mathbf{x} \right| &\leq \int_{\Omega} |(\bar{u}_h - \bar{u})^2 \bar{\phi}| d\mathbf{x} \leq \| \bar{\phi} \|_{0,\Omega} \| (\bar{u}_h - \bar{u})^2 \|_{0,\Omega} \\
&\leq C_5 \| \bar{u} - \bar{u}_h \|_{0,4,\Omega}^2 \\
&\leq \bar{C}_5 \| \bar{u} - \bar{u}_h \|_{1,\Omega}^2 .
\end{aligned} \tag{4.28}$$

Also note that

$$\begin{aligned}
\left| \int_{\Omega} \bar{u} \delta u \delta \phi d\mathbf{x} \right| &\leq \int_{\Omega} |\bar{u}(\bar{u}_h - \bar{u})(\bar{\phi}_h - \bar{\phi})| d\mathbf{x} \\
&\leq \| \bar{u} \|_{0,6,\Omega} \| \bar{u} - \bar{u}_h \|_{0,\Omega} \| \bar{\phi} - \bar{\phi}_h \|_{0,3,\Omega} \\
&\leq C_6 \| \bar{u} - \bar{u}_h \|_{0,\Omega} \| \bar{\phi} - \bar{\phi}_h \|_{1,\Omega} ,
\end{aligned} \tag{4.29}$$

where we made use of the generalized Hölder inequality in the first step and Sobolev

inequality in the next. Using the bounds derived above, it follows that

$$|E_h - E| \leq C \left( \| \bar{u} - \bar{u}_h \|_{1,\Omega}^2 + |\bar{\phi} - \bar{\phi}_h|_{1,\Omega}^2 + \| \bar{u} - \bar{u}_h \|_{0,\Omega} \| \bar{\phi} - \bar{\phi}_h \|_{1,\Omega} \right). \quad (4.30)$$

□

Now it remains to bound the finite-element discretization error with interpolation errors which can in turn be bounded with size of the finite-element mesh size  $h$ . This requires a careful analysis in the case of orbital-free DFT, which is a non-linear constrained problem, and has been discussed in *Langwallner et al. (2010)*. Using the results from Theorem 3.2 in *Langwallner et al. (2010)*, we bound the estimates in equation (4.30) using the following inequalities ( cf. *Ciarlet (1978)*)

$$\| \bar{u} - \bar{u}_h \|_{1,\Omega} \leq \bar{C}_0 \| \bar{u} - u_I \|_{1,\Omega} \leq \tilde{C}_0 \sum_e h_e^k |\bar{u}|_{k+1,\Omega_e}, \quad (4.31a)$$

$$\| \bar{u} - \bar{u}_h \|_{0,\Omega} \leq \bar{C}_1 \| \bar{u} - u_I \|_{0,\Omega} \leq \tilde{C}_1 \sum_e h_e^{k+1} |\bar{u}|_{k+1,\Omega_e}, \quad (4.31b)$$

$$|\bar{\phi} - \bar{\phi}_h|_{1,\Omega} \leq \bar{C}_2 |\bar{\phi} - \phi_I|_{1,\Omega} \leq \tilde{C}_2 \sum_e h_e^k |\bar{\phi}|_{k+1,\Omega_e}, \quad (4.31c)$$

where  $k$  is the order of the polynomial interpolation, and  $e$  denotes an element in the regular family of finite-elements (c.f. *Ciarlet (1978)*) with mesh-size  $h_e$  covering a domain  $\Omega_e$ . Hence, the error estimate in the energy is given by

$$|L_h - L| \leq C \sum_e \left[ h_e^{2k} |\bar{u}|_{k+1,\Omega_e}^2 + h_e^{2k} |\bar{\phi}|_{k+1,\Omega_e}^2 + h_e^{2k+1} |\bar{u}|_{k+1,\Omega_e} |\bar{\phi}|_{k+1,\Omega_e} \right]. \quad (4.32)$$

In the above equation and the analysis to follow, for simplicity, we restrict ourselves to the case where a single finite-element triangulation provides discretization for both root-electron-density and electrostatic potential. Finally, the error estimate

to  $O(h^{2k+1})$  is given by

$$|L_h - L| \leq \mathcal{C} \sum_e h_e^{2k} [|\bar{u}|_{k+1, \Omega_e}^2 + |\bar{\phi}|_{k+1, \Omega_e}^2]. \quad (4.33)$$

### 4.3.2 Optimal Coarse-Graining Rate

We now present the optimal mesh-size distribution that can be estimated by minimizing the approximation error in energy for a fixed number of elements. The approach here closely follows the treatment in *Radovitzky and Ortiz (1999)*. Using the definition of the semi-norms, we rewrite equation (4.33) as

$$|L_h - L| \leq \mathcal{C} \sum_{e=1}^{N_e} \left[ h_e^{2k} \int_{\Omega_e} \left[ |D^{k+1} \bar{u}(\mathbf{x})|^2 + |D^{k+1} \bar{\phi}(\mathbf{x})|^2 \right] d\mathbf{x} \right], \quad (4.34)$$

where  $N_e$  denotes the total number of elements in the finite-element triangulation. To obtain a continuous optimization problem rather than a discrete one, an element size distribution function  $h(\mathbf{x})$  is introduced so that the target element size is defined at all points  $\mathbf{x}$  in  $\Omega$ , and we get

$$|L_h - L| \leq \mathcal{C} \sum_{e=1}^{N_e} \int_{\Omega_e} \left[ h_e^{2k} \left[ |D^{k+1} \bar{u}(\mathbf{x})|^2 + |D^{k+1} \bar{\phi}(\mathbf{x})|^2 \right] d\mathbf{x} \right], \quad (4.35)$$

$$\leq \mathcal{C}' \int_{\Omega} h^{2k}(\mathbf{x}) \left[ |D^{k+1} \bar{u}(\mathbf{x})|^2 + |D^{k+1} \bar{\phi}(\mathbf{x})|^2 \right] d\mathbf{x}. \quad (4.36)$$

Further, the number of elements in the mesh is in the order of

$$N_e \propto \int_{\Omega} \frac{d\mathbf{x}}{h^3(\mathbf{x})}. \quad (4.37)$$

The optimal mesh size distribution is then determined by the following variational problem which minimizes the approximation error in energy subject to a fixed number

of elements:

$$\min_h \int_{\Omega} \left\{ h^{2k}(\mathbf{x}) \left[ |D^{k+1}\bar{u}(\mathbf{x})|^2 + |D^{k+1}\bar{\phi}(\mathbf{x})|^2 \right] \right\} d\mathbf{x} \quad \text{subject to : } \int_{\Omega} \frac{d\mathbf{x}}{h^3(\mathbf{x})} = N_e. \quad (4.38)$$

The Euler-Lagrange equation associated with the above problem is given by

$$2kh^{2k-1}(\mathbf{x}) \left[ |D^{k+1}\bar{u}(\mathbf{x})|^2 + |D^{k+1}\bar{\phi}(\mathbf{x})|^2 \right] - \frac{3\eta}{h^4(\mathbf{x})} = 0, \quad (4.39)$$

where  $\eta$  is the Lagrange multiplier associated with the constraint. Thus, we obtain the following distribution

$$h(\mathbf{x}) = A \left( |D^{k+1}\bar{u}(\mathbf{x})|^2 + |D^{k+1}\bar{\phi}(\mathbf{x})|^2 \right)^{-1/(2k+3)} \quad (4.40)$$

where the constant  $A$  is computed from the constraint that the total number of elements in the finite-element discretization is  $N_e$ .

The coarse-graining rate derived in equation (4.40) has been employed to construct the finite-element meshes for different kinds of problems we study in the subsequent sections.

## 4.4 Implementation and Results

Traditionally, linear tetrahedral elements have been preferred for many applications as these elements are well suited for problems requiring complicated domains and moderate levels of accuracy. However, in electronic structure calculations the levels of accuracy desired, are much higher. We explore methods to reduce the number of basis functions while keeping up the accuracy desired for the calculation. Under these conditions we find the use of higher-order finite elements very appealing and investigate whether they provide chemical level of accuracy in electronic structure calculations with greater computational efficiency than linear elements. We employ

in our study  $C^0$  basis functions comprising of tetrahedral elements with interpolating polynomials up to degree two (TET4 and TET10) and hexahedral elements up to degree four (HEX8, HEX27, HEX64, HEX125). The number following the words ‘TET’ and ‘HEX’ denote the number of nodes in the element. We also investigate the use of spectral-elements, first introduced in *Patena* (1984), and applied to electronic structure calculations in *Batcho* (2000).<sup>3</sup>

We first study the convergence rates of the finite-element approximation with decreasing mesh sizes for different polynomial orders of interpolation. The nuclear charges are treated as point charges located on the nodes of the finite-element triangulation, and the discretization provides a regularization for the electrostatic potential. We note that the self-energy of the nuclei in this case is mesh-dependent and diverges upon mesh refinement. The self energy is also computed on the same mesh that is used to compute the total electrostatic potential, which ensures that the divergent components of the variational problem on the right hand side of equation (3.20) and the self energy exactly cancel owing to the linearity of the Poisson equation.

The following procedure is adopted for conducting the convergence study: the coarsest mesh having  $N_e$  elements is constructed with a coarsening rate determined using the *a priori* knowledge of the far-field asymptotic solutions of electronic fields. We note that as far-field asymptotic solutions are used to compute the coarse-graining rates as opposed to the exact solutions, the obtained meshes are only optimal in the far-field and possibly sub-optimal near the nuclei. Nevertheless, the meshes constructed using this approach still provide an efficient way of resolving the vacuum in non-periodic calculations as opposed to using a uniform discretization or employing

---

<sup>3</sup>In conventional finite-elements, basis functions are constructed as Lagrange polynomials interpolated through equi-spaced nodes in an element, whereas, in spectral-elements, nodal positions are distributed optimally and correspond to the roots of derivatives of Chebyshev or Legendre polynomials. Such a distribution does not have nodes on the boundaries of an element. To guarantee  $C^0$  basis functions, it is common to append nodes on element boundaries. This set of nodes is commonly referred to by Gauss-Lobatto-Chebyshev or Gauss-Lobatto-Legendre. For high orders of interpolation, conventional finite-elements result in an ill-conditioned problem, whereas, spectral-elements are devoid of this deficiency (*Boyd* (2001)).

an ad-hoc coarse-graining rate. The sequence of refined meshes are subsequently constructed by a uniform subdivision of the coarse-mesh, which represents a systematic refinement of the approximation space. The finite-element ground-state energies,  $L_h$ , obtained from each of these subdivisions for the highest order element (HEX125) are used to fit an expression of the form

$$|L_0 - L_h| = \mathcal{C}(1/N_e)^{2k/3}. \quad (4.41)$$

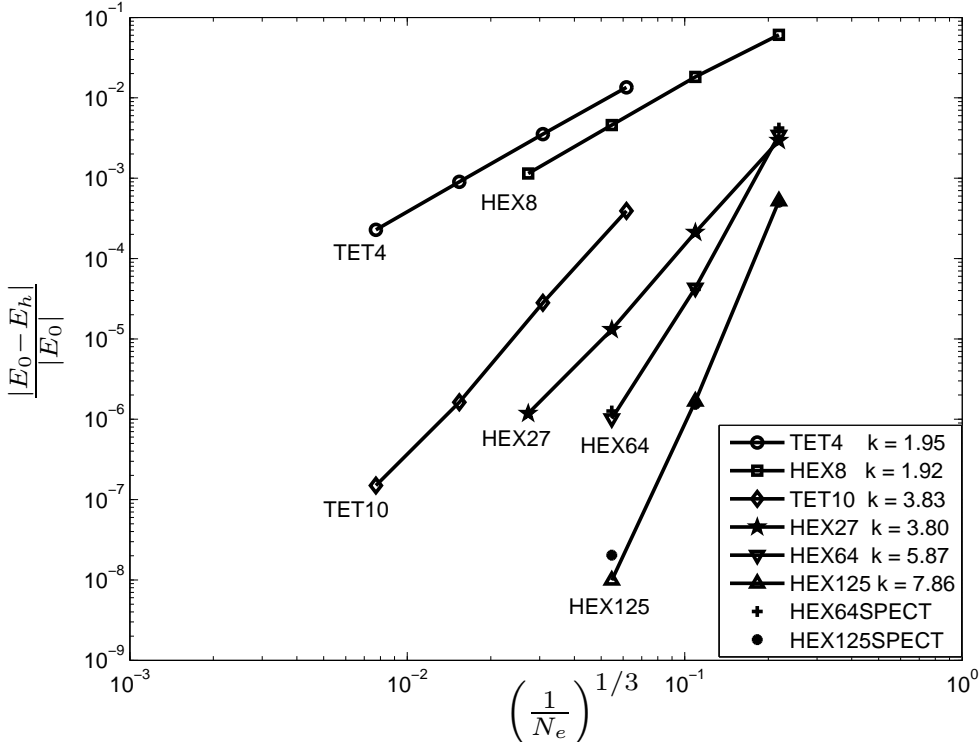
to determine the constants  $L_0$ ,  $\mathcal{C}$  and  $k$ . All convergence study plots for different orders of finite-elements in the subsequent sub-sections show the relative error  $\frac{|L_0 - L_h|}{|L_0|}$  plotted against  $(1/N_e)^{1/3}$  for the value of  $L_0$  obtained using the HEX125 element. The slopes of these curves provide the rate of convergence of the finite-element approximation error in energy for the system being studied. We display here the case of a perfect Aluminium crystal. Periodic boundary conditions are imposed on the root-electron-density and the electrostatic potential on a single face-centered cubic unit cell. Figure 4.1 shows the rate of convergence of the energy error using the density dependent WGC kernel functionals. Remarkably, it can be seen that we observe ideal rates of reduction in error. Ideal rates of convergence to the solution have been proved mathematically only for linear problems. For a strongly non-linear problem, such as in Orbital Free DFT, such a rate is not guaranteed. Our study is purely numerical and a rigorous mathematical proof for the same has only recently become available. It is evident that our chosen technique for local reformulation of the electrostatic and kernel energies has played an important role in obtaining ideal rates of convergence.

It can also be observed from the graph that higher order basis functions perform well. A vertical line through the graph shows that for a given number of elements, higher order elements are seen to be more accurate by orders of magnitude. A horizontal line through the graph shows that for a chemical level of accuracy, higher



order elements require far fewer degrees of freedom than linear elements. Hexahedral elements are also seen to perform better than tetrahedral elements of the same polynomial order.

Figure 4.1: Convergence rates for the finite-element approximation of bulk Aluminum using orbital-free DFT with DD kernel energy.



We then turn towards studying the computational efficiency afforded by the use of higher-order finite-element approximations in the Orbital Free DFT problem. As seen from the convergence studies, higher-order finite-element approximations result in a faster rate of convergence. However, the need for higher-order quadratures for numerical approximation of the integrals in the finite-element formulation increases the per element cost of computations in using higher-order elements. Further, the increase in the bandwidth of the Hessian matrix affects the performance of the iterative solvers. In order to unambiguously determine the computational efficiency of higher-order elements, we measure the CPU time taken for the simulations for a wide range

of meshes providing different relative accuracies. We provide here the results of the investigation on large problems comprising of Aluminum clusters with varying sizes. We consider Aluminum clusters containing 1x1x1, 3x3x3, 5x5x5 face-centered cubic unit cells and restrict this investigation to the study of computational efficiency of linear TET4 and quartic HEX125Spectral elements. Figure 4.2 shows the relative errors vs. the normalized CPU time for the various simulations conducted. The reference time taken here is that of a 3x3x3 aluminium cluster simulated using TET4 elements taking about 3000 CPU hours (approximately 75 hours on 40 AMD Opteron 2.6 GHz processors), with a relative error in the energy of the order  $10^{-2}$ . As can be observed from the results, quartic HEX125Spectral element is over hundred-fold more computationally efficient and provides at least an order of magnitude greater accuracy than the linear TET4 element. Further, we note that the simulation performed on a 5x5x5 aluminium cluster (666 atoms) using quartic HEX125Spectral elements takes only marginally more time than a 1x1x1 cluster (14 atoms) discretized with linear TET4 elements, while providing two orders-of-magnitude greater accuracy. Interestingly, we also observe that calculations with spectral finite-elements are twice as fast as regular finite-elements. We attribute this improved performance to the better conditioning of the system. It is known that at higher orders of interpolation, conventional finite-elements result in an ill-conditioned problem, while spectral finite-elements are devoid of this deficiency. These results confirm the computational efficiency of using higher-order elements for Orbital Free DFT calculations.

## 4.5 Transferability studies

The transferability of Orbital Free DFT to *simple* Al-Mg alloys ( $Al_3Mg$ ) was established by *Huang and Carter* (2008) with an implementation using a plane wave basis set. In our study, we establish the same for a real-space, finite-element implementation and also extend the investigations to a wider range of Al-Mg systems.

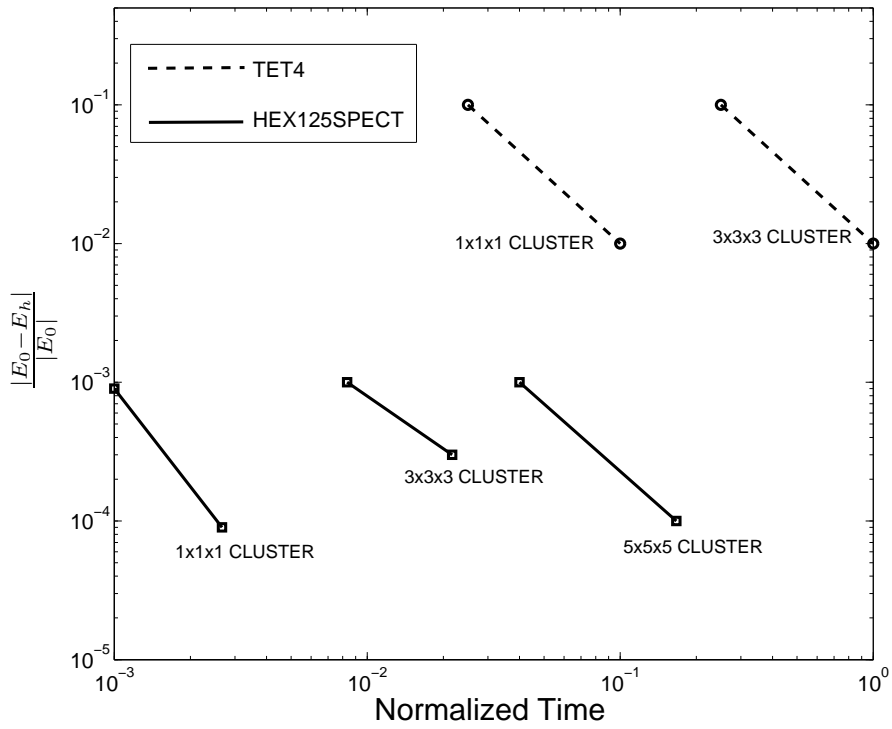


Figure 4.2: Computational efficiency of various orders of finite-element approximations. Case study: Aluminum clusters.

These systems provide a stringent test on the validity of the Orbital Free DFT kinetic energy functionals and for the real-space, finite-element implementation. The results to follow unambiguously establish that real-space finite-element implementation Orbital Free DFT with WGC kernels can provide chemical accuracies in all Aluminum-Magnesium systems. We follow *Huang and Carter* (2008) and determine the most stable phase of Aluminum and Magnesium over a wide range of competing phases including, face-centered-cubic (fcc), body-centered-cubic (bcc), simple-cubic, diamond, hexagonal-close-packed (hcp). We establish correctly that Aluminum is most stable in the fcc phase while Magnesium is the most stable in the hcp state. We then follow this with a computation of equilibrium energies of a number of Al-Mg intermetallic systems (c.f. *Jain et al.* (2011); *Ong et al.* (2011)) of increasing complexity like  $Al_3Mg$ ,  $Al_{14}Mg_{13}$ ,  $Al_{12}Mg_{17}$ ,  $Al_{23}Mg_{30}$ , and the  $\beta'$  phase with 4, 27, 29, 53, 879 atoms per unit cell respectively (the last of these, the  $\beta'$  phase is known to be the largest Al-Mg phase without significant disorder).

At the outset, we briefly mention some of the important improvements in solution schemes that are necessary for OFDFT to be a robust and viable technique for large scale calculations. Firstly, the WGC Kernels produce instabilities in the functional that has been established by *Blanc and Cancès* (2004) (though for a class of Density Independent kernels). This instability shows up in the divergence of WGC kernel energies for complex intermetallic systems. To resolve this, we follow the suggestion in *Hung et al.* (2010) and use the following Taylor expansion for the WGC kernels:

$$\begin{aligned}
K(u(\mathbf{x}), u(\mathbf{x}'); |\mathbf{x} - \mathbf{x}'|) &= K(u^*; |\mathbf{x} - \mathbf{x}'|) + \left. \frac{\partial K}{\partial u(\mathbf{x})} \right|_{u^*} \delta u(\mathbf{x}) \\
&+ \left. \frac{\partial K}{\partial u(\mathbf{x}')} \right|_{u^*} \delta u(\mathbf{x}') + \left. \frac{\partial^2 K}{\partial u(\mathbf{x}') \partial u(\mathbf{x})} \right|_{u^*} \delta u(\mathbf{x}') \delta u(\mathbf{x}) \quad (4.42)
\end{aligned}$$

This is to be compared with the full second order Taylor expansion given in equation (3.13). This reduced second order expansion is seen to be converging for all the

systems considered. Secondly, we look for a robust solution scheme to solve for the ground state electron density. We note that along with  $u, \phi$  we have a number of kernel fields  $\omega_\alpha, \omega_\beta$  whose size depends on the accuracy of the fitting form for the kernels (described in section 3.2.2). While a staggered solution scheme suggested in *Motamarri et al.* (2012), would be natural choice, we find it to be an inefficient choice for solving large systems. This apart, we find a number of shortcomings, some of which affect only real space implementations.

- The rational polynomial fits proposed by *Choly and Kaxiras* (2002) are accurate enough to capture energetics of Al and Mg in simple systems. However, for the intermetallic systems we study, the WGC kernels need to be fit with greater accuracy. In fact, even for a simple intermetallic like  $Al_3Mg$  the alloy formation energy obtained using the fit proposed in *Choly and Kaxiras* (2002) is qualitatively incorrect.
- The Helmholtz equations required to solve for potential fields coming from the local reformulation (c.f. section 3.2.2) are characterized by frequencies that are high enough to render most iterative techniques and multigrid schemes inefficient. The systems sizes we consider, preclude the usage of sparse direct solvers. Reliable techniques for solving high frequency Helmholtz equations is an open problem.
- The indefiniteness of the Helmholtz operator makes the rate of convergence of most iterative linear solvers quite slow and in such cases, usage of a staggered scheme (*Motamarri et al.* (2012)) leads to a drastic increase in solution times.

We resolve the first issue, we follow the approach of *Choly and Kaxiras* (2002) and extend the accuracy of fitting expressions. To make the Helmholtz equations amenable to iterative solvers, we find the use of Block Jacobi preconditioners with ILU (Incomplete LU) pre conditioners within the blocks to be robust for the range of frequencies

produced by local reformulation of the WGC kernels. The solvers and preconditioners are available through the PETSc library (*Balay et al. (2014)*). We also observe that the above preconditioner remains robust only for a hermitian matrix. When the Helmholtz equations are solved with real (and hence interlaced) matrices, the symmetry is lost and the preconditioners are no longer effective. We also clarify that this is only an observation and is not backed up by analysis. Finally, to make the calculations robust, we adopt a self-consistent solver scheme where the root-electron-density and electrostatic fields are minimized with a Newton technique while the kernels are solved separately, in a self-consistent loop. The choice of a mixing scheme is crucial and we find that the Anderson N-stage mixing scheme (c.f *Anderson (1965)*) is sufficient to provide a self consistent solution in under 10 steps. For Newton based minimization of the root-electron-density and the electrostatic potential, we choose a monolithic/concurrent scheme over a staggered scheme even though is more unstable (*Motamarri et al. (2012)*). This is because the introduction of kernels greatly affects the convexity of the functional and degrades non-linear solver performance. When using a staggered scheme, the use of a matrix-free Newton technique is necessary to keep the dependent fields (electrostatic and kernel) consistent with the root-electron-density. Since matrix-free schemes work without an explicit Hessian matrix (instead evaluating matrix-vector products through numerical directional derivatives) only simple preconditioners like Jacobi and its variants can be used. The inclusion of a number of kernel fields into the functional adversely affects the conditioning of the matrix, making Jacobi preconditioning techniques insufficient. Thus we use a monolithic/concurrent scheme and use the Field Split preconditioner available through PETSc (*Balay et al. (2014)*), that allows the use of different preconditioners for the root-electron density and electrostatic potential and proves to be very robust. The charge constraint is enforced through Lagrange multipliers.

The transferability studies are conducted by performing Orbital Free DFT calcu-

lations with WGC kernels and the Bulk Local pseudopotential (BLPS) (c.f. *Huang and Carter* (2008)) and Kohn Sham DFT calculations with Troullier-Martins Norm-Conserving non-local pseudopotential (TM-NLPS). For the phase stability studies, we compare the differences in the equilibrium total energy of each phase with the most stable phase, whereas in the transferability studies we compute the alloy formation energies. The  $\beta'$  alloy has a disorder in 20 out of 879 sites with each site having 0.5 chance of being occupied by either Al or Mg. In our simulations, we treat two limits where all 20 sites are occupied by either Al or Mg and call them  $\beta'$ (Al) and  $\beta'$ (Mg) respectively. For these two systems, we do not provide Kohn-Sham DFT results as they are computationally prohibitive. The results of the phase stability study are shown in table 4.1 and those for the intermetallic systems in table 4.2. We can readily observe that the qualitative trends are consistent with Kohn-Sham DFT calculations. Moreover, with the choice of WGC kernels truncated to a reduced second order, all energy differences between the Orbital Free DFT and Kohn-Sham DFT results are less than 65 meV which is within the error made by other approximations in Kohn-Sham DFT (e.g. the choice of exchange-correlation functional or choice of pseudopotential). These studies validate the transferability of Orbital Free DFT to Al-Mg systems.

Table 4.1: KS-DFT-LDA results for equilibrium total energies ( $E_{min}$  in eV per atom) calculated using TM-NLPS, and OFDFT results for the same using BLPS (*Huang and Carter* (2008)). The energy differences in eV between competing phases and the stable phase are shown. The TM-NLPS data should be viewed as the benchmark. The zero in the first column is to indicate that these numbers form the base against which energies of other phases are determined.

Al	fcc	hcp	bcc	sc	dia
OFDFT	0	0.016	0.075	0.339	0.843
KSDFT	0	0.040	0.106	0.397	0.820
Mg	hcp	fcc	bcc	sc	dia
OFDFT	0	0.003	0.019	0.343	0.847
KSDFT	0	0.014	0.031	0.400	0.821

Table 4.2: KS-DFT-LDA results for formation energies ( $E_{min}$  in eV per atom) calculated using TM-NLPS, and OFDFT results for the same using BLPS (*Huang and Carter* (2008)). The TM-NLPS data should be viewed as the benchmark

Alloy	$Al_3Mg$	$Al_{14}Mg_{13}$	$Al_{12}Mg_{17}$	$Al_{30}Mg_{23}$	$\beta'$ (Al)	$\beta'$ (Mg)
OFDFT	-0.013	0.069	-0.007	-0.001	-0.026	-0.084
KSDFT	-0.009	0.062	-0.020	-0.016	NA	NA



## CHAPTER V

### Quasi Continuum - Orbital Free DFT

Mechanical properties and chemical properties of crystalline materials are strongly affected by defects in the structure and even the simplest defects create profound effects on the material. These defects occur over multiple length scales ranging from the angstrom (vacancies) to the micro-scale (precipitates). The lattice distortion that a defect creates is characterized by a core region, with rapidly varying fields and an elastic tail that with slowly varying but long ranged fields. The core region of a defect features sharp changes in the atomic displacement field and in the electron density distribution. This necessitates calculations of quantum mechanical accuracy and correspondingly, knowledge of the electronic structure. The far-field perturbations induced by the core are long ranged, thus placing the demand for large simulations. The twin demands of highly accurate physical models and large scale simulations make this problem computationally challenging. Traditionally, continuum models based on elasticity have been very successful in predicting the asymptotic decay of displacement fields outside the defect core. More recently, large scale atomistic calculations using empirical potentials to describe atomic interactions have been used to predict the complete displacement field, including the core region. However, neither approach can capture physics coming from changes to the electronic structure —sharp disturbances at the core and long ranged decay, created by the defect. Since the per-

turbations to the electronic structure are long ranged, typically, volumes containing million of atoms need to be simulated, before the perturbations decay sufficiently. Explicit electronic structure simulations on such large samples are computationally intractable. On the other hand, the challenges presented by the problem can be addressed by multi-scale models that provide electronic structure resolution near the defect core and seamlessly coarsen to a continuum description away from the core and making substantial computational savings in the process. We build upon the field theoretic quasi-continuum formulation introduced in chapter II and extend it from interatomic potentials to Orbital Free DFT. This gives us the capability to perform electronic structure calculations without restrictions on cell size. The formulation follows chapter II closely.

## 5.1 Quasi-continuum Orbital Free DFT

We introduce three meshes representing 1) atomic positions ( $T_{h1}$ ) 2) A mesh to capture corrections to electronic and potential fields ( $T_{h3}$ ) 3) A subatomic mesh that captures fine scale oscillations in the electronic and potential fields ( $T_{h2}$ ). We restrict the meshes in such a way that  $T_{h3}$  is a p-refinement of  $T_{h1}$  and  $T_{h2}$  is a sub-division and a p-refinement of  $T_{h3}$ . We use linear hexahedral (HEX8) elements for  $T_{h1}$ , quadratic hexahedrons (HEX27) for  $T_{h3}$  and cubic hexahedrons (HEX64) for  $T_{h2}$ . The  $T_{h2}$  mesh extends only to a small fraction of the domain size, beyond which a unit cell is associated with each  $T_{h3}$  element. Thus the  $T_{h2}$  mesh consists of a continuous region and a number of disjoint unit cells. (c.f. Figure 2.8). We additionally denote by  $X_{h1}$ ,  $X_{h2}$  and  $X_{h3}$  the corresponding finite-element approximation spaces and denote by

$\tilde{\omega} = \{\tilde{\omega}^\alpha, \tilde{\omega}^\beta\}$ , the list containing all kernel fields. We decompose the fields as

$$u_h = u_h^0 + u_h^c, \quad \phi_h = \phi_h^0 + \phi_h^c \quad (5.1a)$$

$$\tilde{\omega}_h = \tilde{\omega}_h^0 + \tilde{\omega}_h^c, \quad \mu_h = \mu_h^0 + \mu_h^c \quad (5.1b)$$

where  $u_h^0, \phi_h^0, \tilde{\omega}_h^0, \mu_h^0 \in X_{h2}$  are the predictors while  $u_h^c, \phi_h^c, \tilde{\omega}_h^c, \mu_h^c \in X_{h3}$  are their correctors.  $\mu$  is the Lagrange multiplier enforcing the charge constraint. Note that self potentials  $\nu$  correct only for the singularities in  $\phi$  (present only in  $\phi^0$ ) and need to be evaluated only in  $T_{h2}$  and have no corrections associated with them. The minimization problem given by equation (4.1) now reduces to a minimization problem on the corrector fields and is given by

$$\begin{aligned} & \inf_{u_h^c \in X_{h3}} \sup_{\phi_h^c \in X_{h3}} \inf_{\tilde{\omega}_h^{\alpha,c} \in X_{h3}} \sup_{\tilde{\omega}_h^{\beta,c} \in X_{h3}} \tilde{L}(u_h^0 + u_h^c, \phi_h^0 + \phi_h^c, \tilde{\omega}_h^{\alpha,0} + \tilde{\omega}_h^{\alpha,c}, \tilde{\omega}_h^{\beta,0} + \tilde{\omega}_h^{\beta,c}, \mathbf{R}) \\ & \text{subject to: } \int_{\Omega} (u_h^0 + u_h^c)^2 d\mathbf{x} = N. \end{aligned} \quad (5.2)$$

We solve for the predictor fields ( $u_0, \phi_0$  etc) under the Cauchy-Born approximation where the values of electronic fields on the fine mesh are computed from periodic unit-cells undergoing the deformations seen by their associated  $T_{h1}$  element. We proceed with an explicit solve on the contiguous region of the  $T_{h2}$  mesh. Since this volume is only a small fraction of the complete system volume, the costs are tractable. In this solve, naturally, the only numerical approximation involved is the bulk boundary condition for the  $T_{h2}$  mesh (which is only approximate due to the small size of the computation). These errors are removed in the solution for the corrector fields. Since the explicit solve captures the electronic structure at the defect core to a reasonable accuracy, the corrector fields are primarily required to capture the long ranged asymptotic decay of the core-effect. This allows for the corrector fields to be represented on

a very coarse mesh everywhere. In the solution to the variational problem (5.2), we are naturally required to calculate generalized forces for variations with respect to  $\phi_h^c$  (correction to electrostatic potential),  $u_h^c$  (correction to electron-density),  $\tilde{\omega}_h^c$  (correction to kernel potentials) and  $\mu_h^c$  (correction to the Lagrange multiplier). The generalized forces – defined here as  $f_u^k, f_\phi^k, f_{\tilde{\omega}}^k, f_\mu^k$  for  $k^{\text{th}}$  node of the  $T_{h3}$  mesh depend on the values of the predictors that are quantities defined on the finer mesh  $T_{h2}$ . Since the predictors are defined only on the fine mesh, the corrector fields are interpolated to the  $T_{h2}$  mesh, where the nodal forces are evaluate and restricted back to the  $T_{h3}$  mesh. Since the  $T_{h2}$  mesh is a sub-grid of  $T_{h3}$ , the interpolation of the fields and restriction of the forces have no projection error. We provide an expression for  $f_u^k$  and others follow similarly. By definition,

$$f_u^k = \int_{\Omega} \frac{\partial \tilde{L}}{\partial u_h(\mathbf{x})} N_{h3}^k(\mathbf{x}) d\mathbf{x} + \int_{\Omega} \frac{\partial \tilde{L}}{\partial \nabla u_h(\mathbf{x})} \nabla N_{h3}^k(\mathbf{x}) b\mathbf{x} + \int_{\Omega} 2\mu_h u_h(\mathbf{x}) N_{h3}^k(\mathbf{x}) d\mathbf{x}, \quad (5.3)$$

where

$$N_{h3}^k(\mathbf{x}) = \sum_{a \in T_{h2}} N_{h3}^k(\mathbf{x}_a) N_{h2}^a(\mathbf{x}). \quad (5.4)$$

Here,  $a$  denotes a node in  $T_{h2}$ , located at  $\mathbf{x}_a$  and  $N_{h2}^a$  the shape function associated with node  $a$ . Hence the nodal force in equation (5.3) is given as

$$f_u^k = \sum_{a \in T_{h2}} N_{h3}^k(\mathbf{x}_a) \left\{ \int_{\Omega} \frac{\partial \tilde{L}}{\partial u_h(\mathbf{x})} N_{h2}^a(\mathbf{x}) d\mathbf{x} + \int_{\Omega} \frac{\partial \tilde{L}}{\partial \nabla u_h(\mathbf{x})} \nabla N_{h2}^a(\mathbf{x}) d\mathbf{x} + \int_{\Omega} 2\mu_h u_h(\mathbf{x}) N_{h2}^a(\mathbf{x}) d\mathbf{x} \right\} \quad (5.5)$$

$$= \sum_{a \in T_{h2}} N_{h3}^k(\mathbf{x}_a) f_u^{a,0} \quad (5.6)$$

where  $f_u^{a,0}$  denoted the generalized force associated with  $u_h$  on node  $a$  of mesh  $T_{h2}$ .

The complexity of this force evaluation is reduced by introducing cluster rules as

described in equation (2.69) to obtain

$$f_u^k = \sum_{e \in T_{h3}} C_e \sum'_{a \in D_e} N_{h3}^k(\mathbf{x}_a) f_u^{a,0}, \quad k \in T_{h3} \quad (5.7)$$

where  $f_u^{a,0}$  is the nodal force associated with  $u_h$  on node  $a$  of the  $T_{h2}$  mesh;  $C_e$  is a constant whose value is 1 if  $D_e = e$  and  $\frac{|e|}{|D_e|}$  otherwise;  $'$  over summation avoids double counting;  $N_{h3}^k(\mathbf{x}_a)$  denotes the value of the shape function associated with node  $k$  of  $T_{h3}$  at position  $\mathbf{x}_a$ . The generalized forces for other variables can be derived similarly.

To end, we derive expressions for the configurational force on the nuclei in the  $T_{h1}$  mesh. These forces have already been derived on a continuous setting in equation (3.43). To get these forces on a discrete setting, for a node  $k$  of the  $T_{h1}$  mesh, we replace  $\Gamma(\mathbf{x})$  by  $N_{h1}^k$ . As described earlier,  $\Gamma(\mathbf{x})$  is the perturbation of a point  $\mathbf{x}$  in the domain. The configurational force on node  $k$ , in direction  $i$  is thus

$$\begin{aligned} \mathbb{F}_i^{k,0} = & \int \tilde{L} \frac{\partial N_{h1}^k}{\partial x_i} d\mathbf{x} - \int \left\{ \left( \frac{\partial \tilde{L}}{\partial \nabla u(\mathbf{x})} \right)_j \frac{\partial u(\mathbf{x})}{\partial x_i} + \left( \frac{\partial \tilde{L}}{\partial \nabla \phi(\mathbf{x})} \right)_j \frac{\partial \phi(\mathbf{x})}{\partial x_i} \right. \\ & + \sum_{I=1}^M \left( \frac{\partial \tilde{L}}{\partial \nabla \nu_I(\mathbf{x})} \right)_j \frac{\partial \nu_I(\mathbf{x})}{\partial x_i} + \sum_{J=1}^m \left( \frac{\partial \tilde{L}}{\partial \nabla \omega^{\alpha J}(\mathbf{x})} \right)_j \frac{\partial \omega^{\alpha J}(\mathbf{x})}{\partial x_i} \\ & \left. + \sum_{J=1}^m \left( \frac{\partial \tilde{L}}{\partial \nabla \omega^{\beta J}(\mathbf{x})} \right)_j \frac{\partial \omega^{\beta J}(\mathbf{x})}{\partial x_i} \right\} \frac{\partial N_{h1}^k}{\partial x_j} d\mathbf{x} \\ & + \sum_{I=1}^M \left[ \int u^2(\mathbf{x}) \frac{\partial v_{\text{net}}^k(\mathbf{x}, \mathbf{R})}{\partial x_i} N_{h1}^k d\mathbf{x} - + \int u^2(\mathbf{x}) \frac{\partial v_{\text{net}}^k(\mathbf{x}, \mathbf{R})}{\partial x_i} d\mathbf{x} \right] \quad (5.8) \end{aligned}$$

where  $\tilde{L}$  is from equation (3.28),  $\nabla \cdot \Gamma = 0$ , if  $b \neq 0$ ). The domain of integration in these equations is  $\Omega_I$ ;  $I = 1 : M$  if the variable in the integrand is  $\nu_I$  and  $\Omega$  otherwise.

Applying cluster rules as in equations (5.5, 5.7), we get

$$\mathbb{F}_i^k = \sum_{e1 \in T_{h1}} \sum_{\substack{e2 \in e1 \\ e2 \in T_{h3}}} C_{e2} \sum'_{a \in D_{e2}} \mathbb{F}_i^{a,0} N_{h1}^k(\mathbf{x}_a) \quad (5.9)$$

## 5.2 Benchmark Studies: Vacancy

We perform studies to verify and validate the quasi-continuum model by computing the formation energy of a mono vacancy system. To measure the accuracy of the quasi-continuum calculations, we perform large scale explicit Orbital Free DFT calculations and compare the quasi-continuum calculations against these. In the mono-vacancy study, we consider an un-relaxed vacancy in Aluminum and first compute the formation energy on cells containing 31, 107, 255, 499, 863 and 2047 atoms with explicit calculations. We repeat this calculation with the coarse-grained quasi-continuum calculation, with the  $T_{h2}$  mesh having 255 atoms and the results are shown in table 5.1. All calculations are performed with the Bulk Local pseudo potential and WGC kernel functionals.

Table 5.1: Quasi-continuum Orbital Free DFT bench mark calculations on a perfect crystal with a single vacancy. The QC calculations are compared against explicit Orbital Free DFT calculations. All calculations are performed using the Bulk Local pseudo potential and with WGC kernels.

Cluster Size	Number Atoms	Formation Energy (eV) Explicit Calculation	Formation Energy (eV) QC calculation
2x2x2	31	0.517	–
3x3x3	107	0.931	–
4x4x4	255	0.813	0.813
5x5x5	499	0.776	0.773
6x6x6	863	0.762	0.759
8x8x8	2047	0.761	0.759

We can see from the explicit calculations that about 800 atoms are required to obtain a converged vacancy formation energy. The quasi-continuum calculations are accurate to within 2 meV from the explicit calculations, while taking a fraction of the computational expense. As the system size increases, explicit calculations rise linearly in cost, while quasi-continuum calculations rise sub-linearly. With quasi continuum

calculations, simulation cells with millions of atoms are easily attained even as explicit calculations become computationally intractable. These results clearly display that quasi-continuum methods are essential to overcome cell size restrictions on simulations of crystal defects.

## CHAPTER VI

# Electronic structure study of an isolated edge dislocation

Dislocations are line defects in crystalline materials which play a very important role in governing the deformation and failure mechanisms in solids. Continuum theories based on elastic formulations have been widely used to study effects of dislocations on the mechanical properties of crystals (*Rice (1992); Fleck et al. (1994); Nix and Gao (1998); Ghoniem et al. (2000); Arsenlis and Parks (2002)*). In such models, the energetics of dislocations are solely determined by the elastic energy while the core-energy is often assumed to be a constant. In order to overcome the inability of continuum theories to describe the dislocation-core, explicit atomistic calculations based on empirical interatomic potentials have also been employed to study deformation mechanisms mediated by dislocations (*Tadmor et al. (1996b); Kelchner et al. (1998); Gumbsch and Gao (1999); Li et al. (2002b); Marian et al. (2004a,b)*), and have provided many useful insights. However, the interatomic potentials, whose parameters are often fit to bulk properties and some defect properties, may not accurately describe the dislocation-core which is governed by the electronic-structure (*Gumbsch and Daw (1991); Ismail-Beigi and Arias (2000); Woodward et al. (2008)*). Core effects are known to have a strong influence on the crystal properties. The dislocation core is a region with weaker atomic bonding than the rest of the lattice. A change in



the core state influences the dislocation glide process and thus retards or enhances its mobility (*Takeuchi (1999)*). Impeding dislocation mobility through the introduction of solute atoms, precipitates and grain boundaries has been historically exploited for strength hardening of crystals. Core effects are also responsible for temperature and orientation dependence of yield stress in bcc metals (*Duesbery (1969)*). In many materials, the core can exist in several metastable states and in such cases, core energy of a dislocation is the critical parameter in determining the stable core structure. Due to the strong influence of the core on the crystal properties, it is essential to study the core with electronic structure calculations.

## 6.1 Electronic structure study of an isolated edge dislocation

Electronic-structure calculations using plane-wave implementations of density functional theory (DFT) have been employed to study the dislocation-core structure in a wide range of crystalline materials (cf. e.g. *Ismail-Beigi and Arias (2000)*; *Blase et al. (2000)*; *Frederiksen and Jacobsen (2003)*; *Woodward et al. (2008)*; *Clouet et al. (2009)*) and the energetics of dislocation-solute interactions in metals with different symmetries (*Trinkle and Woodward (2005)*; *Yasi et al. (2010)*). As the displacement fields produced by isolated dislocations are not compatible with periodic boundary conditions, these calculations have either been restricted to artificial dipole and quadrupole configurations of dislocations or free-surfaces have been introduced to contain isolated dislocations. While these studies have provided useful insights into the dislocation core-structure, a direct quantification of the dislocation core-energy solely from electronic-structure calculations and its role in governing dislocation behavior has remained elusive thus far. We note that some prior *ab initio* studies using a dipole or quadrupole configuration of dislocations (cf. e.g. *Blase et al. (2000)*; *Li et al. (2004)*; *Clouet et al. (2009)*), have attempted to indirectly compute the core-energy of an isolated dislocation by subtracting from the total energy the elastic

interaction energy between dislocations in the simulation cell and their periodic images. This approach assumes the spacing between dislocations is large enough that the dislocation-cores do not overlap. However, these prior studies have been conducted on computational cells containing a few hundred atoms, which, according to our studies, are much smaller than the core-size of an isolated perfect edge dislocation in Aluminum.

Through large-scale electronic structure calculations, we unambiguously identify the size of the dislocation-core, directly compute the dislocation core-energy, and study the effect of macroscopic deformations on dislocation core-energy. Our studies are performed using large-scale, explicit Orbital Free DFT calculations with the WGC kinetic energy functional, a local density approximation (LDA) for the exchange-correlation energy ( *Perdew and Zunger (1981a)*), and Goodwin-Needs-Heine pseudopotential ( *Goodwin et al. (1990)*). Our real-space, finite-element approach enables consideration of complex geometries and general boundary conditions (Dirichlet, periodic and mixed), which is crucial in resolving the aforementioned limitations of plane-wave basis in the study of energetics of isolated dislocations. We decide against using the quasi-continuum model in this study because the observed cell size effect of a few thousand atoms can be handled by an explicit calculation itself. In the present study, we use quadratic hexahedral finite-elements in all our calculations, where the basis functions correspond to a tensor product of quadratic polynomials. The finite-element discretization and other numerical parameters—quadrature rules and stopping tolerances on iterative solvers—are chosen such that the errors in the computed dislocation energies are less than 0.005 eV. In all our calculations, the atomic relaxations are performed till the maximum force on any atom is less than 0.01 eV/Å.

We first compute elastic constants and the intrinsic stacking fault energy using orbital-free DFT since these are important determinants of dislocation properties. We

also compute these quantities using Kohn-Sham DFT using the same pseudopotential (Goodwin-Needs-Heine pseudopotential) and exchange-correlation (LDA) functional using ABINIT (c.f. *Gonze et al. (2002)*). We see from table 6.1 that the elastic constants and the intrinsic stacking fault energy computed using orbital-free DFT are in close agreement with the Kohn-Sham DFT calculations, demonstrating the accuracy of the WGC orbital-free kinetic energy functional for Aluminum. We note that, prior studies suggest a significant dependence of the stacking fault energy on the choice of the pseudopotential (c.f. *Woodward et al. (2008)*; *Shin et al. (2009a)*), which predict intrinsic stacking fault energies in the range of 55-140 mJ/m<sup>2</sup>. However, as Aluminum is a material with high stacking fault energy, the Shockley partial separation distance is more influenced by the core interactions between the partials rather than the intrinsic stacking fault energy. We note that prior electronic structure studies, including this study, predict a partial separation distance between 9.5-13.7 Å, which is a tight range given the wide spread in the stacking fault energies.

Table 6.1: Computed elastic constants and intrinsic stacking fault energy ( $\gamma_{isf}$ ) with orbital-free DFT and Kohn-Sham DFT. Both sets of calculations are performed with the Goodwin-Needs-Heine pseudo potential.

Method	$C_{11}$ (GPa)	$C_{12}$ (GPa)	$C_{44}$ (GPa)	$\gamma_{isf}$ (mJ/m <sup>2</sup> )
Orbital-free DFT	85.0	57.5	26.6	65.1
Kohn-Sham DFT	83.0	57.6	22.5	67.0

*Dislocation core-size:* In order to compute the dislocation-core energy, we define the energy of a dislocation to be comprised of the stored elastic energy ( $E_{elastic}$ ), associated with the elastic fields outside the dislocation-core, and a core-energy ( $E_{core}$ ) associated with quantum-mechanical and atomistic scale interactions inside the dislocation-core and use this to estimate the dislocation core-size. Prior atomistic calculations have estimated the dislocation core-sizes based on displacement fields to be  $\sim 1 - 3$  |b| (*Yang et al. (2001)*; *Banerjee et al. (2007)*; *Weinberger and Cai (2008)*), where

$\mathbf{b}$  denotes the Burgers vector. While the displacement and strain fields may be well described by elastic formulations outside of a  $1 - 3 |\mathbf{b}|$  core region, the perturbations in electronic-structure due to the dislocation may be present on a larger region. The energetic contributions from these electronic-structure effects can not be captured in continuum elasticity theories or atomistic calculations using empirical potentials. Thus, in the present work, we consider the dislocation-core to be the region where electronic-structure effects and their contribution to the defect energy are significant.

We consider a perfect edge dislocation in face-centered-cubic Aluminum to determine the dislocation core-size. We align our coordinate system,  $X - Y - Z$  axes, along  $[110] - [1\bar{1}1] - [1\bar{1}\bar{2}]$  crystallographic directions, respectively. We begin by considering a perfect crystal of size  $2R\sqrt{2}a_0 \times 2R\sqrt{3}a_0 \times 0.5\sqrt{6}a_0$  where  $a_0$  denotes the lattice parameter and  $R$  is an integer-valued scaling factor used to consider a sequence of increasing simulation domain sizes. A perfect edge dislocation with Burgers vector  $\mathbf{b} = \frac{a_0}{2}[110]$  is introduced at the center of the simulation domain by removing two consecutive half-planes normal to  $[110]$  and applying the continuum displacement fields of an edge dislocation to the positions of atoms. In this work, the displacement fields from isotropic elasticity (c.f *Hirth and Lothe (1968)*) are employed as anisotropic effects are not strong in Aluminum. Upon the application of displacement fields, the geometry of the computational domain is no longer cuboidal, and, thus, the use of a finite-element basis which can accommodate complex geometries is crucial to the present study.

In order to simulate a perfect edge dislocation, we hold the positions of the atoms fixed and compute the electronic-structure using orbital-free DFT. We employ Dirichlet boundary conditions on the electronic fields—comprising of electron-density, electrostatic potential and kernel potentials—in the  $X$  and  $Y$  directions and use periodic boundary conditions along the  $Z$  direction. The Dirichlet boundary conditions are determined under the Cauchy-Born approximation, where the values of electronic fields

on the Dirichlet boundary are computed from periodic unit-cells undergoing the deformations produced by the edge dislocation. The electronic-structure, thus computed, represents an isolated edge-dislocation in bulk with the electronic-structure perturbations from the edge dislocation vanishing on the Dirichlet boundary. The local real-space formulation of orbital-free DFT and the finite-element basis are key to employing these boundary conditions, which are not possible to realize in Fourier-space based formulations.

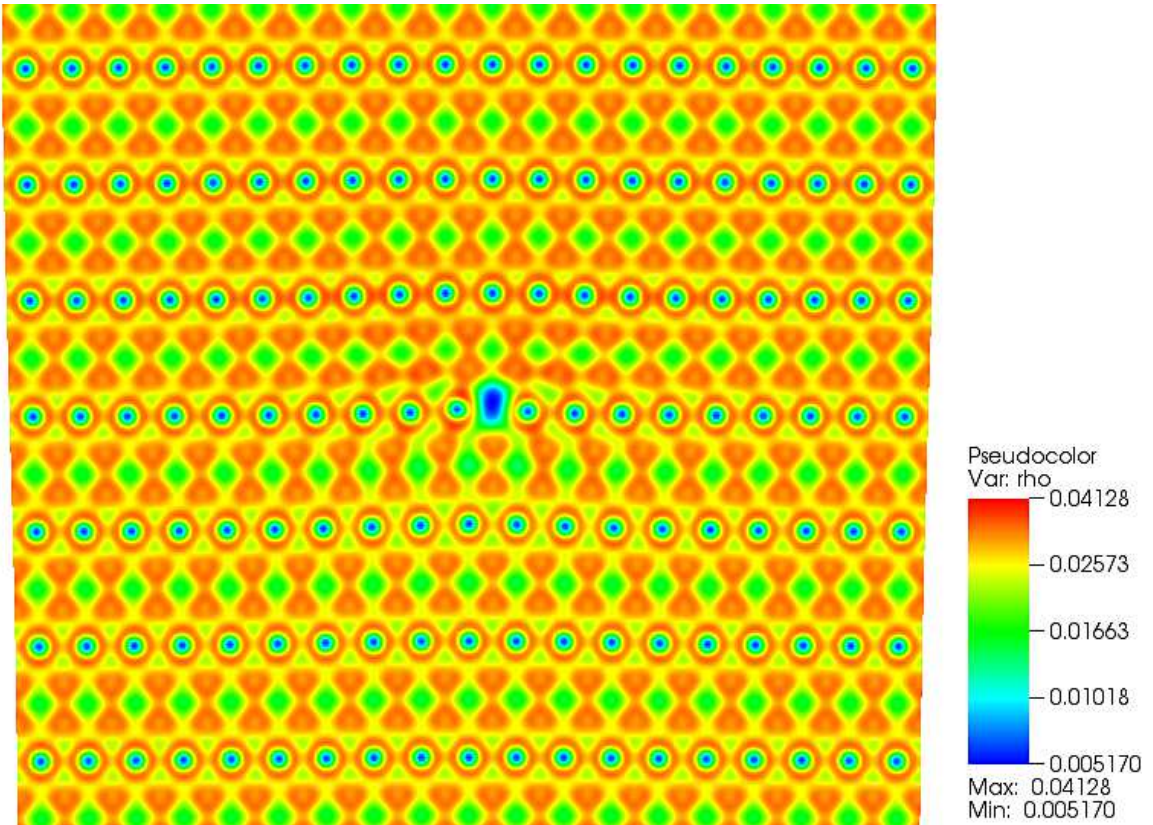


Figure 6.1: Electron-density contours of a perfect edge dislocation in Aluminum.

We computed the electronic-structure and ground-state energy of the perfect edge-dislocation for varying simulation domains with  $R = 2, 3, 4, 5, 7, 9$ . Figure 6.1 shows the contours of the electron-density for  $R = 5$ . We note that a scaling factor  $R$  corresponds to a domain-size where the distance from dislocation line to the boundary along  $[110]$  is  $2R|\mathbf{b}|$ . The dislocation energy ( $E_d$ ) for these various simulation domains

is computed as

$$E_d(N, V) = E_{disloc}(N, V) - E_0(N, V) \quad (6.1)$$

where  $E_{disloc}(N, V)$  denotes the energy of the  $N$  atom system comprising of the dislocation and occupying a volume  $V$ , and  $E_0(N, V)$  denotes energy of a perfect crystal containing the same number of atoms and occupying the same volume. We first computed the dislocation energy at equilibrium volume (i.e.  $V = N\frac{a_0^3}{4}$ ) for the various domain-sizes considered in this study, and the results are presented in Table 6.2. The computed dislocation energy increases with increasing domain-size, and has an asymptotic logarithmic divergence as expected from continuum theories. In order to understand the extent of electronic relaxations, we considered the change in dislocation energy by increasing the domain-size—for instance, from a domain-size of  $2R_1|\mathbf{b}|$  to  $2R_2|\mathbf{b}|$ —and denote this change by  $\Delta E_d$ . This change in the energy has two contributions: (i) the increase in the elastic energy due to the increase in the domain-size, which we denote by  $\Delta E_d^{elas}$ ; (ii) electronic contribution from perturbations in the electronic-structure, which we denote by  $\Delta E_d^{elec}$ . As the elastic energy contribution to the dislocation energy is due to the elastic deformation fields produced by the dislocation, we estimate  $\Delta E_d^{elas}$  by integrating the elastic energy density in the region of interest. The elastic energy density at any point, in turn, is computed from an orbital-free DFT calculation on a unit-cell undergoing the macroscopic deformation produced by the edge dislocation at that point. We verified that the discretization errors in the computation of  $\Delta E_d^{elas}$  are of the order of 0.001 eV. Upon computing  $\Delta E_d^{elas}$ , we infer  $\Delta E_d^{elec}$  from  $\Delta E_d$  ( $\Delta E_d^{elec} = \Delta E_d - \Delta E_d^{elas}$ ). The computed  $\Delta E_d^{elas}$  and  $\Delta E_d^{elec}$  are reported in Table 6.2. It is interesting to note from the results that  $\Delta E_d^{elec}$  is comparable to  $\Delta E_d^{elas}$  up to a domain-size of  $10|\mathbf{b}|$ , suggesting that the electronic-structure perturbations are significant up to distances as far as  $10|\mathbf{b}|$  from the dislocation line. This result is in strong contrast to conventional estimates of core-sizes to be  $1 - 3 |\mathbf{b}|$ . Further, we note that a core-size of  $10|\mathbf{b}|$  contains about

1000 atoms, which is much larger than the computational cells employed in most prior electronic-structure studies of dislocations, and underscores the need to consider sufficiently large simulation domains to accurately compute the energetics of dislocations. In the remainder of this work, we consider  $10|\mathbf{b}|$  to be the core-size of edge dislocation, and the dislocation energy corresponding to this core-size as the dislocation core-energy. For a perfect edge dislocation, the computed core-energy is  $2.548 \text{ eV}$ , or, equivalently, the core-energy per unit length of dislocation line is  $0.515 \text{ eV}/\text{\AA}$ . A plot of the dislocation energies reported in Table 6.2 as a function of domain-size is provided in Figure 6.2, which shows the expected asymptotic logarithmic divergence of the dislocation energy.

Table 6.2: Computed dislocation energy of perfect edge dislocation in Aluminum for varying domain-sizes, where  $N$  denotes the number of atoms in the simulation domain.  $\Delta E_d$  denotes the change in the dislocation energy from the previous domain-size, and  $\Delta E_d^{elas}$  and  $\Delta E_d^{elec}$  denote the elastic and electronic contributions to  $\Delta E_d$ .

Simulation domain	$N$ (atoms)	$E_d$ (eV)	$\Delta E_d$ (eV)	$\Delta E_d^{elas}$ (eV)	$\Delta E_d^{elec}$ (eV)
$4 \mathbf{b} $	179	1.718	-	-	-
$6 \mathbf{b} $	413	2.096	0.378	0.230	0.148
$8 \mathbf{b} $	743	2.334	0.237	0.164	0.073
$10 \mathbf{b} $	1169	2.548	0.215	0.118	0.097
$14 \mathbf{b} $	2309	2.757	0.209	0.187	0.022
$18 \mathbf{b} $	3833	2.91	0.153	0.156	-0.003

*Shockley Partials:* As a next step in our study, we allowed for internal atomic relaxations in the simulation domain corresponding to  $10|\mathbf{b}|$  by holding the positions of atoms fixed on the boundary. Upon atomic relaxations, the perfect edge dislocation splits into Shockley partials. Figure 6.3 shows the edge component of the differential displacements (c.f. *Vitek et al. (1970)*) and indicates the location of the Shockley partials. The partial separation distance computed from the edge-component differential displacement plot is  $12.8 \text{ \AA}$  ( $4.5|\mathbf{b}|$ ). This is in good agreement with other DFT studies which have reported partial separation distances between  $9.5\text{-}13.7 \text{ \AA}$

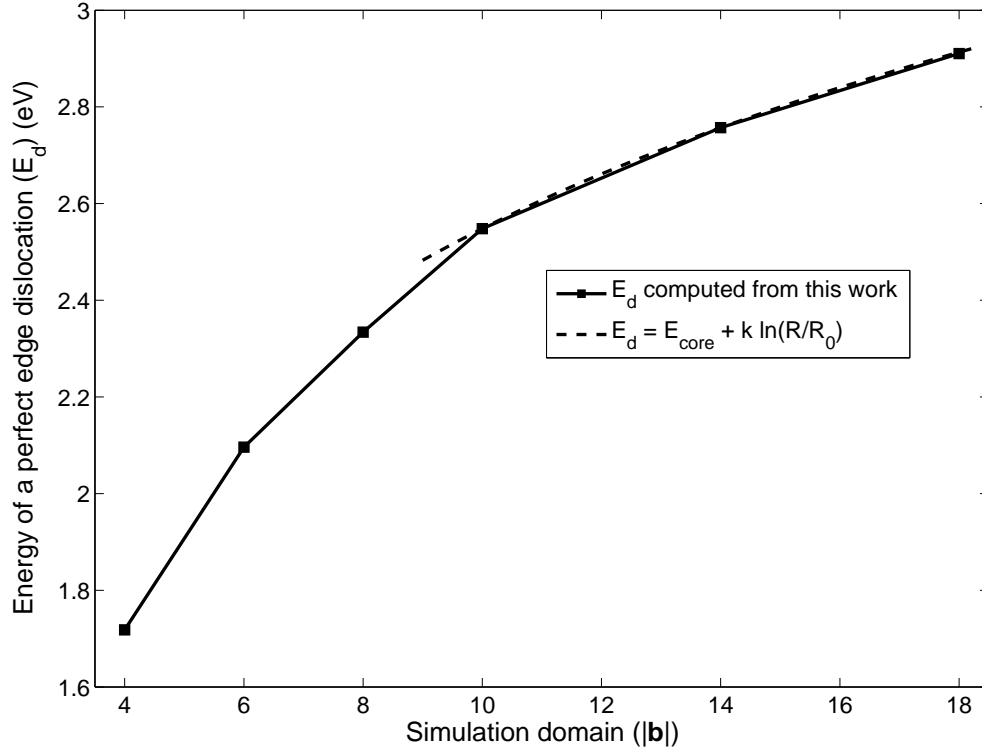


Figure 6.2: Energy of a perfect edge dislocation as a function of simulation domain size.

(c.f. *Woodward et al. (2008)*; *Shin et al. (2009a)*). The core-energy of Shockley partials is computed to be  $1.983 \text{ eV}$ , or, equivalently, the core-energy per unit length of dislocation line is  $0.401 \text{ eV}/\text{\AA}$ .

*Effect of macroscopic deformations on dislocation core-energy:* The interaction of the dislocation core with an applied pressure has been already evidenced by previous atomistic simulations, in particular in fcc and bcc metals (*Gehlen et al. (2003)*; *Clouet et al. (2011)*). Consequences of this pressure contribution on dislocation interactions have been described in (*Hirth (1993)*; *Gehlen et al. (2003)*; *Clouet et al. (2011)*; *Kuan and Hirth (1976)*; *Pizzagalli et al. (2009)*). Motivated by these studies, we calculate the response of the core-energy to externally applied uniaxial, biaxial and volumetric strains. To this end, we impose strains of  $-1.7\%$ ,  $-0.66\%$ ,  $-0.33\%$ ,  $0.33\%$ ,  $0.66\%$  and  $1.7\%$  along a dimension, and compute the core-energy of Shockley partials as a



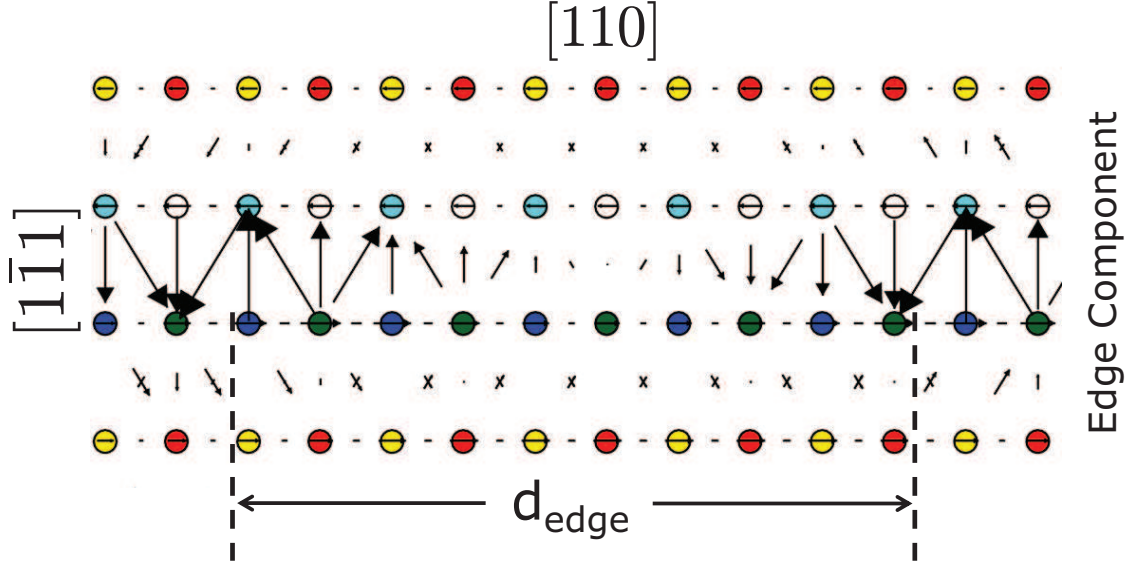


Figure 6.3: Differential displacement plot of the edge component of Shockley partials. The dotted lines represent the location of the partials, and  $d_{edge}$  denotes the partial separation distance.

function of the imposed strains. We do not consider shearing strains in this study as they can cause the dislocation to glide. While dislocation glide is the dominant reason for plasticity, it is not the focus of this study. For the range of strains considered, the partial separation distance in terms of  $|\mathbf{b}|$  was found to be insensitive to applied strain, and is  $\sim 4.5|\mathbf{b}|$ . However, the computed core-energy demonstrated a dependence on macroscopic strain, and is shown in figures 6.4-6.10. The core-energy (per unit length of dislocation line) changed from  $0.48 \text{ eV}/\text{\AA}$  at  $-5\%$  volumetric strain to  $0.34 \text{ eV}/\text{\AA}$  at  $5\%$  volumetric strain, and this change corresponds to a significant fraction ( $\sim 0.3$ ) of the core-energy at equilibrium. This finding is in sharp contrast to the assumptions in continuum formulations that ignore the core-energy in determining the energetics of dislocations and their interactions.

In order to elucidate the role of dislocation core-energy in influencing dislocation behavior, we consider the force on a unit length of dislocation line segment resulting from external loads or other defects. This force has two parts: (i) The classical Peach-

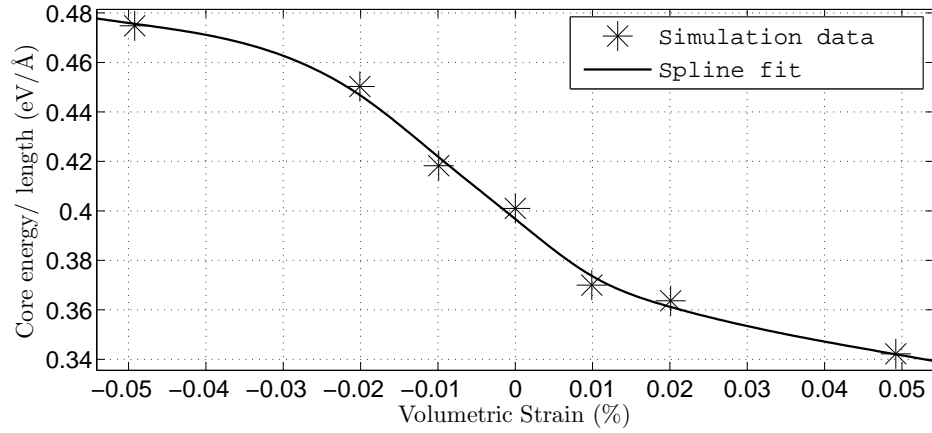


Figure 6.4: Core-energy per unit length of dislocation line of relaxed Shockley partials as a function of macroscopic volumetric strain.

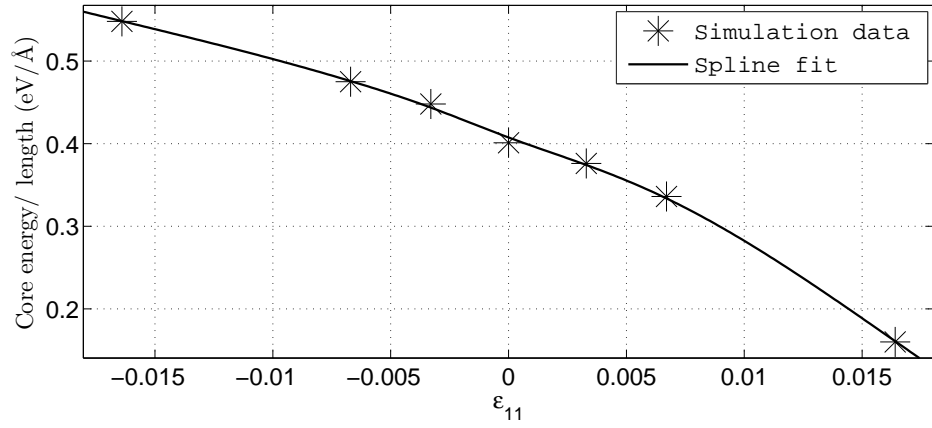


Figure 6.5: Core-energy per unit length of dislocation line of relaxed Shockley partials as a function of uniaxial  $\epsilon_{11}$  strain.

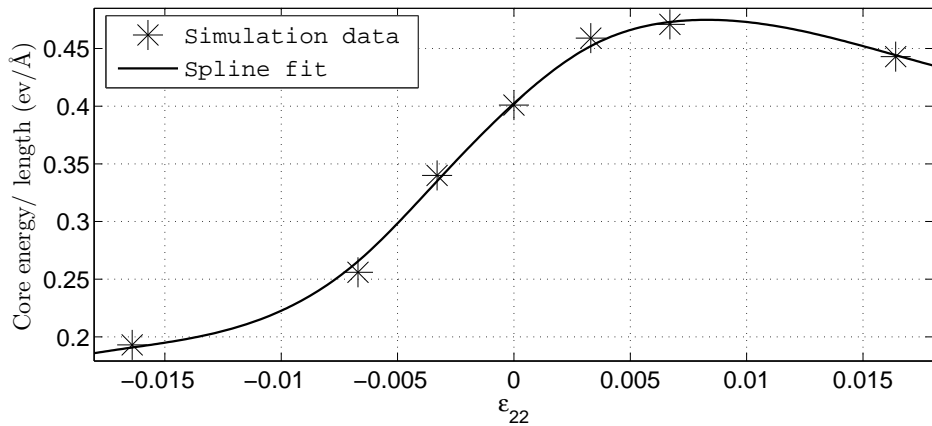


Figure 6.6: Core-energy per unit length of dislocation line of relaxed Shockley partials as a function of macroscopic uniaxial  $\epsilon_{22}$  strain.

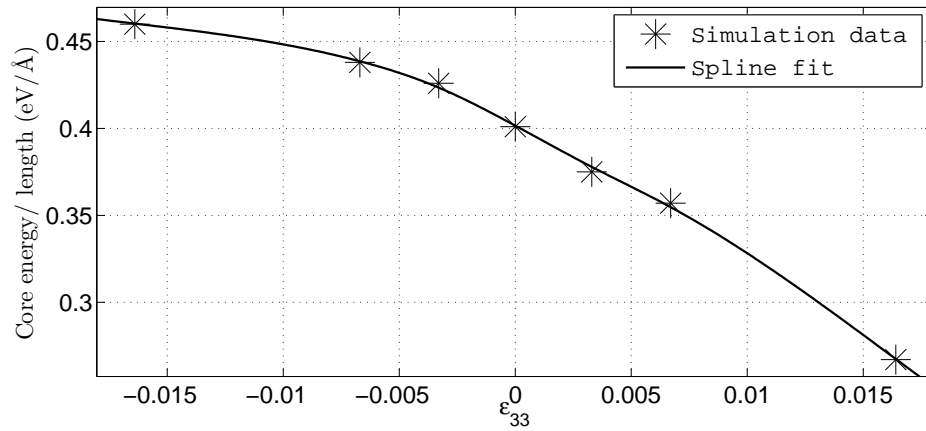


Figure 6.7: Core-energy per unit length of dislocation line of relaxed Shockley partials as a function of macroscopic uniaxial  $\epsilon_{33}$  strain.

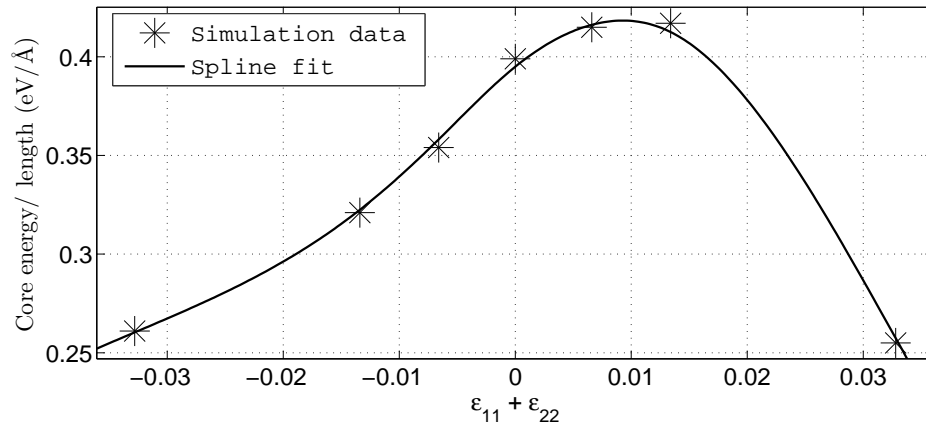


Figure 6.8: Core-energy per unit length of dislocation line of relaxed Shockley partials as a function of macroscopic biaxial  $\epsilon_{11} + \epsilon_{22}$  strain.

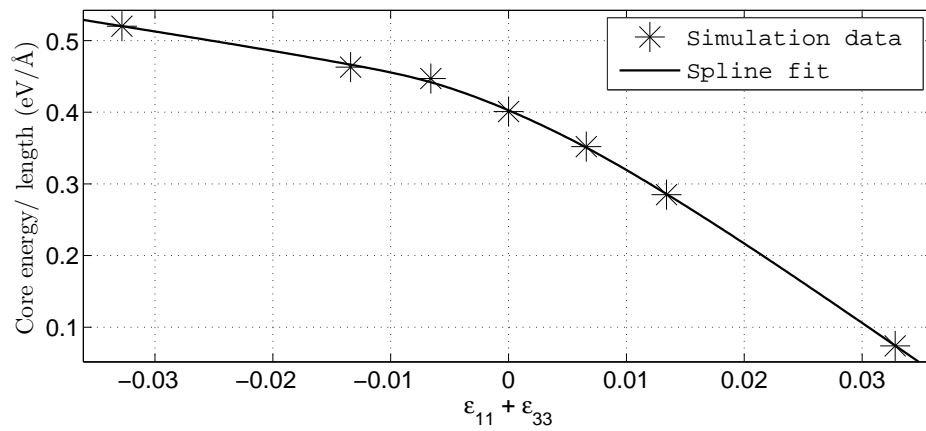


Figure 6.9: Core-energy per unit length of dislocation line of relaxed Shockley partials as a function of macroscopic biaxial  $\epsilon_{11} + \epsilon_{33}$  strain.

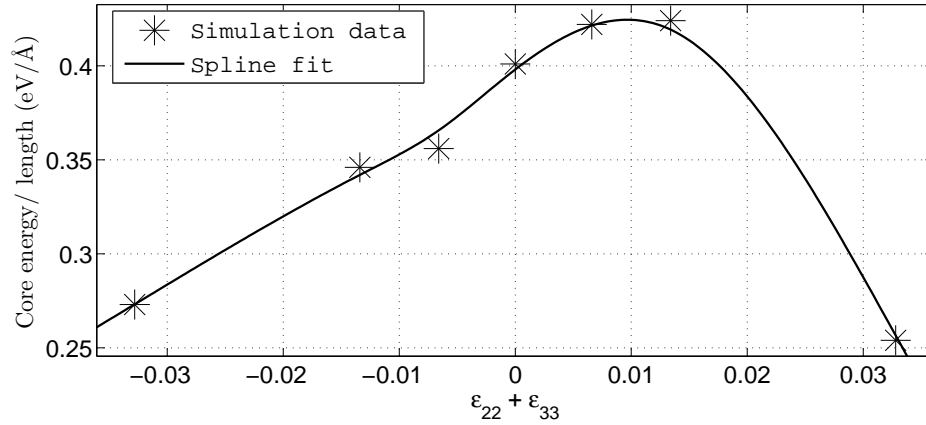


Figure 6.10: Core-energy per unit length of dislocation line of relaxed Shockley partials as a function of macroscopic biaxial  $\epsilon_{22} + \epsilon_{33}$  strain.

Koehler force corresponding to elastic interactions ( *Hirth and Lothe* (1968); *Peach and Koehler* (1950)); (ii) Force due to the core-energy dependence on normal strains (referred to as core-force), given by  $\mathbf{f}^{core} = -\frac{\partial E_{core}}{\partial \epsilon_{11}} \nabla \epsilon_{11} - \frac{\partial E_{core}}{\partial \epsilon_{22}} \nabla \epsilon_{22} - \frac{\partial E_{core}}{\partial \epsilon_{33}} \nabla \epsilon_{33}$  where  $\frac{\partial E_{core}}{\partial \epsilon_{11}}$ ,  $\frac{\partial E_{core}}{\partial \epsilon_{22}}$ ,  $\frac{\partial E_{core}}{\partial \epsilon_{33}}$  are computed from figure 6.5 - 6.7. It is interesting to note that, while the Peach-Koehler force depends on the stress-tensor (which is related to the strain-tensor), the core-force depends on the gradient of strain-tensor and while short-ranged, can be significant in regions of inhomogeneous deformations. We note that a recent work (*Clouet* (2011)), employing an elastic formulation to model the defect-core using dislocation dipoles and line forces, alludes to the possibility of this core-force, but, due to the elastic nature of the formulation, a quantification of this force was beyond reach.

In order to understand the relative importance of this core-force and its implications on dislocation behavior, we consider the interaction force between a dislocation along the  $Z$ -axis located at  $(X, Y) = (0, 0)$  with Burgers vector  $\frac{a_0}{2}[110]$  and another dislocation also along  $Z$ -axis located at  $(X, Y) = (x, y)$  with Burgers vector  $-\frac{a_0}{2}[110]$  (a dislocation dipole). The Peach-Koehler force ( *Peach and Koehler* (1950); *Hirth and Lothe* (1968)) on a unit length of dislocation  $B$  due to the elastic fields from

dislocation  $A$  is given by

$$\mathbf{f}_B^{PK} = \sigma_A \cdot (-\mathbf{b}) \times \xi_B, \quad (6.2)$$

where  $\sigma_A$  denotes the stress tensor associated with the elastic fields produced by dislocation  $A$  at the location of dislocation  $B$  and  $\xi_B$  denotes the unit vector along the dislocation line of  $B$  (unit vector along  $Z$ -axis). The stress tensor associated with the elastic fields of a stationary edge dislocation located at the origin is given by (plane-strain and isotropic elasticity, c.f. *Hirth and Lothe* (1968)):

$$\sigma_{XX} = -\frac{Gb}{2\pi(1-\nu)} \frac{y(3x^2 + y^2)}{(x^2 + y^2)^2} \quad (6.3a)$$

$$\sigma_{YY} = \frac{Gb}{2\pi(1-\nu)} \frac{y(x^2 - y^2)}{(x^2 + y^2)^2} \quad (6.3b)$$

$$\sigma_{XY} = \frac{Gb}{2\pi(1-\nu)} \frac{x(x^2 - y^2)}{(x^2 + y^2)^2} \quad (6.3c)$$

$$\sigma_{ZZ} = \nu(\sigma_{XX} + \sigma_{YY}) \quad (6.3d)$$

$$\sigma_{YZ} = \sigma_{XZ} = 0, \quad (6.3e)$$

where  $G$  denotes the shear modulus,  $\nu$  denotes the Poisson's ratio, and  $b = |\mathbf{b}|$  denotes the magnitude of the Burgers vector. The computed shear modulus and Poisson's ratio are 29 *GPa* and 0.31 respectively. The strain tensor associated with these elastic fields is given by

$$\varepsilon_{XX} = -\frac{by}{2\pi} \frac{Gy^2 + (2\lambda + 3G)x^2}{(\lambda + 2G)(x^2 + y^2)^2} \quad (6.4a)$$

$$\varepsilon_{YY} = \frac{by}{2\pi} \frac{(2\lambda + G)x^2 - Gy^2}{(\lambda + 2G)(x^2 + y^2)^2} \quad (6.4b)$$

$$\varepsilon_{XY} = \frac{b}{2\pi(1-\nu)} \frac{x(x^2 - y^2)}{(x^2 + y^2)^2} \quad (6.4c)$$

$$\varepsilon_{ZZ} = \varepsilon_{ZX} = \varepsilon_{ZY} = 0 \quad (6.4d)$$

$$\varepsilon_v = \varepsilon_{XX} + \varepsilon_{YY} + \varepsilon_{ZZ} = -\frac{Gb}{\pi(\lambda + 2G)} \frac{y}{x^2 + y^2}, \quad (6.4e)$$

where  $\lambda = \frac{2G\nu}{1-2\nu}$  and  $\epsilon_v$  denotes the volumetric strain. We note that the Peach-Koehler force ( $\mathbf{f}^{PK}$ ) decays as  $O(\frac{1}{r})$ , where  $r$  denotes the distance between the two dislocations, which follows from the decay of the stress tensor. On the other hand, the core-force is given by

$$\mathbf{f}^{core} = -2\frac{\partial E^{core}}{\partial \epsilon_{xx}}\nabla\epsilon_{xxA} - 2\frac{\partial E^{core}}{\partial \epsilon_{yy}}\nabla\epsilon_{yyA} - 2\frac{\partial E^{core}}{\partial \epsilon_{zz}}\nabla\epsilon_{zzA} \quad (6.5)$$

where  $\epsilon_{ijA}$  denotes strain at A due to B, and the factor 2 comes due to the strain at B due to A. Noting that  $\nabla\epsilon$  is  $O(\frac{1}{r^2})$ , we note that the core-force also decays as  $O(\frac{1}{r^2})$ . Thus, the core-force is a short-ranged force compared to the Peach-Koehler force.

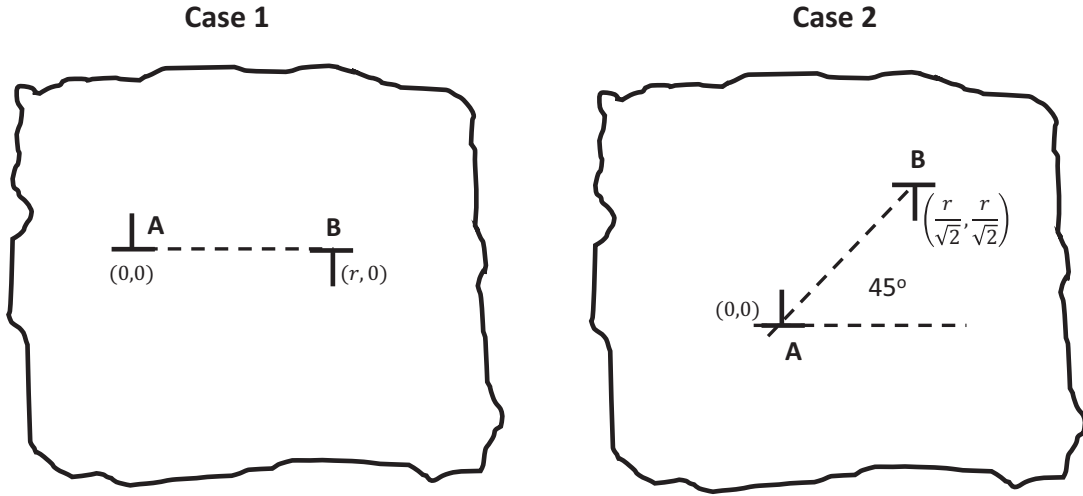


Figure 6.11: Schematics for the two scenarios considered. *Case (i)*: Edge dislocations aligned along the glide plane. *Case (ii)*: Dislocations at an angle of  $45^\circ$ .

In order to understand the relative importance of this core-force and its implications on dislocation behavior, we consider two specific cases as shown in figure 6.11: *Case (i)*  $y = 0$ ; *Case (ii)*  $x = y$ . In the first case, the dislocations are aligned along the glide-plane, whereas in the second case they are at an angle of  $45^\circ$ . For these two cases, we computed the Peach-Koehler force and the core-force on dislocation B.

**Case (i):** For the first case, using the stress tensor from equation 6.3, the Peach-Koehler force is given by

$$\mathbf{f}^{PK} = -\frac{Gb^2}{2\pi(1-\nu)r} \hat{\mathbf{i}}, \quad (6.6)$$

where  $\hat{\mathbf{i}}, \hat{\mathbf{j}}, \hat{\mathbf{k}}$  denote unit vectors along  $X - Y - Z$  axis. Using the strain tensor from equation 6.4, the core-force is given by

$$-\left. \frac{\partial E^{core}}{\partial \varepsilon_{xx}} \right|_{\varepsilon_{xx}=0} \frac{2\lambda + 3G}{\pi(\lambda + 2G)} \frac{b}{r^2} + \left. \frac{\partial E^{core}}{\partial \varepsilon_{yy}} \right|_{\varepsilon_{yy}=0} \frac{2\lambda + G}{\pi(\lambda + 2G)} \frac{b}{r^2} \hat{\mathbf{j}}. \quad (6.7)$$

It is interesting to note that while the Peach-Koehler force exerts a glide force on the dislocation, the core-force exerts a climb force.

**Case (ii):** For the second case, the Peach-Koehler force and the core-force are given by

$$\mathbf{f}^{PK} = -\frac{Gb^2}{2\pi(1-\nu)r} \frac{\sqrt{2}}{r} \hat{\mathbf{j}}, \quad (6.8)$$

$$\mathbf{f}^{core} = -\frac{b}{\pi r^2} \frac{G}{\lambda + 2G} \left( \frac{\partial E^{core}}{\partial \varepsilon_{xx}} + \frac{\partial E^{core}}{\partial \varepsilon_{yy}} \right) \hat{\mathbf{i}} - \frac{b}{\pi r^2} \frac{\lambda + G}{\lambda + 2G} \left( \frac{\partial E^{core}}{\partial \varepsilon_{xx}} - \frac{\partial E^{core}}{\partial \varepsilon_{yy}} \right) \hat{\mathbf{j}} \quad (6.9)$$

It is interesting to note that, for this case, the Peach-Koehler force exerts a climb force on the dislocation, whereas the core-force exerts a glide and climb force.

We next investigated the relative importance of the core-force in governing the dislocation behavior. To this end, we computed the core-force from Case (ii), which corresponds to a glide force on the dislocation, and compared it to the Peierls-Nabarro force—the critical force that will cause dislocation glide. Using 1.6 MPa for the Peierls stress from calculations of (*Shin and Carter (2013)*), we computed the Peierls-Nabarro force (from equation 6.2) on a 1Å length of dislocation line to be  $2.85 \times 10^{-5}$  eV/Å. Using  $\left. \frac{\partial E^{core}}{\partial \varepsilon_{xx}} \right|_{\varepsilon_v=0} = -9.10$ ,  $\left. \frac{\partial E^{core}}{\partial \varepsilon_{yy}} \right|_{\varepsilon_v=0} = 16.34$  eV/Å from figures 6.5 to 6.7, the glide component of the core-force from case (ii) on 1Å length of dislocation line is computed to be  $\frac{-1.82}{r^2}$  eV/Å where  $r$  is the distance between the dislocations  $A$  and  $B$

measured in Angstroms. It is interesting to note that even at a distance of  $25nm$ , the glide component of core-force is larger than the Peierls-Nabarro force. These results suggest that the short-ranged core-force, resulting from the dependence of core-energy on macroscopic deformation, is significant up to many tens of nanometers and can play an important role in governing the behavior of dislocations, especially in regions of inhomogeneous deformations.



## CHAPTER VII

### Conclusions

In chapter II, we have presented a solution to some of the long standing issues in the quasi-continuum method. The approximations involved in various versions of the QC method are known to result in undesirable features, which include a loss of variational structure leading to non-conservative forces, appearance of spurious forces on a perfect periodic lattice, possible lack of stability in the numerical approximations, etc. These in turn can undermine the numerical accuracy and systematic convergence of the QC method. We identify the primary cause of these shortcomings to be the use of a non-local representation of energy to describe the extended interatomic interactions in materials. We demonstrate that cluster summation rules introduced on a non-local representation of energy result in a lack of consistency—approximation errors do not reduce with increasing refinement of the solution space. Cluster summation rules which are introduced in the spirit of numerical quadratures are derived from a local notion of numerical approximation, and result in inconsistent schemes when used on non-local representations of energy.

In the field theoretic formulation for the quasi-continuum method, we resolve these outstanding issues by reformulating the extended interatomic interactions into a local variational problem involving potential fields. We demonstrate this approach for commonly used interatomic potentials. We then introduce the quasi-continuum reduction

of these potential fields following the ideas first suggested in *Gavini et al.* (2007b) in the context of electronic structure calculations. The key ideas behind the quasi-continuum reduction of field theories being: (i) decomposition of potential fields into predictor fields and corrector fields; (ii) an efficient representation of these fields using nested finite-element triangulations—predictor fields being resolved on an auxiliary unit cell, whereas corrector fields being represented on a coarse-grained triangulation; (iii) introduction of quadrature rules which reduce all computations to the complexity commensurate with the coarse-grained variables in the system. We demonstrate that the quasi-continuum reduction of field formulations satisfies the necessary conditions for a consistent numerical approximation, and hence may provide a systematic convergence of the approximation errors. Further, we show using numerical examples the remarkable improvement in the accuracy of the solution afforded by the suggested field approach to the QC method. Numerical results suggest that the approximation errors in a field approach are solely from the coarse-graining of displacement fields which can not be surpassed by any QC formulation. In comparison, other seamless QC formulations based on non-local representations of energy incur orders of magnitude larger numerical errors from quadrature approximations, and also suffer from a lack of systematic convergence.

The suggested field theoretic approach to the quasi-continuum method has the following properties. A single field theory is used to describe the physics in all regions of the model. The formulation is seamless and not reliant on any patching conditions. The formulation has a variational structure and thus the computed forces are conservative. The approximations introduced are consistent, and hence provide a systematic convergence to the exact solution. Moreover, the formulation provides a general framework for the quasi-continuum reduction of any field theory, where quasi-continuum reduction is solely a numerical coarse-graining technique.

It may appear that the computation of potential fields, which requires resolv-

ing these fields on a length-scale finer than interatomic distance, can significantly increase the computational cost. We note that the computation of these potential fields is mostly an overhead cost as it is the initial computation of these fields which is time consuming, and the subsequent evaluations are updates which require very few iterations. On the other hand, the field formulation provides a significant advantage as the computation of forces and energy is in turn a local computation involving the potential fields, unlike force and energy computations in conventional quasi-continuum formulations. In our simulations, force evaluations in the field formulation were about four times more expensive than force evaluations in conventional node-based formulations. However, there is significant room for optimization in our preliminary implementation of the field formulation. For instance, the use of multi-grid approaches can significantly reduce the computational complexity of potential field calculations.

In chapter II we have restricted our attention to a single component material system. Extending the present ideas to multi-component systems requires careful consideration as the PDE's describing potential fields can have different forms in different regions of the model, and presents itself as a direction for future investigations. Further, various numerical analysis aspects which include developing a priori error estimates, investigating the stability and accuracy of the formulation, developing effective preconditioned iterative solvers are potential directions for future investigations.

In chapter III and chapter IV, we conduct a numerical analysis of the finite-element discretization of the orbital-free DFT problem with particular focus on evaluating the computational efficiency afforded by the use of higher-order finite-element discretizations. In order to aid our studies on the computational efficiency of higher-order finite-elements in orbital-free DFT, we developed error estimates for the approximation error in energy in terms of the ground-state electronic fields and characteristic

mesh-size. Using these error estimates and the *a priori* knowledge of the asymptotic solutions of far-field electronic fields, we constructed mesh coarse-graining rates for the various benchmark problems considered in the present study. We note that the proposed approach is similar in spirit to optimal mesh-coarse-graining rates derived based on energy error estimates for the Schrodinger equation by *Levine and Wilkins* (1989), but extended to non-linear problems. Using the proposed mesh adaption strategy, we first investigated the performance of higher-order elements by studying the convergence rates of various elements up to fourth-order including tetrahedral elements, hexahedral elements and spectral finite-elements. In all cases, consistent with recent studies by *Pask and Sterne* (2005); *Chen et al.* (2010), we observed close to optimal convergence rates. It is indeed worthwhile to note that optimal convergence is obtained for higher-order finite-elements discretizations (studied up to fourth order in the present work) of the orbital-free DFT problem even for the case of singular Coulomb potentials, the proof of which, to the best of our knowledge, is an open mathematical problem.

As demonstrated in previous studies by *Hermansson and Yevick* (1986); *Batcho* (2000); *Lehtovaara et al.* (2009), and also observed in the present work, higher-order finite-element discretizations provide a significant degree-of-freedom advantage, i.e., the desired chemical accuracy can be achieved with fewer higher-order basis functions in comparison to linear basis functions. However, the per degree of freedom cost increases with higher-order basis functions due to the increased bandwidth of the matrix corresponding to the discrete system of equations and need for higher-order quadrature rules. In order to assess the practically realized computational efficiency afforded by higher-order finite-element discretizations, we studied the CPU time required to solve the benchmark problems involving atomic systems, periodic systems, as well as larger systems containing up to 666 atom Aluminum clusters. Our results demonstrate that significant computational savings can be realized by using higher-order

elements, which is the main result of the present work. For instance, a staggering 100-1000 fold savings in terms of CPU time and two orders of magnitude better accuracy are realized by using fourth-order hexahedral spectral-elements in comparison to linear tetrahedral elements.

The prospect of using higher-order finite-elements as basis functions for electronic structure calculations is shown to be promising. While finite-elements have the advantages of handling complex geometries and boundary conditions and scale well on massively parallel computing architectures, their use has been limited in electronic structure calculations as they compare unfavorably to plane-wave and atomic-orbital basis functions in terms of computational efficiency. Chapter IV shows that the use of higher-order discretizations can alleviate this problem, and presents a useful direction for electronic structure calculations using finite-element discretization.

Finally, in chapter VI, we employ a real-space finite-element discretization of Orbital Free DFT to compute the core-radius and core-energy of an edge dislocation. We compute the core-radius—the region where electronic-structure effects are significant—to be  $10|\mathbf{b}|$ , which is much larger than those suggested from prior studies. Importantly, the core-energy of Shockley partials is found to be significantly dependent on macroscopic strains. This core-energy dependence on external strains results in an additional short-range core-force, beyond the Peach-Koehler force, in dislocations-dislocation interactions.

To conclude, the work presented in this thesis can be extended in a number of promising ways. Firstly, there are interesting problems which are a straight forward extension of the current work. These include computation of Peierls barrier to dislocation glide, dislocation-solute interactions and their response to external strains and eventually the change in Peierls barrier due to the presence of solute impurities. Secondly, the response of dislocation core energies to external strains can be built into dislocation dynamics simulations through short-ranged corrections to the Peach-

Koehler force. Lastly, the quasi-continuum field theoretic formulation has been shown to be a purely numerical approximation method that is applicable to any local physical model. There is potential extend these ideas to coarse grain Kohn-Sham DFT, which would then enable study of dislocations in bcc transition metals, that are characterized by strong and complex core effects. However, there are some research challenges to be addressed before hand: Kohn-Sham DFT is traditionally formulated in terms of orbitals/ single particle wave functions. Since these orbitals are orthogonal to each other, they oscillate on a global scale and this makes them difficult to coarse-grain. This apart, the electron density in a defect-free crystal is periodic, the Kohn-Sham orbitals are only Bloch-periodic, precluding a straightforward application of Cauchy-Born hypothesis. A coarse-grained model for Kohn-Sham DFT would indeed permit large scale electronic structure calculations on a wide variety of phenomena, systems and materials.

## APPENDICES

## APPENDIX A

### Orbital Free DFT

#### A.1 Estimate of Energy Error with Kernels

Let  $(\bar{u}_h, \bar{\phi}_h, \bar{\mu}_h, \bar{\omega}_h^{\alpha J}, \bar{\omega}_h^{\beta J})$  and  $(\bar{u}, \bar{\phi}, \bar{\mu}, \bar{\omega}^{\alpha J}, \bar{\omega}^{\beta J})$  be the solutions of the discrete finite-element problem and the continuous problem respectively for a given set of nuclear positions. Kernel functionals are valid for periodic systems where ground-state electron-density  $\bar{u}$  is a perturbation of uniform electron gas. Hence, we assume  $\bar{u}$  is bounded from above and below in subsequent analysis. The ground state energy in the discrete and the continuous formulations can be expressed as

$$\begin{aligned}
 E_h(\bar{u}_h, \bar{\phi}_h, \bar{\omega}_h^{\alpha J}, \bar{\omega}_h^{\beta J}) &= \int_{\Omega} \left[ \frac{1}{2} |\nabla \bar{u}_h|^2 + F(\bar{u}_h) - \frac{1}{8\pi} |\nabla \bar{\phi}_h|^2 + (\bar{u}_h^2 + b) \bar{\phi}_h \right] d\mathbf{x} \\
 &+ \sum_{J=1}^m \left\{ \int_{\Omega} \left[ \frac{1}{A_J B_J} \nabla \bar{\omega}_h^{\alpha J} \cdot \nabla \bar{\omega}_h^{\beta J} + \frac{1}{A_J} \bar{\omega}_h^{\alpha J} \bar{\omega}_h^{\beta J} + \bar{\omega}_h^{\beta J} \bar{u}_h^{2\alpha} + \bar{\omega}_h^{\alpha J} \bar{u}_h^{2\beta} + A_J \bar{u}_h^{2(\alpha+\beta)} \right] d\mathbf{x} \right\},
 \end{aligned} \tag{A.1}$$



and

$$\begin{aligned}
E(\bar{u}, \bar{\phi}, \bar{\omega}^{\alpha J}, \bar{\omega}^{\beta J}) &= \int_{\Omega} \left[ \frac{1}{2} |\nabla \bar{u}|^2 + F(\bar{u}) - \frac{1}{8\pi} |\nabla \bar{\phi}|^2 + (\bar{u}^2 + b) \bar{\phi} \right] d\mathbf{x} \\
&+ \sum_{J=1}^m \left\{ \int_{\Omega} \left[ \frac{1}{A_J B_J} \nabla \bar{\omega}^{\alpha J} \cdot \nabla \bar{\omega}^{\beta J} + \frac{1}{A_J} \bar{\omega}^{\alpha J} \bar{\omega}^{\beta J} + \bar{\omega}^{\beta J} \bar{u}^{2\alpha} + \bar{\omega}^{\alpha J} \bar{u}^{2\beta} + A_J \bar{u}^{2(\alpha+\beta)} \right] d\mathbf{x} \right\},
\end{aligned} \tag{A.2}$$

where

$$F(u) = C_F u^{10/3} + \varepsilon_{xc}(u^2)u^2.$$

We begin by expanding  $E_h(\bar{u}_h, \bar{\phi}_h, \bar{\omega}_h^{\alpha J}, \bar{\omega}_h^{\beta J})$  about the solution of the continuous problem, i.e  $\bar{u}_h = \bar{u} + \delta u$ ,  $\bar{\phi}_h = \bar{\phi} + \delta \phi$ ,  $\bar{\omega}_h^{\alpha J} = \bar{\omega}^{\alpha J} + \delta \omega^{\alpha J}$ ,  $\bar{\omega}_h^{\beta J} = \bar{\omega}^{\beta J} + \delta \omega^{\beta J}$ . Using Taylor series expansion, we get

$$\begin{aligned}
E_h(\bar{u}_h, \bar{\phi}_h, \bar{\omega}_h^{\alpha J}, \bar{\omega}_h^{\beta J}) &= \\
&\int_{\Omega} \left\{ \frac{1}{2} |\nabla(\bar{u} + \delta u)|^2 + F(\bar{u} + \delta u) - \frac{1}{8\pi} |\nabla(\bar{\phi} + \delta \phi)|^2 + [(\bar{u} + \delta u)^2 + b] [\bar{\phi} + \delta \phi] \right. \\
&+ \sum_{J=1}^m \left\{ \left[ \frac{1}{A_J B_J} [\nabla(\bar{\omega}^{\alpha J} + \delta \omega^{\alpha J}) \cdot \nabla(\bar{\omega}^{\beta J} + \delta \omega^{\beta J})] + \frac{1}{A_J} (\bar{\omega}^{\alpha J} + \delta \omega^{\alpha J})(\bar{\omega}^{\beta J} + \delta \omega^{\beta J}) \right. \right. \\
&\left. \left. + (\bar{\omega}^{\beta J} + \delta \omega^{\beta J})(\bar{u} + \delta u)^{2\alpha} + (\bar{\omega}^{\alpha J} + \delta \omega^{\alpha J})(\bar{u} + \delta u)^{2\beta} + A_J (\bar{u} + \delta u)^{2(\alpha+\beta)} \right] \right\} d\mathbf{x}.
\end{aligned} \tag{A.3}$$

Since  $(\bar{u}, \bar{\phi}, \bar{\mu}, \bar{\omega}^{\alpha J}, \bar{\omega}^{\beta J})$  are extremal functions, we have

$$\begin{aligned}
&\int_{\Omega} \left\{ \nabla \bar{u} \cdot \nabla \delta u + F'(\bar{u}) \delta u + 2 \bar{u} \delta u \bar{\phi} + \sum_{j=1}^m \left[ 2 \alpha \bar{u}^{2\alpha-1} \delta u \bar{\omega}^{\beta j} + 2 \beta \bar{u}^{2\beta-1} \delta u \bar{\omega}^{\alpha j} \right. \right. \\
&\left. \left. + 2(\alpha + \beta) \bar{u}^{2(\alpha+\beta)-1} \delta u A_j \right] \right\} d\mathbf{x} = - \int_{\Omega} 2 \bar{\mu} \bar{u} \delta u d\mathbf{x}
\end{aligned}$$

$$\begin{aligned}
& \int_{\Omega} \left[ -\frac{1}{4\pi} \nabla \bar{\phi} \cdot \nabla \delta \phi + (\bar{u}^2 + b) \delta \phi \right] d\mathbf{x} = 0, \\
& \int_{\Omega} \left[ \frac{1}{A_J B_J} \nabla \bar{\omega}^{\alpha_J} \cdot \nabla \delta \bar{\omega}^{\beta_J} + \frac{1}{A_J} \bar{\omega}^{\alpha_J} \delta \bar{\omega}^{\beta_J} + u^{2\alpha} \delta \bar{\omega}^{\beta_J} \right] d\mathbf{x} = 0, \\
& \int_{\Omega} \left[ \frac{1}{A_J B_J} \nabla \bar{\omega}^{\beta_J} \cdot \nabla \delta \bar{\omega}^{\alpha_J} + \frac{1}{A_J} \bar{\omega}^{\beta_J} \delta \bar{\omega}^{\alpha_J} + u^{2\beta} \delta \bar{\omega}^{\alpha_J} \right] d\mathbf{x} = 0.
\end{aligned}$$

Using equation (A.3) and the above Euler-Lagrange equations we get

$$\begin{aligned}
E_h - E &= \int_{\Omega} \left\{ \frac{1}{2} |\nabla \delta u|^2 - 2\bar{\mu} \bar{u} \delta u + \frac{1}{2} F''(\bar{u}) (\delta u)^2 - \frac{1}{8\pi} |\nabla \delta \phi|^2 + (\delta u)^2 \bar{\phi} + 2\bar{u} \delta u \delta \phi \right. \\
&+ \sum_{J=1}^m \left\{ \frac{1}{A_J} \delta \omega^{\alpha_J} \delta \omega^{\beta_J} + \frac{1}{A_J B_J} \nabla \delta \omega^{\alpha_J} \cdot \nabla \delta \omega^{\beta_J} + 2\alpha(2\alpha - 1) \bar{\omega}^{\beta_J} \bar{u}^{2\alpha-2} \frac{(\delta u)^2}{2} \right. \\
&+ 2\alpha \bar{u}^{2\alpha-1} \delta u \delta \omega^{\beta_J} + 2\beta(2\beta - 1) \bar{\omega}^{\alpha_J} \bar{u}^{2\beta-2} \frac{(\delta u)^2}{2} + 2\beta \bar{u}^{2\beta-1} \delta u \delta \omega^{\alpha_J} \\
&\left. \left. + 2(\alpha + \beta)(2(\alpha + \beta) - 1) A_J \bar{u}^{2(\alpha+\beta)-2} \frac{(\delta u)^2}{2} \right\} \right\} d\mathbf{x}.
\end{aligned} \tag{A.4}$$

Using equations (4.21) and (A.4), we arrive at the following bound in energy

$$\begin{aligned}
|E_h - E| &\leq \frac{1}{2} \left| \int_{\Omega} |\nabla \delta u|^2 d\mathbf{x} \right| + \bar{\mu} \left| \int_{\Omega} (\delta u)^2 d\mathbf{x} \right| + \frac{1}{2} \left| \int_{\Omega} F''(\bar{u}) (\delta u)^2 d\mathbf{x} \right| \\
&+ \frac{1}{8\pi} \left| \int_{\Omega} |\nabla \delta \phi|^2 d\mathbf{x} \right| + \left| \int_{\Omega} (\delta u)^2 \bar{\phi} d\mathbf{x} \right| + 2 \left| \int_{\Omega} \bar{u} \delta u \delta \phi d\mathbf{x} \right| + \sum_{J=1}^m \left\{ \left| \int_{\Omega} \frac{1}{A_J} \delta \omega^{\alpha_J} \delta \omega^{\beta_J} d\mathbf{x} \right| \right. \\
&+ \left| \int_{\Omega} \frac{1}{A_J B_J} \nabla \delta \omega^{\alpha_J} \cdot \nabla \delta \omega^{\beta_J} d\mathbf{x} \right| + \left| \int_{\Omega} 2\alpha(2\alpha - 1) \bar{\omega}^{\beta_J} \bar{u}^{2\alpha-2} \frac{(\delta u)^2}{2} d\mathbf{x} \right| \\
&+ \left| \int_{\Omega} 2\alpha \bar{u}^{2\alpha-1} \delta u \delta \omega^{\beta_J} d\mathbf{x} \right| + \left| \int_{\Omega} 2\beta(2\beta - 1) \bar{\omega}^{\alpha_J} \bar{u}^{2\beta-2} \frac{(\delta u)^2}{2} d\mathbf{x} \right| + \left| \int_{\Omega} 2\beta \bar{u}^{2\beta-1} \delta u \delta \omega^{\alpha_J} d\mathbf{x} \right| \\
&\left. + \left| \int_{\Omega} 2(\alpha + \beta)(2(\alpha + \beta) - 1) A_J \bar{u}^{2(\alpha+\beta)-2} \frac{(\delta u)^2}{2} d\mathbf{x} \right| \right\}.
\end{aligned} \tag{A.5}$$

We next find an optimal bound for the kernel terms involved in  $|E_h - E|$ . As before, let  $|\cdot|_{1,\Omega}$  represents the semi-norm in  $H^1$  space,  $\|\cdot\|_{1,\Omega}$  represents the  $H^1$  norm,  $\|\cdot\|_{0,\Omega}$  represents the standard  $L^2$  norm,  $\|\cdot\|_{0,p,\Omega}$  represents  $L^p$  norm. Firstly note that using Hölder inequality, we have

$$\begin{aligned} \left| \int_{\Omega} \frac{1}{A_J} \delta\omega^{\alpha_J} \delta\omega^{\beta_J} d\mathbf{x} \right| &= \left| \frac{1}{A_J} \right| \left| \int_{\Omega} \delta\omega^{\alpha_J} \delta\omega^{\beta_J} d\mathbf{x} \right| \\ &\leq C_1 \int_{\Omega} |\delta\omega^{\alpha_J} \delta\omega^{\beta_J}| d\mathbf{x} \leq C_1 \|\bar{\omega}^{\alpha_J} - \bar{\omega}_h^{\alpha_J}\|_{0,\Omega} \|\bar{\omega}^{\beta_J} - \bar{\omega}_h^{\beta_J}\|_{0,\Omega} \end{aligned} \quad (\text{A.6})$$

and

$$\begin{aligned} \left| \int_{\Omega} \frac{1}{A_J B_J} \nabla \delta\omega^{\alpha_J} \cdot \nabla \delta\omega^{\beta_J} d\mathbf{x} \right| &= \left| \frac{1}{A_J B_J} \right| \left| \int_{\Omega} \nabla \delta\omega^{\alpha_J} \cdot \nabla \delta\omega^{\beta_J} d\mathbf{x} \right| \\ &\leq C_2 \int_{\Omega} |\nabla \delta\omega^{\alpha_J} \cdot \nabla \delta\omega^{\beta_J}| d\mathbf{x} \\ &\leq C_2 \|\nabla(\bar{\omega}^{\alpha_J} - \bar{\omega}_h^{\alpha_J})\|_{0,\Omega} \|\nabla(\bar{\omega}^{\beta_J} - \bar{\omega}_h^{\beta_J})\|_{0,\Omega} \\ &= C_2 |\bar{\omega}^{\alpha_J} - \bar{\omega}_h^{\alpha_J}|_{1,\Omega} |\bar{\omega}^{\beta_J} - \bar{\omega}_h^{\beta_J}|_{1,\Omega}. \end{aligned} \quad (\text{A.7})$$

Using Hölder inequality and the Sobolev inequality, we arrive at

$$\begin{aligned} \left| \int_{\Omega} 2\alpha(2\alpha - 1) \bar{\omega}^{\beta_J} \bar{u}^{2\alpha-2} \frac{(\delta u)^2}{2} d\mathbf{x} \right| &\leq C_3 \int_{\Omega} |\bar{\omega}^{\beta_J} \bar{u}^{2\alpha-2} (\delta u)^2| d\mathbf{x} \\ &\leq C_3 \|\bar{\omega}^{\beta_J} \bar{u}^{2\alpha-2}\|_{0,\Omega} \|(\bar{u} - \bar{u}_h)^2\|_{0,\Omega} \\ &= C_3 \|\bar{\omega}^{\beta_J} \bar{u}^{2\alpha-2}\|_{0,\Omega} \|\bar{u} - \bar{u}_h\|_{0,4,\Omega}^2 \\ &\leq \bar{C}_3 \|\bar{u} - \bar{u}_h\|_{1,\Omega}^2. \end{aligned} \quad (\text{A.8})$$

Further, note that

$$\begin{aligned}
\left| \int_{\Omega} 2 \alpha \bar{u}^{2\alpha-1} \delta u \delta \omega^{\beta J} d\mathbf{x} \right| &\leq C_4 \int_{\Omega} |\bar{u}^{2\alpha-1} \delta u \delta \omega^{\beta J}| d\mathbf{x} \\
&\leq C_4 \|\bar{u}^{2\alpha-1}\|_{0,6,\Omega} \|\bar{u} - \bar{u}_h\|_{0,\Omega} \|\bar{\omega}^{\beta J} - \bar{\omega}_h^{\beta J}\|_{0,3,\Omega} \\
&\leq \bar{C}_4 \|\bar{u} - \bar{u}_h\|_{0,\Omega} \|\bar{\omega}^{\beta J} - \bar{\omega}_h^{\beta J}\|_{1,\Omega} .
\end{aligned} \tag{A.9}$$

where we made use of generalized Holder inequality in the first step and Sobolev inequality in the next. Also one can show that

$$\begin{aligned}
\left| \int_{\Omega} 2 \beta (2\beta - 1) \bar{\omega}^{\alpha J} \bar{u}^{2\beta-2} \frac{(\delta u)^2}{2} d\mathbf{x} \right| &\leq C_5 \int_{\Omega} |\bar{\omega}^{\alpha J} \bar{u}^{2\beta-2} (\delta u)^2| d\mathbf{x} \\
&\leq C_5 \|\bar{\omega}^{\alpha J} \bar{u}^{2\beta-2}\|_{0,\Omega} \|(\bar{u} - \bar{u}_h)^2\|_{0,\Omega} \\
&= C_5 \|\bar{\omega}^{\alpha J} \bar{u}^{2\beta-2}\|_{0,\Omega} \|\bar{u} - \bar{u}_h\|_{0,4,\Omega}^2 \\
&\leq \bar{C}_5 \|\bar{u} - \bar{u}_h\|_{1,\Omega}^2
\end{aligned} \tag{A.10}$$

and

$$\begin{aligned}
\left| \int_{\Omega} 2 \beta \bar{u}^{2\beta-1} \delta u \delta \omega^{\alpha J} d\mathbf{x} \right| &\leq C_6 \int_{\Omega} |\bar{u}^{2\beta-1} \delta u \delta \omega^{\alpha J}| d\mathbf{x} \\
&\leq \bar{C}_6 \|\bar{u} - \bar{u}_h\|_{0,\Omega} \|\bar{\omega}^{\alpha J} - \bar{\omega}_h^{\alpha J}\|_{1,\Omega} .
\end{aligned} \tag{A.11}$$

Using the bounds derived above, it follows that

$$\begin{aligned}
|E_h - E| &\leq C \left[ \|\bar{u} - \bar{u}_h\|_{1,\Omega}^2 + |\bar{\phi} - \bar{\phi}_h|_{1,\Omega}^2 + \|\bar{u} - \bar{u}_h\|_{0,\Omega} \|\bar{\phi} - \bar{\phi}_h\|_{1,\Omega} \right. \\
&\quad + \sum_{J=1}^m \left\{ \|\bar{\omega}^{\alpha J} - \bar{\omega}_h^{\alpha J}\|_{0,\Omega} \|\bar{\omega}^{\beta J} - \bar{\omega}_h^{\beta J}\|_{0,\Omega} + |\bar{\omega}^{\alpha J} - \bar{\omega}_h^{\alpha J}|_{1,\Omega} |\bar{\omega}^{\beta J} - \bar{\omega}_h^{\beta J}|_{1,\Omega} \right. \\
&\quad \left. \left. + \|\bar{u} - \bar{u}_h\|_{0,\Omega} \|\bar{\omega}^{\alpha J} - \bar{\omega}_h^{\alpha J}\|_{1,\Omega} + \|\bar{u} - \bar{u}_h\|_{0,\Omega} \|\bar{\omega}^{\beta J} - \bar{\omega}_h^{\beta J}\|_{1,\Omega} \right\} \right] .
\end{aligned} \tag{A.12}$$

Now in the neighbourhood of the solution  $(\bar{u}, \bar{\phi}, \bar{\mu}, \bar{\omega}^{\alpha_J}, \bar{\omega}^{\beta_J})$ , we bound the above estimates with the interpolation error and then bound them with finite-element mesh size in the similar lines of Section 4.3.

$$|\bar{\omega}^{\alpha_J} - \bar{\omega}_h^{\alpha_J}|_{1,\Omega} \leq \bar{C} |\bar{\omega}^{\alpha_J} - \bar{\omega}_I^{\alpha_J}|_{1,\Omega} \leq \tilde{C} \sum_e h_e^k |\bar{\omega}^{\alpha_J}|_{k+1,\Omega_e}, \quad (\text{A.13a})$$

$$\| \bar{\omega}^{\alpha_J} - \bar{\omega}_h^{\alpha_J} \|_{0,\Omega} \leq \bar{C}_0 \| \bar{\omega}^{\alpha_J} - \bar{\omega}_I^{\alpha_J} \|_{0,\Omega} \leq \tilde{C}_0 \sum_e h_e^{k+1} |\bar{\omega}^{\alpha_J}|_{k+1,\Omega_e}, \quad (\text{A.13b})$$

$$|\bar{\omega}^{\beta_J} - \bar{\omega}_h^{\beta_J}|_{1,\Omega} \leq \bar{C} |\bar{\omega}^{\beta_J} - \bar{\omega}_I^{\beta_J}|_{1,\Omega} \leq \tilde{C} \sum_e h_e^k |\bar{\omega}^{\beta_J}|_{k+1,\Omega_e}, \quad (\text{A.13c})$$

$$\| \bar{\omega}^{\beta_J} - \bar{\omega}_h^{\beta_J} \|_{0,\Omega} \leq \bar{C}_0 \| \bar{\omega}^{\beta_J} - \bar{\omega}_I^{\beta_J} \|_{0,\Omega} \leq \tilde{C}_0 \sum_e h_e^{k+1} |\bar{\omega}^{\beta_J}|_{k+1,\Omega_e}. \quad (\text{A.13d})$$

Hence the error estimate in energy is given by

$$\begin{aligned} |E_h - E| &\leq \mathcal{C} \sum_e \left[ h_e^{2k} |\bar{u}|_{k+1,\Omega_e}^2 + h_e^{2k} |\bar{\phi}|_{k+1,\Omega_e}^2 + h_e^{2k+1} |\bar{u}|_{k+1,\Omega_e} |\bar{\phi}|_{k+1,\Omega_e} \right. \\ &+ \sum_{J=1}^m \left\{ h_e^{2k+2} |\bar{\omega}^{\alpha_J}|_{k+1,\Omega_e} |\bar{\omega}^{\beta_J}|_{k+1,\Omega_e} + h_e^{2k} |\bar{\omega}^{\alpha_J}|_{k+1,\Omega_e} |\bar{\omega}^{\beta_J}|_{k+1,\Omega_e} \right. \\ &\left. \left. + h_e^{2k+1} |\bar{u}|_{k+1,\Omega_e} |\bar{\omega}^{\beta_J}|_{k+1,\Omega_e} + h_e^{2k+1} |\bar{u}|_{k+1,\Omega_e} |\bar{\omega}^{\alpha_J}|_{k+1,\Omega_e} \right\} \right]. \end{aligned} \quad (\text{A.14})$$

The error estimate to  $O(h^{2k+1})$  is therefore given by

$$|E_h - E| \leq \mathcal{C} \sum_e \left[ h_e^{2k} |\bar{u}|_{k+1,\Omega_e}^2 + h_e^{2k} |\bar{\phi}|_{k+1,\Omega_e}^2 + \sum_{J=1}^m \left\{ h_e^{2k} |\bar{\omega}^{\alpha_J}|_{k+1,\Omega_e} |\bar{\omega}^{\beta_J}|_{k+1,\Omega_e} \right\} \right] \quad (\text{A.15})$$

## A.2 Discrete formulation of electrostatic interactions

The electrostatic interaction energy in the discrete formulation is given by

$$E_{\text{electrostatic}}^h = \left[ -\frac{1}{8\pi} \int_{\Omega} |\nabla \phi_h(\mathbf{x})|^2 d\mathbf{x} + \int_{\Omega} (u_h^2(\mathbf{x}) + b(\mathbf{x})) \phi_h(\mathbf{x}) d\mathbf{x} \right] - E_{\text{self}}^h \quad \text{where} \quad (\text{A.16})$$

$$E_{\text{self}}^h = \frac{1}{2} \sum_{I=1}^M \int_{\Omega} \delta(\mathbf{x} - \mathbf{R}_I) V_{h_I}(\mathbf{x}) d\mathbf{x} . \quad (\text{A.17})$$

In the above expression  $\phi_h$  denotes the total electrostatic potential field, corresponding to the electron-density  $u_h^2$  and nuclear charge distribution  $b(\mathbf{x})$ , computed in the finite-element basis.  $V_{h_I}$  denotes the nuclear potential corresponding to the  $I^{\text{th}}$  nuclear charge, denoted by  $\delta(\mathbf{x} - \mathbf{R}_I)$ , computed in the finite-element basis. In the finite-element discretization of all-electron calculations, we treat the nuclear charges as point charges located on the nodes of the finite-element triangulation. The discreteness of the finite-element triangulation provides a regularization of the potential fields, despite nuclear charges being treated as point charges. However, the self-energy of the nuclei in this case is mesh-dependent and diverges upon mesh refinement. Thus, care must be taken to evaluate the total electrostatic potential  $\phi_h$  and the nuclear potentials  $V_{h_I}$ ,  $I = 1, \dots, M$  on the same finite-element mesh. The electrostatic interaction energy in equation (A.16) can be simplified to

$$E_{\text{electrostatic}}^h = \frac{1}{2} \int_{\Omega} u_h^2(\mathbf{x}) \phi_h(\mathbf{x}) d\mathbf{x} + \underbrace{\frac{1}{2} \int_{\Omega} b(\mathbf{x}) \phi_h(\mathbf{x}) d\mathbf{x}}_{(a)} - \underbrace{\frac{1}{2} \sum_{I=1}^M \int_{\Omega} \delta(\mathbf{x} - \mathbf{R}_I) V_{h_I}(\mathbf{x}) d\mathbf{x}}_{(b)} . \quad (\text{A.18})$$

In the above expression, the first term on the righthand side contains electron-electron interaction energy and half contribution of the electron-nuclear interaction

energy. The term (a) contains the other half of the electron-nuclear interaction energy, nuclear-nuclear repulsion energy, and the self energy of the nuclei. The term (b) represents the self energy of the nuclei. By evaluating all the electrostatic potentials on the same finite-element mesh, the divergent self energy contribution in term (a) equals the sum of separately evaluated divergent self-energy terms in (b) owing to the linearity of the Poisson problem. The boundary conditions used for the computation of the discrete potential fields are homogeneous Dirichlet boundary conditions for total electrostatic potential ( $\phi_h$ ) and Dirichlet boundary conditions with the prescribed Coulomb potential for nuclear potentials ( $V_{h_I}$ ), applied on a large enough domain where the boundary conditions become realistic. We present numerical results to corroborate the fact that the diverging components of self energy in terms (a) and (b) indeed cancel. To this end, we present the case study of the electrostatic interaction energy, computed using two types of elements “HEX8” and “HEX125SPECTRAL” with varying mesh sizes, of a Helium atom ( $Z_I = 2$ ) with  $u_h(\mathbf{x})$  given by equation (58) with  $\lambda = 0.2$ ,  $\bar{\mu} = 0.1$ . The results in tables (A.1)-(A.2) show that while terms (a) and (b) diverge upon mesh refinement, the electrostatic energy nevertheless converges suggesting the cancelation of divergent self energy terms.

Degrees of Freedom	Term (a)(Ha.)	Term (b)(Ha.)	$E_{electrostatic}^h$ (Ha.)
313	422.06232	423.95270	-2.61289
2281	871.12178	873.09235	-2.71462
17713	1755.99626	1757.98873	-2.74103
140257	3517.91090	3519.90901	-2.74775
1117633	7038.91408	7040.91360	-2.74944
8926081	14080.11011	14082.11000	-2.74986

Table A.1: Convergence of  $E_{electrostatic}^h$  for “HEX8” element

Degrees of Freedom	Term (a)	Term (b)	$E_{electrostatic}^h$
17713	3603.40360	3605.40357	-2.74995
140257	7233.78712	7235.78714	-2.7499899
1117633	14469.7040	14471.70400	-2.7499984

Table A.2: Convergence of  $E_{electrostatic}^h$  for “HEX125SPECTRAL” element



## BIBLIOGRAPHY

## BIBLIOGRAPHY

- Anderson, D. (1965), Iterative procedures for nonlinear integral equations, *Journal of the ACM (JACM)*, 12(4), 547–560.
- Arsenlis, A., and D. M. Parks (2002), Modeling the evolution of crystallographic dislocation density in crystal plasticity, *Journal of the Mechanics and Physics of Solids*, 50, 1979–2009.
- Ashcroft, N. W., and N. D. Mermin (2005), Solid state physics (holt, rinehart and winston, new york, 1976), *There is no corresponding record for this reference.*
- Bacon, D., D. Barnett, and R. O. Scattergood (1980), Anisotropic continuum theory of lattice defects, *Progress in Materials Science*, 23, 51–262.
- Balay, S., et al. (2014), PETSc Web page.
- Banerjee, S., N. Ghoniem, G. Lu, and N. Kioussis (2007), Non-singular descriptions of dislocation cores: a hybrid ab initio continuum approach, *Philosophical Magazine*, 87, 4131–4150.
- Batcho, P. (2000), Computational method for general multicenter electronic structure calculations, *Physical Review E*, 61(6), 7169.
- Beck, T. L. (2000), Real-space mesh techniques in density-functional theory, *Reviews of Modern Physics*, 72(4), 1041.
- Blanc, X., and E. Cancès (2004), Nonlinear instability of density-independent orbital-free kinetic energy functionals, *arXiv preprint cond-mat/0409081*.
- Blanc, X., C. Le Bris, and P.-L. Lions (2002), From molecular models to continuum mechanics, *Archive for Rational Mechanics and Analysis*, 164(4), 341–381.
- Blase, X., K. Lin, A. Canning, S. G. Louie, and D. C. Chrzan (2000), Structure and energy of the 90° partial dislocation in diamond: A combined *Ab Initio* and elasticity theory analysis, *Phys. Rev. Lett.*, 84, 5780–5783.
- Boyd, J. (2001), *Chebyshev and Fourier spectral methods*, Dover publications.
- Cancès, E., R. Chakir, and Y. Maday (2010), Numerical analysis of nonlinear eigenvalue problems, *Journal of Scientific Computing*, 45(1-3), 90–117.

- Ceperley, D. M., and B. J. Alder (1980), Ground state of the electron gas by a stochastic method, *Phys. Rev. Lett.*, *45*, 566–569, doi:10.1103/PhysRevLett.45.566.
- Chen, H., X. Gong, and A. Zhou (2010), Numerical approximations of a nonlinear eigenvalue problem and applications to a density functional model, *Mathematical Methods in the Applied Sciences*, *33*(14), 1723–1742.
- Choly, N., and E. Kaxiras (2002), Kinetic energy density functionals for non-periodic systems, *Solid state communications*, *121*(5), 281–286.
- Ciarlet, P. G. (1978), *The finite element method for elliptic problems*, Elsevier.
- Clouet, E. (2011), Dislocation core field. i. modeling in anisotropic linear elasticity theory, *Phys. Rev. B*, *84*, 224,111.
- Clouet, E., L. Ventelon, and F. Willaime (2009), Dislocation core energies and core fields from first principles, *Phys. Rev. Lett.*, *102*, 055,502.
- Clouet, E., L. Ventelon, and F. Willaime (2011), Dislocation core field. ii. screw dislocation in iron, *Physical Review B*, *84*(22), 224,107.
- Curtin, W. A., and R. E. Miller (2003), Atomistic/continuum coupling in computational materials science, *Modelling and simulation in materials science and engineering*, *11*(3), R33.
- Daw, M. S., and M. I. Baskes (1984), Embedded-atom method: Derivation and application to impurities, surfaces, and other defects in metals, *Physical Review B*, *29*(12), 6443.
- Dobson, M., and M. Luskin (2008), Analysis of a force-based quasicontinuum approximation, *ESAIM: Mathematical Modelling and Numerical Analysis*, *42*(01), 113–139.
- Dobson, M., M. Luskin, and C. Ortner (2010), Accuracy of quasicontinuum approximations near instabilities, *Journal of the Mechanics and Physics of Solids*, *58*(10), 1741–1757.
- Duesbery, M. (1969), The influence of core structure on dislocation mobility, *Philosophical Magazine*, *19*(159), 501–526.
- Eidel, B., and A. Stukowski (2009), A variational formulation of the quasicontinuum method based on energy sampling in clusters, *Journal of the Mechanics and Physics of Solids*, *57*(1), 87–108.
- Eshelby, J. D. (1957), The determination of the elastic field of an ellipsoidal inclusion, and related problems, *Proceedings of the Royal Society of London. Series A. Mathematical and Physical Sciences*, *241*(1226), 376–396.
- Fleck, N., G. Muller, M. Ashby, and J. Hutchinson (1994), Strain gradient plasticity: Theory and experiment, *Acta Metallurgica et Materialia*, *42*, 475 – 487.

- Frederiksen, S. L., and K. W. Jacobsen (2003), Density functional theory studies of screw dislocation core structures in bcc metals, *Philosophical Magazine*, *83*, 365–375.
- Gavini, V., and L. Liu (2011), A homogenization analysis of the field theoretic approach to the quasi-continuum method, *Journal of the Mechanics and Physics of Solids*, *59*(8), 1536–1551.
- Gavini, V., K. Bhattacharya, and M. Ortiz (2007a), Quasi-continuum orbital-free density-functional theory: A route to multi-million atom non-periodic dft calculation, *Journal of the Mechanics and Physics of Solids*, *55*(4), 697–718.
- Gavini, V., J. Knap, K. Bhattacharya, and M. Ortiz (2007b), Non-periodic finite-element formulation of orbital-free density functional theory, *Journal of the Mechanics and Physics of Solids*, *55*(4), 669–696.
- Gehlen, P., J. Hirth, R. Hoagland, and M. Kanninen (2003), A new representation of the strain field associated with the cube-edge dislocation in a model of a  $\alpha$ -iron, *Journal of Applied Physics*, *43*(10), 3921–3933.
- Ghoniem, N. M., S.-H. Tong, and L. Z. Sun (2000), Parametric dislocation dynamics: A thermodynamics-based approach to investigations of mesoscopic plastic deformation, *Phys. Rev. B*, *61*, 913–927.
- Gonze, X., et al. (2002), First-principles computation of material properties: the abinit software project, *Computational Materials Science*, *25*(3), 478–492.
- Goodwin, L., R. J. Needs, and V. Heine (1990), *J. Phys. Condens. Matter*, *2*, 351.
- Gumbsch, P., and M. S. Daw (1991), Interface stresses and their effects on the elastic moduli of metallic multilayers, *Phys. Rev. B*, *44*, 3934–3938.
- Gumbsch, P., and H. Gao (1999), Dislocations faster than the speed of sound, *Science*, *283*, 965–968.
- Gunzburger, M., and Y. Zhang (2010), A quadrature-rule type approximation to the quasi-continuum method, *Multiscale Modeling & Simulation*, *8*(2), 571–590.
- Hellmann, H. (1939), Einführung in die quantenchemie (deuticke, leipzig, 1937); rpfeynman, *Phys. Rev*, *56*, 340.
- Hermansson, B., and D. Yevick (1986), Finite-element approach to band-structure analysis, *Physical Review B*, *33*, 7241–7242.
- Hirth, J. (1993), Crack nucleation in glide plane decohesion and shear band separation, *Scripta metallurgica et materialia*, *28*(6), 703–707.
- Hirth, J. P., and J. Lothe (1968), *Theory of Dislocations*, McGraw-Hill, New York.

- Hohenberg, P., and W. Kohn (1964), Inhomogeneous electron gas, *Physical review*, *136*(3B), B864.
- Huang, C., and E. A. Carter (2008), Transferable local pseudopotentials for magnesium, aluminum and silicon, *Physical Chemistry Chemical Physics*, *10*(47), 7109–7120.
- Huang, C., and E. A. Carter (2010), Nonlocal orbital-free kinetic energy density functional for semiconductors, *Physical Review B*, *81*(4), 045,206.
- Huang, C., and E. A. Carter (2012), Toward an orbital-free density functional theory of transition metals based on an electron density decomposition, *Physical Review B*, *85*(4), 045,126.
- Hung, L., C. Huang, I. Shin, G. S. Ho, V. L. Lignères, and E. A. Carter (2010), Introducing profess 2.0: A parallelized, fully linear scaling program for orbital-free density functional theory calculations, *Computer Physics Communications*, *181*(12), 2208–2209.
- Ismail-Beigi, S., and T. A. Arias (2000), *Ab Initio* study of screw dislocations in mo and ta: A new picture of plasticity in bcc transition metals, *Phys. Rev. Lett.*, *84*, 1499–1502.
- Jain, A., G. Hautier, C. J. Moore, S. P. Ong, C. C. Fischer, T. Mueller, K. A. Persson, and G. Ceder (2011), A high-throughput infrastructure for density functional theory calculations, *Computational Materials Science*, *50*(8), 2295–2310, doi: 10.1016/j.commatsci.2011.02.023.
- Johnson, R. (1988), Analytic nearest-neighbor model for fcc metals, *Physical Review B*, *37*(8), 3924.
- Kelchner, C. L., S. J. Plimpton, and J. C. Hamilton (1998), Dislocation nucleation and defect structure during surface indentation, *Phys. Rev. B*, *58*, 11,085–11,088.
- Knap, J., and M. Ortiz (2001), An analysis of the quasicontinuum method, *Journal of the Mechanics and Physics of Solids*, *49*(9), 1899–1923.
- Knap, J., and M. Ortiz (2003), Effect of indenter-radius size on au (001) nanoindentation, *Physical Review Letters*, *90*(22), 226,102.
- Kohn, W., and L. J. Sham (1965), Self-consistent equations including exchange and correlation effects, *Physical Review*, *140*(4A), A1133.
- Kresse, G., and J. Furthmüller (1996), Efficient iterative schemes for ab initio total-energy calculations using a plane-wave basis set, *Physical Review B*, *54*(16), 11,169.
- Kuan, H., and J. Hirth (1976), Dislocation pileups near the interface of a bimaterial couple, *Materials Science and Engineering*, *22*, 113–131.

- Langwallner, B., C. Ortner, and E. Süli (2010), Existence and convergence results for the galerkin approximation of an electronic density functional, *Mathematical Models and Methods in Applied Sciences*, 20(12), 2237–2265.
- Lehtovaara, L., V. Havu, and M. Puska (2009), All-electron density functional theory and time-dependent density functional theory with high-order finite elements, *The Journal of chemical physics*, 131(5), 054,103.
- Lennard-Jones, J. (1925), On the forces between atoms and ions, *Proceedings of the Royal Society of London. Series A*, 109(752), 584–597.
- Levine, Z. H., and J. W. Wilkins (1989), An energy-minimizing mesh for the schrödinger equation, *Journal of Computational Physics*, 83(2), 361–372.
- Li, J., K. J. Van Vliet, T. Zhu, S. Yip, and S. Suresh (2002a), Atomistic mechanisms governing elastic limit and incipient plasticity in crystals, *Nature*, 418(6895), 307–310.
- Li, J., K. J. V. Vliet, T. Zhu, S. Yip, and S. Suresh (2002b), Atomistic mechanisms governing elastic limit and incipient plasticity in crystals, *Nature*, 418, 307–310.
- Li, J., C.-Z. Wang, J.-P. Chang, W. Cai, V. V. Bulatov, K.-M. Ho, and S. Yip (2004), Core energy and peierls stress of a screw dislocation in bcc molybdenum: A periodic-cell tight-binding study, *Phys. Rev. B*, 70, 104,113.
- Luskin, M., and C. Ortner (2009), An analysis of node-based cluster summation rules in the quasicontinuum method, *SIAM Journal on Numerical Analysis*, 47(4), 3070–3086.
- Marian, J., W. Cai, and V. V. Bulatov (2004a), Dynamic transitions from smooth to rough to twinning in dislocation motion, *Nature Materials*, 3, 158–163.
- Marian, J., J. Knap, and M. Ortiz (2004b), Nanovoid cavitation by dislocation emission in aluminum, *Phys. Rev. Lett.*, 93, 165,503.
- Miller, R., M. Ortiz, R. Phillips, V. Shenoy, and E. Tadmor (1998a), Quasicontinuum models of fracture and plasticity, *Engineering Fracture Mechanics*, 61(3), 427–444.
- Miller, R., E. Tadmor, R. Phillips, and M. Ortiz (1998b), Quasicontinuum simulation of fracture at the atomic scale, *Modelling and Simulation in Materials Science and Engineering*, 6(5), 607.
- Miller, R. E., and E. Tadmor (2009), A unified framework and performance benchmark of fourteen multiscale atomistic/continuum coupling methods, *Modelling and Simulation in Materials Science and Engineering*, 17(5), 053,001.
- Miller, R. E., and E. B. Tadmor (2002), The quasicontinuum method: Overview, applications and current directions, *Journal of Computer-Aided Materials Design*, 9(3), 203–239.

- Morse, P. M. (1929), Diatomic molecules according to the wave mechanics. ii. vibrational levels, *Physical Review*, *34*(1), 57.
- Motamarri, P., M. Iyer, J. Knap, and V. Gavini (2012), Higher-order adaptive finite-element methods for orbital-free density functional theory, *Journal of Computational Physics*, *231*(20), 6596–6621.
- Nix, W. D., and H. Gao (1998), Indentation size effects in crystalline materials: A law for strain gradient plasticity, *Journal of the Mechanics and Physics of Solids*, *46*, 411 – 425.
- Ong, S. P., et al. (2011), The Materials Project.
- Ortiz, M., and R. Phillips (1998), Nanomechanics of defects in solids, *Advances in applied mechanics*, *36*, 1–79.
- Parr, R. G., and W. Yang (1989), *Density-functional theory of atoms and molecules*, vol. 16, Oxford university press.
- Pask, J., and P. Sterne (2005), Finite element methods in ab initio electronic structure calculations, *Modelling and Simulation in Materials Science and Engineering*, *13*(3), R71.
- Patera, A. (1984), A spectral element method for fluid dynamics: laminar flow in a channel expansion, *Journal of Computational Physics*, *54*(3), 468–488.
- Peach, M., and J. S. Koehler (1950), The forces exerted on dislocations and the stress fields produced by them, *Phys. Rev.*, *80*, 436–439.
- Perdew, J. P., and A. Zunger (1981a), *Phys. Rev. B*, *23*, 5048.
- Perdew, J. P., and A. Zunger (1981b), Self-interaction correction to density-functional approximations for many-electron systems, *Physical Review B*, *23*(10), 5048.
- Phillips, R., D. Rodney, V. Shenoy, E. Tadmor, and M. Ortiz (1999), Hierarchical models of plasticity: dislocation nucleation and interaction, *Modelling and Simulation in Materials Science and Engineering*, *7*(5), 769.
- Pizzagalli, L., J.-L. Demenet, and J. Rabier (2009), Theoretical study of pressure effect on the dislocation core properties in semiconductors, *Phys. Rev. B*, *79*, 045,203.
- Radhakrishnan, B., and V. Gavini (2010), Effect of cell size on the energetics of vacancies in aluminum studied via orbital-free density functional theory, *Physical Review B*, *82*(9), 094,117.
- Radovitzky, R., and M. Ortiz (1999), Error estimation and adaptive meshing in strongly nonlinear dynamic problems, *Computer Methods in Applied Mechanics and Engineering*, *172*(1), 203–240.
- Reed-Hill, R. E., and R. Abbaschian (1973), Physical metallurgy principles.

- Rice, J. R. (1992), Dislocation nucleation from a crack tip: An analysis based on the peierls concept, *Journal of the Mechanics and Physics of Solids*, *40*, 239 – 271.
- Segall, M., P. J. Lindan, M. Probert, C. Pickard, P. Hasnip, S. Clark, and M. Payne (2002), First-principles simulation: ideas, illustrations and the castep code, *Journal of Physics: Condensed Matter*, *14*(11), 2717.
- Shenoy, V., R. Miller, E. Tadmor, D. Rodney, R. Phillips, and M. Ortiz (1999), An adaptive finite element approach to atomic-scale mechanics the quasicontinuum method, *Journal of the Mechanics and Physics of Solids*, *47*(3), 611–642.
- Shenoy, V. B., R. Phillips, and E. B. Tadmor (2000), Nucleation of dislocations beneath a plane strain indenter, *Journal of the Mechanics and Physics of Solids*, *48*(4), 649–673.
- Shimokawa, T., J. J. Mortensen, J. Schiøtz, and K. W. Jacobsen (2004), Matching conditions in the quasicontinuum method: Removal of the error introduced at the interface between the coarse-grained and fully atomistic region, *Physical Review B*, *69*(21), 214,104.
- Shin, I., and E. A. Carter (2013), Possible origin of the discrepancy in peierls stresses of fcc metals: First-principles simulations of dislocation mobility in aluminum, *Phys. Rev. B*, *88*, 064,106.
- Shin, I., A. Ramasubramaniam, C. Huang, L. Hung, and E. A. Carter (2009a), Orbital-free density functional theory simulations of dislocations in aluminum, *Philosophical Magazine*, *89*, 3195–3213.
- Shin, I., A. Ramasubramaniam, C. Huang, L. Hung, and E. A. Carter (2009b), Orbital-free density functional theory simulations of dislocations in aluminum, *Philosophical Magazine*, *89*(34-36), 3195–3213.
- Smargiassi, E., and P. A. Madden (1994), Orbital-free kinetic-energy functionals for first-principles molecular dynamics, *Physical Review B*, *49*(8), 5220.
- Strang, W. G., and G. J. Fix (1973), *Analysis of the finite element method*, Prentice-Hall.
- Sutton, A., and J. Chen (1990), Long-range finnis–sinclair potentials, *Philosophical Magazine Letters*, *61*(3), 139–146.
- Tadmor, E., R. Phillips, and M. Ortiz (1996a), Mixed atomistic and continuum models of deformation in solids, *Langmuir*, *12*(19), 4529–4534.
- Tadmor, E., R. Miller, R. Phillips, and M. Ortiz (1999), Nanoindentation and incipient plasticity, *Journal of Materials Research*, *14*(06), 2233–2250.
- Tadmor, E. B., M. Ortiz, and R. Phillips (1996b), Quasicontinuum analysis of defects in solids, *Philosophical Magazine A*, *73*(6), 1529–1563.



- Takeuchi, S. (1999), Dislocation core effects on plasticity, *Radiation effects and defects in solids*, 148(1-4), 333–344.
- Trinkle, D. R., and C. Woodward (2005), The chemistry of deformation: How solutes soften pure metals, *Science*, 310(5754), 1665–1667.
- Vitek, V., R. C. Perrin, and D. K. Bowen (1970), The core structure of  $1/2$  (111) screw dislocations in bcc crystals, *Philosophical Magazine*, 21(173), 1049–1073.
- Wang, L.-W., and M. P. Teter (1992), Kinetic-energy functional of the electron density, *Physical Review B*, 45(23), 13,196.
- Wang, Y. A., N. Govind, and E. A. Carter (1999), Orbital-free kinetic-energy density functionals with a density-dependent kernel, *Physical Review B*, 60(24), 16,350.
- Wang, Y. A., N. Govind, and E. A. Carter (2001), Erratum: Orbital-free kinetic-energy functionals for the nearly free electron gas [phys. rev. b 58, 13 465 (1998)], *Physical Review B*, 64(12), 129,901.
- Weinan, E., J. Lu, and J. Z. Yang (2006), Uniform accuracy of the quasicontinuum method, *Physical Review B*, 74(21), 214,115.
- Weinberger, C. R., and W. Cai (2008), Surface-controlled dislocation multiplication in metal micropillars, *Proceedings of the National Academy of Sciences*, 105, 14,304–14,307.
- Woodward, C., D. R. Trinkle, L. G. Hector, and D. L. Olmsted (2008), Prediction of dislocation cores in aluminum from density functional theory, *Phys. Rev. Lett.*, 100, 045,507.
- Xia, J., and E. A. Carter (2012), Density-decomposed orbital-free density functional theory for covalently bonded molecules and materials, *Physical Review B*, 86(23), 235,109.
- Xia, J., C. Huang, I. Shin, and E. A. Carter (2012), Can orbital-free density functional theory simulate molecules?, *The Journal of Chemical Physics*, 136, 084,102.
- Yang, L., P. Söderlind, and J. A. Moriarty (2001), Accurate atomistic simulation of  $(a/2)_i$  111 $_i$  screw dislocations and other defects in bcc tantalum, *Philosophical Magazine A*, 81(5), 1355–1385.
- Yasi, J. A., L. G. H. Jr., and D. R. Trinkle (2010), First-principles data for solid-solution strengthening of magnesium: From geometry and chemistry to properties, *Acta Materialia*, 58, 5704 – 5713.